

Imparting Dynamics and Stability to Peptide-Directed Gold Nanoparticle Assemblies

by

Yicheng Zhou

Bachelor of Science, University of Science and Technology of China, 2013

Submitted to the Graduate Faculty of the
Dietrich School of Arts and Sciences in partial fulfillment
of the requirements for the degree of
Doctor of Philosophy

University of Pittsburgh

2021

UNIVERSITY OF PITTSBURGH

DIETRICH SCHOOL OF ARTS AND SCIENCES

This dissertation was presented

by

Yicheng Zhou

It was defended on

December 9, 2020

and approved by

Jill E. Millstone, Ph.D., Department of Chemistry

Alexander Star, Ph.D., Department of Chemistry

Sachin Velankar, Ph.D., Department of Chemical and Petroleum Engineering

Thesis Advisor/Dissertation Director: Nathaniel L. Rosi, Ph.D., Department of Chemistry and
Department of Chemical and Petroleum Engineering

Copyright © by Yicheng Zhou

2021

Imparting Dynamics and Stability to Peptide-Directed Gold Nanoparticle Assemblies

Yicheng Zhou, PhD

University of Pittsburgh, 2021

Gold nanoparticles (Au NPs) attract significant research attention due to their unique chemical, physical and biological properties, which make them promising candidates for various applications in electronics, catalysis, sensing, and therapeutics. When gold nanoparticles are organized into superstructures, new collective properties emerge, leading to a large expansion to their existing properties and applications. Of particular interest are peptide-based Au NP superstructures, in which peptides and peptide conjugates serve both as structure directing agents and Au NP capping agents.

While many previous research advances focused on assembling Au NPs into a certain superstructure using peptide or peptide conjugate molecules, an emerging area of research focuses on introducing dynamics to these peptide-based Au NP superstructures and tailoring their properties. Stimuli-based tunable handles can expand the horizon of applications of Au NP superstructures. Some intuitive but interesting questions can be asked: What stimuli can we use? How does the material behave when the stimuli are applied? How do we systematically tune the responsive behavior?

Many potential nanomaterial applications require that they be stable and durable. It is thus equally important to study and analyze peptide-based Au NP superstructures under various conditions. What destabilizes peptide-based Au NP superstructures? What factors influence the stability of the NP assembly? How can the stability of the assembly be enhanced?

This dissertation describes several research projects aimed at answering these compelling questions. First, a review of Au NP superstructures, in particular those fabricated using peptide-based precursors, is provided, which is followed by previous examples of stimuli-responsive materials and stability studies of NP assemblies. Second, I introduce a photo-responsive moiety to the peptide conjugate, which enables reversible changes to the morphology of both the peptide assembly and peptide-directed Au NP superstructures. By systematically tuning structural parameters of the peptide conjugate, an optimized morphology transition is realized upon light irradiation. Additionally, a new strategy for controlling photo-induced superstructure transformations based on host-guest chemistry is presented. Finally, I investigate the factors impacting the stability of Au NP single helices and determine strategies for enhancing their stability under different environmental conditions.

Table of Contents

Title Page	i
Committee Page	ii
Abstract.....	iv
Table of Contents	vi
List of Tables	x
List of Figures.....	xi
Preface.....	xxiii
1.0 Introduction to Peptide-Directed Gold Nanoparticle Assembly	1
1.1 Plasmonic Nanoparticles.....	3
1.2 Peptide-Based Au NP Superstructures.....	6
1.2.1 Peptide Assembly	6
1.2.2 Recognition Abilities of Peptides	7
1.2.3 Peptide Scaffolds for Nanoparticle Superstructures	10
1.2.3.1 Step-wise Assembly of Nanoparticles.....	11
1.2.3.2 One-Pot Synthesis of NP Superstructures	15
1.3 Reversible Assemblies of NPs	23
1.3.1 Light	24
1.3.2 Other Stimuli.....	29
1.3.2.1 Temperature.....	29
1.3.2.2 Biomolecules	29
1.3.2.3 pH	30

1.4 Objectives of the Dissertation.....	30
2.0 Design and Preparation of Photo-Responsive Peptide Conjugates for the Construction of Gold Nanoparticle Superstructures Having Photo-Regulated Morphological Transitions.....	32
2.1 Introduction	33
2.2 Results and Discussion	35
2.3 Conclusion	50
2.4 Supplementary Information	51
2.4.1 General Information	51
2.4.2 Syntheses of Azo-(CH ₂) _m -A _n -PEP _{Au} (m = 1-3, n = 0-2)	53
2.4.2.1 Synthesis of Azobenzene Carboxylic Acids	53
2.4.2.1.1 2-(4-(Phenyldiazenyl)phenyl)acetic Acid (MW = 240.15 g/mol)	53
2.4.2.1.2 3-(4-(Phenyldiazenyl)phenyl)propanoic Acid (MW = 254.29 g/mol)	54
2.4.2.1.3 4-(4-(Phenyldiazenyl)phenyl)butanoic Acid (MW = 268.32 g/mol)	55
2.4.2.2 Syntheses of Peptide Conjugates Azo-(CH ₂) _m -A _n -PEP _{Au} (m = 1-3, n = 0-2)	57
2.4.2.2.1 General Information	57
2.4.2.2.2 Peptide Synthesis and Purification	57
2.4.3 Supporting Figures and Tables.....	59

3.0 Photo-induced Assembly of One-Dimensional Au NP Superstructures Based on Azobenzene-Cyclodextrin Host-Guest Interactions.....	68
3.1 Introduction	68
3.2 Results and Discussions.....	70
3.2.1 Stability of Azo/CD-(CH₃)₃-PEP_{Au}	70
3.2.2 UV-Induced Peptide Conjugate Assembly	75
3.2.3 NP Assembly	78
3.3 Conclusion	85
3.4 Supplementary Information	85
3.4.1 General Methods	85
3.4.2 Synthetic Scheme for Peptide Conjugate Azo/CD-(CH₃)₃-PEP_{Au}	86
3.4.3 Synthesis of Azo-(CH₃)₃-COOH	87
3.4.4 Solid-Phase Peptide Synthesis of Azo/CD-(CH₃)₃-AA-PEP_{Au}.....	88
3.4.5 Molecular Structure of Azo-(CH₃)₃-A-PEP_{Au}.....	90
3.4.6 Molecular Structure of β-Cyclodextrin (β-CD).....	90
3.4.7 Assembly of Peptide Conjugate Azo/CD-(CH₃)₃-A-PEP_{Au} in HEPES Buffer and UV Irradiation	91
3.4.8 Synthesis of NPs Directed by Azo/CD-(CH₃)₃-A-PEP_{Au} and UV Irradiation	91
3.4.9 Transmission Electron Microscopy (TEM)	92
3.4.10 Fluorescence Studies	92
3.4.10.1 Molecular Structure of Thioflavin T (ThT)	92
3.4.10.2 ThT Fluorescence Studies for Peptide Assemblies	92

3.4.11 Supporting Figures.....	93
4.0 Investigating the Stability of Peptide-based Gold Nanoparticle Single Helices	95
4.1 Introduction	95
4.2 Results and Discussion	97
4.2.1 Elevated Temperature	99
4.2.2 Treatment with Proteinase K (ProK).....	104
4.2.3 Treatment with Urea	110
4.3 Conclusion.....	114
4.4 Supplementary Information	115
4.4.1 General Methods	115
4.4.2 Solid-Phase Peptide Synthesis of PEP _{Au} and N ₃ -PEP _{Au}	116
4.4.3 Preparation of N ₃ -PEP _{Au} ^{M-ox} and C ₁₈ -(PEP _{Au} ^{M-ox}) ₂	117
4.4.4 Synthesis of Small Au NP Single Helices	118
4.4.5 Synthesis of Medium and Large Au NP Single Helices	119
4.4.6 Transmission Electron Microscopy (TEM)	119
4.4.7 Circular Dichroism (CD) Spectroscopy	120
4.4.8 Fluorescence Studies	120
4.4.8.1 Molecular Structure of Thioflavin T (ThT).....	120
4.4.8.2 ThT Fluorescence Studies for Peptide Assemblies	120
Bibliography	122

List of Tables

Table 1.1. Examples of peptide sequences that are known to bind to plasmonic nanoparticles.	8
Table 2.1. Molar masses of conjugates Azo-(CH₂)_m-A_n-PEP_{Au}.....	59
Table 2.2. Temperature change of AuNP assemblies in HEPES buffer upon UV irradiation for 30 min and 1 hr.	63
Table 4.1. Metrics of Au NP single helices comprising of three different NP sizes.	98

List of Figures

Figure 1.1. Two strategies of constructing nanostructured materials: (a) “top-down” approach and (b) “bottom-up” approach.....	4
Figure 1.2. (a) Schematic representation of localized surface plasmon resonance (LSPR) of nanoparticle. (b) Example of Au NPs of different sizes exhibit different LSPR effect. Reproduced with permission.⁵⁷ Copyright 2007, Nature Publishing Group.....	5
Figure 1.3. Phage display and cell-surface display. Reproduced with permission from ref.⁸⁹ Copyright 2003, Nature Publishing Group.	10
Figure 1.4. Au nanowire by histidine-rich peptide nanotubules. Reproduced with permission from ref.⁸³ Copyright 2002, American Chemical Society.....	12
Figure 1.5. Double helical Au NP assembly based on peptides. TEM images of (a) T1 peptide fibrils, (b) Au colloidal NPs, and (c) double helical assembly of Au NPs directed by T1 peptide at pH = 6. Reproduced with permission from ref.¹⁰² Copyright 2003, Wiley-VCH.	13
Figure 1.6. Schematic (a) and TEM images (b) of a tripeptide, fiber-forming amphiphile assisted linear assembly of Au NPs. Reproduced with permission from ref.⁶³ Copyright 2005, Wiley-VCH.	14
Figure 1.7. Schematic representation of examples of modification of peptide conjugates and some resulting Au NP superstructures directed by peptide conjugates. (a) Many aspects of peptide conjugates can be systematically modified such as aliphatic tails, valencies, amino acid sequences and chirality, and oxidation state of single amino acid residue. (b) When a certain type of peptide conjugates is dissolved in HEPES buffer in the presence of an Au	

precursor, various Au NP superstructures are obtained depending on the kind of peptide conjugate chosen. 17

Figure 1.8. Double helical Au NP superstructures. TEM image (a), rendered tomographic reconstruction image (b), and schematic model (c) of Au NP double helical superstructures directed by peptide conjugate C₁₂-PEP_{Au}. Structural parameters such as constituent NP size (d-f) could be tuned for Au NP double helices. (a-c) Reproduced with permission from ref.¹⁶ Copyright 2008, American Chemical Society. (d-f) Reproduced with permission from ref.¹⁰⁵ Copyright 2010, American Chemical Society. 18

Figure 1.9. Chirality of the Au NP double helices could be dictated by using all L- or D-amino acids for C₁₂-PEP_{Au} conjugates. (a) Left- and (b) right-handed Au NP double helices are observed under TEM. Scale bar = 20 nm. (c) Mirrored chiroptical signals are observed for the two superstructures respectively. Reproduced with permission from ref.¹⁰⁶ Copyright 2013, American Chemical Society. 19

Figure 1.10. Spherical Au NP superstructures constructed using C₆-AA-PEP_{Au}. (a, b) TEM images of Au NP spherical superstructures. (c) 3-D surface rendering of the tomographic volume of Au NP spheres Reproduced with permission from ref.²⁰ Copyright 2010, American Chemical Society. (d) Cumulative release profile of DOX-loaded Au NP spheres. Reproduced with permission from ref.¹⁰⁹ Copyright 2015, Royal Society of Chemistry. 20

Figure 1.11. Single helical Au NP superstructures. (a) TEM image and (b) 3-D rendering of tomographic rendering of single helical Au NP superstructures directed by peptide conjugate C₁₈-(PEP_{Au}^{M-ox})₂. (c) AFM mapping and schematics representation of the underlying coiled ribbon assembly of peptide conjugate. (d) The resulting Au NP single helices showed enhanced chiroptical response with a g-factor of 0.02. Reproduced with

permission from ref.²⁷ Copyright 2016, American Chemical Society. (e) Schematic illustration of tuning structural features of single helix assembly by modifying the aliphatic tail of peptide conjugate $C_x-(PEP_{Au}^{M-ox})_2$ ($x = 16-22$). (f) TEM images of single helical Au NP assembly directed by conjugates $C_x-(PEP_{Au}^{M-ox})_2$ ($x = 16-22$). Reproduced with permission from ref.²⁸ Copyright 2017, American Chemical Society. (g) Adding auxiliary particle capping agents to the synthesis of Au NP single helices introduced anisotropy to constituent particles. Reproduced with permission from ref.¹¹⁰ Copyright 2018, Wiley-VCH..... 22

Figure 1.12. Photo-isomerization of azobenzene..... 25

Figure 1.13. Controlling NP assembly using light. (a) An early example of controlling aggregation of Au NPs by functionalizing the surface of Au NPs with a dithiolated azobenzene ligand. Reproduced with permission from ref.¹⁵⁵ Copyright 2005, American Chemical Society. (b) Assembling Au NPs into well-defined crytaline superstructures using light. Reproduced with permission from ref.¹³¹ Copyright 2007, The National Academy of Sciences of the USA. (c) Light-induced self-erasable film doped with photo-responsive Au NP. Reproduced with permission from ref.¹²⁹ Copyright 2009, Wiley-VCH. (d) Catalysis that can be turned “on” and “off” by using photo-responsive Au NPs. Reproduced with permission from ref.⁵³ Copyright 2010, American Chemical Society. (e) Tuning Au NP assembly and disassembly based on azobenzene- β -CD host-guest interactions. Reproduced with permission from ref.¹⁵⁶ Copyright 2016, American Chemical Society..... 27

Figure 2.1. Schematic representation of controlling peptide-based photoresponsive Au NP superstructure by systematically modifying peptide conjugates..... 33

Figure 2.2. (a) Schematic representation of the AzO-(CH₂)_m-A_n-PEP_{Au} (m = 1-3, n = 0-2). (b-j) TEM images of peptide assemblies as a function of number of methylene groups and number of alanine residues: (b) AzO-(CH₂)₁-A₀-PEP_{Au}, (c) AzO-(CH₂)₂-A₀-PEP_{Au}, (d) AzO-(CH₂)₃-A₀-PEP_{Au}, (e) AzO-(CH₂)₁-A₁-PEP_{Au}, (f) AzO-(CH₂)₂-A₁-PEP_{Au}, (g) AzO-(CH₂)₃-A₁-PEP_{Au}, (h) AzO-(CH₂)₁-A₂-PEP_{Au}, (i) AzO-(CH₂)₂-A₂-PEP_{Au} and (j) AzO-(CH₂)₃-A₂-PEP_{Au}. (k-p) FT-IR and CD spectra of AzO-(CH₂)_m-A_n-PEP_{Au}: (k) and (n), n = 0; (l) and (o), n = 1; (m) and (p), n = 2; green line, m = 1; red line, m = 2; blue line, m = 3. 37

Figure 2.3. TEM images of AzO-(CH₂)_m-A_n-PEP_{Au} (m = 1-3, n = 0-2) assemblies after UV irradiation for 30 min (a – i), and corresponding CD spectra (j – l). Black: m =1; red: m = 2; blue: m = 3. 40

Figure 2.4. TEM images of AzO-(CH₂)_m-A_n-PEP_{Au} (m = 1-3, n = 0-2) assemblies after visible light irradiation for 18 hrs (a – i), and corresponding CD spectra (j – l). Black: m =1; red: m = 2; blue: m = 3. 41

Figure 2.5. UV and visible irradiation of peptide assemblies and NP assemblies formed using AzO-(CH₂)₂-A₁-PEP_{Au}. Top row: peptide assembly before UV irradiation (a), after UV irradiation for 30 min (b) and after visible light irradiation for 18 hrs (c), and corresponding CD signal (d) (Green: before UV irradiation; red: after UV irradiation; blue: after visible light irradiation). Bottom row: NP assembly before UV irradiation (e), after UV irradiation for 30 min (f) and after visible light irradiation for 18 hrs (g), and corresponding UV-Vis spectra (h) (Green: before UV irradiation; red: after UV irradiation; blue: after visible light irradiation). 42

Figure 2.6. Dynamic light scattering results of AzO-(CH₂)₂-A₁-PEP_{Au}, assemblies before UV irradiation (black), after UV irradiation for 30 min (red) and after visible light irradiation (blue).....	43
Figure 2.7. TEM images of NP assemblies directed by AzO-(CH₂)_m-A_n-PEP_{Au} (m = 1-3, n = 0-2) before irradiation (a – i).....	45
Figure 2.8. TEM images of NP assemblies directed by AzO-(CH₂)_m-A_n-PEP_{Au} (m = 1-3, n = 0-2) after UV irradiation for 30 min (a – i).....	46
Figure 2.9. TEM images of NP assemblies directed by AzO-(CH₂)_m-A_n-PEP_{Au} (m = 1-3, n = 0-2) after visible light irradiation for 18 hrs (a – i).....	47
Figure 2.10. UV and visible light irradiation on AzO-(CH₂)₂-A₁-PEP_{Au} directed assemblies as a function of time. Top row: UV irradiation of AzO-(CH₂)₂-A₁-PEP_{Au} directed assemblies for (a) 0 min, (b) 5 min, (c) 10 min, (d) 15 min and (e) 30 min. Bottom row: visible light irradiation of AzO-(CH₂)₂-A₁-PEP_{Au} directed assemblies for (f) 2 h, (g) 4 h, (h) 6 h, (i) 8 h and (j) 12 h.....	50
Figure 2.11. Schematic for synthesis of azobenzene carboxylic acids.....	53
Figure 2.12. ¹H-NMR spectrum of 2-(4-aminophenyl)acetic acid.....	54
Figure 2.13. ¹H-NMR spectrum of 3-(4-aminophenyl)propanoic acid.....	55
Figure 2.14. ¹H-NMR spectrum of 4-(4-Aminophenyl)butanoic acid.....	56
Figure 2.15. MALDI-TOF spectra of AzO-(CH₂)_m-A_n-PEP_{Au} (m = 1-3, n = 0-2). (a)-(c) m = 1-3, n = 0; (d)-(f) m = 1-3, n = 1, (g)-(i) m = 1-3, n = 2.....	59
Figure 2.16. Metrics of peptide assemblies formed using AzO-(CH₂)_m-A_n-PEP_{Au}. For spherical peptide assemblies (a) AzO-(CH₂)₁-A₀-PEP_{Au}, (b) AzO-(CH₂)₂-A₀-PEP_{Au}, (c) AzO-(CH₂)₃-A₀-PEP_{Au}, and (d) AzO-(CH₂)₂-A₁-PEP_{Au}, diameters are measured based on at least	

100 counts. For fiber assemblies (e) AzO-(CH₂)₂-A₁-PEP_{Au}, (f) AzO-(CH₂)₃-A₁-PEP_{Au}, (g) AzO-(CH₂)₁-A₂-PEP_{Au}, (h) AzO-(CH₂)₂-A₂-PEP_{Au}, and (i) AzO-(CH₂)₃-A₂-PEP_{Au}, widths of fibers are measured based on at least 100 counts. 60

Figure 2.17. UV-Vis spectra of NP assemblies formed using AzO-(CH₂)_m-A_n-PEP_{Au} (m = 1-3, n = 0) before irradiation (black), after UV irradiation (red) and after visible light irradiation (blue)..... 61

Figure 2.18. TEM images of peptide (a-c) and AuNP assembly (d-f) upon UV and visible light irradiation directed by conjugate BP-AA-PEP_{Au} (BP = biphenyl). (a) and (d): before UV irradiation; (b) and (e) after UV irradiation for 30 min; (c) and (f) after visible light irradiation for 18 hrs. 62

Figure 2.19. NP size measurement in assemblies formed using AzO-(CH₂)₂-A₁-PEP_{Au} before UV irradiation (a), after UV irradiation for 30 min (b) and after visible light irradiation for 18 hrs (c). 62

Figure 2.20. TEM images of a sample without addition of any peptide conjugates irradiated by UV light for 30 min..... 63

Figure 2.21. Additional TEM images of NP assemblies formed using AzO-(CH₂)₂-A₁-PEP_{Au} after UV irradiation for 30 min. 64

Figure 2.22. Additional TEM images for NP assemblies formed using AzO-(CH₂)₂-A₁-PEP_{Au} before UV irradiation. 64

Figure 2.23. Additional TEM images for NP assemblies formed using AzO-(CH₂)₂-A₁-PEP_{Au} after UV irradiation for 5 min. 65

Figure 2.24. Additional TEM images for NP assemblies formed using AzO-(CH₂)₂-A₁-PEP_{Au} after UV irradiation for 10 min. 65

Figure 2.25. Additional TEM images for NP assemblies formed using Azo-(CH ₂) ₂ -A ₁ -PEP _{Au} after UV irradiation for 15 min.	65
Figure 2.26. Additional TEM images for NP assemblies formed using Azo-(CH ₂) ₂ -A ₁ -PEP _{Au} after UV irradiation for 30 min.	66
Figure 2.27. Additional TEM images for NP assemblies formed using Azo-(CH ₂) ₂ -A ₁ -PEP _{Au} after visible light irradiation for 2 h.	66
Figure 2.28. Additional TEM images for NP assemblies formed using Azo-(CH ₂) ₂ -A ₁ -PEP _{Au} after visible light irradiation for 4 h.	66
Figure 2.29. Additional TEM images for NP assemblies formed using Azo-(CH ₂) ₂ -A ₁ -PEP _{Au} after visible light irradiation for 6 h.	67
Figure 2.30. Additional TEM images for NP assemblies formed using Azo-(CH ₂) ₂ -A ₁ -PEP _{Au} after visible light irradiation for 8 h.	67
Figure 2.31. Additional TEM images for NP assemblies formed using Azo-(CH ₂) ₂ -A ₁ -PEP _{Au} after visible light irradiation for 12 h.	67
Figure 3.1. Schematic representation of light-triggered peptide fiber assembly and one-dimensional Au NP superstructures by UV-induced β -CD removal from azobenzene incorporated peptide conjugate.	70
Figure 3.2. RP-HPLC elution of Azo/CD-(CH ₃) ₃ -A-PEP _{Au}	71
Figure 3.3. MALDI-TOF spectra of (a) Azo/CD-(CH ₃) ₃ -A-PEP _{Au} (calc. 2676, found [M+Na] ⁺ = 2699) and (b) Azo-(CH ₃) ₃ -A-PEP _{Au} (calc. 1564, found [M] ⁺ = 1564).	71
Figure 3.4. Assembly studies of Azo/CD-(CH ₃) ₃ -A-PEP _{Au} in the absence (a-d) and presence (e-h) of additional β -CD in HEPES buffer. (a, b) Negatively stained TEM images of Azo/CD-(CH ₃) ₃ -A-PEP _{Au} assemblies in 0.1 M HEPES buffer at 5 min (a) and 30 min (b).	

(c) DLS data of Azo/CD-(CH₃)₃-A-PEP_{Au} assemblies in 0.1 M HEPES buffer over a period of 20 hrs. (d) ThT emissions of Azo/CD-(CH₃)₃-A-PEP_{Au} assemblies in 0.1 M HEPES buffer recorded up to 2 d. (e, f) Negatively stained TEM images of Azo/CD-(CH₃)₃-A-PEP_{Au} assemblies in 0.1 M HEPES/ β -CD mixed buffer at 30 min (e) and 1 d (f). (g) DLS data of Azo/CD-(CH₃)₃-A-PEP_{Au} assemblies in 0.1 M HEPES/ β -CD mixed buffer over a period of 1 d. (h) ThT emissions of Azo/CD-(CH₃)₃-A-PEP_{Au} assemblies in 0.1 M HEPES/ β -CD mixed buffer recorded up to 2 d. Scale bar = 200 nm..... 73

Figure 3.5. Negatively stained TEM images of assemblies of Azo/CD-(CH₃)₃-A-PEP_{Au} in 0.1 M HEPES buffer at 5 min..... 74

Figure 3.6. UV irradiation of assemblies of Azo/CD-(CH₃)₃-A-PEP_{Au} in β -CD saturated 0.1 M HEPES buffer. (a, b) Negatively stained TEM images of assemblies of Azo/CD-(CH₃)₃-A-PEP_{Au} in 0.1 M HEPES buffer saturated by β -CD before (a) and after (b) UV irradiation for 30 min. (c) DLS data recorded before and after UV irradiation of the sample for 30 min. (d) Effect of the time lengths of UV irradiation monitored via ThT emission spectra. 77

Figure 3.7. Negatively stained TEM images of assemblies of Azo/CD-(CH₃)₃-A-PEP_{Au} in 0.1 M HEPES buffer (a) before irradiation, (b) after UV irradiation for 30 min, and (c) after visible light irradiation for 4 hrs..... 78

Figure 3.8. UV irradiation of Au NPs directed by Azo/CD-(CH₃)₃-A-PEP_{Au}. (a, b) TEM images of Au NPs directed by Azo/CD-(CH₃)₃-A-PEP_{Au} before (a) and after (b) irradiation for 30 min. (c) UV-Vis spectra of the Au NPs before and after UV irradiation for 30 min. (d) ThT fluorescence emission spectra (ex. 450 nm) of Au NPs before and after UV irradiation for 30 min. 80

Figure 3.9. Additional TEM images of Au NPs directed by Azo/CD-(CH ₃) ₃ -A-PEP _{Au} in 0.1 M HEPES buffer saturated by β -CD before (a-d) and after (e, f) UV irradiation for 30 min.....	82
Figure 3.10. (a, b) TEM images and (c) ThT fluorescence of Au NPs directed by Azo/CD-(CH ₃) ₃ -A-PEP _{Au} after incubating in 0.1 M HEPES saturated with β -CD for 1 d.....	82
Figure 3.11. (a) TEM image of Au NPs synthesized using PEP _{Au} . (b, c) Negatively stained TEM images of PEP _{Au} capped Au NPs in the presence of equimolar Azo-(CH ₃) ₃ -A-PEP _{Au} (b) or Azo/CD-(CH ₃) ₃ -A-PEP _{Au} (c). (d) Negatively stained TEM image of Au NPs sample in (c) after UV irradiation for 30 min.	84
Figure 3.12. Synthetic scheme for peptide conjugate Azo/CD-(CH ₃) ₃ -PEP _{Au}	86
Figure 3.13. ¹ H-NMR spectrum of 4-(4-Aminophenyl)butanoic acid.	88
Figure 3.14. Molecular Structure of Azo-(CH ₃) ₃ -A-PEP _{Au}	90
Figure 3.15. Molecular structure of β -cyclodextrin (β -CD).....	90
Figure 3.16. Negatively stained TEM image of assembly of Azo-(CH ₃) ₃ -A-PEP _{Au} in 0.1 M HEPES buffer at 2 h.	93
Figure 3.17. Diameter distribution (based on 100 counts) of NPs directed by conjugate Azo/CD-(CH ₃) ₃ -A-PEP _{Au} (a) before and (b) after UV irradiation for 30 min. The average diameters before and after UV irradiation are 7.7 ± 0.9 nm and 8.3 ± 1.5 nm, respectively.	94
Figure 4.1. Schematic representation of increasing the stability of peptide-based Au NP single helices against heat, urea or ProK by increasing the constituent NP sizes.	97

Figure 4.2. Characterization of AuNP single helices of increasing NP sizes. TEM images and metrics measurements of small (a, d), medium (b, e), and large (c, f) Au NP single helices. Scale bar, 50 nm. Measurements are based on at least 100 counts. 98

Figure 4.3. Negatively stained TEM images of assemblies of conjugate $C_{18}-(PEP_{Au}^{M-ox})_2$ in 0.1 M HEPES buffer as temperature increases from 25 °C to 90 °C..... 99

Figure 4.4. (a) CD spectra of assemblies of conjugate $C_{18}-(PEP_{Au}^{M-ox})_2$ in 0.1 M HEPES buffer as temperature increases from 25 °C to 90 °C. (b) CD intensity at 208 nm (black), 220 nm (red), and 237 nm (blue) as temperature increases from from 25 °C to 90 °C. 101

Figure 4.5. (a) ThT emissions upon excitation at 450 nm as a function of temperature. (b) Emission intensity at 485 nm as a function of temperature..... 101

Figure 4.6. Effect of temperature on Au NP single helices. TEM images and CD intensity at 560 nm of small (top row), medium (middle row), and large (bottom) Au NP single helices at different temperatures. Scale bar = 100 nm. CD intensity data were collected using three parallel measurements..... 103

Figure 4.7. CD spectra of small (a), medium (b), and large (c) Au NP single helices when temperatures were increased from 25 °C to 90 °C. 103

Figure 4.8. ThT emission spectra (excited at 450 nm) recorded at different time points when incubated with $C_{18}-(PEP_{Au}^{M-ox})_2$ (20 nmol) in 0.1 M HEPES buffer at 37 °C in the presence of different concentrations of ProK: (a) 0.02 mg/mL, (b) 0.1 mg/mL, (c) 0.2 mg/mL, (d) 0.4 mg/mL, (e) 0.8 mg/mL. 105

Figure 4.9. Negatively stained TEM images of $C_{18}-(PEP_{Au}^{M-ox})_2$ (20 nmol) assemblies before (top row) and after (bottom row) ProK was added. ProK concentrations: (a, b) 0.02 mg/mL, (c, d) 0.1 mg/mL, (e, f) 0.2 mg/mL, (g, h) 0.4 mg/mL, (i, j) 0.8 mg/mL. For 0.02

mg/mL ProK, TEM images were taken after 18 hours incubation; for all other concentrations, TEM images were taken after 30 min incubation. Scale bar = 100 nm. 105

Figure 4.10. TEM images and ThT fluorescence spectra of small (left column), medium (middle column), and large (right column) Au NP single helices before (top row) and after (middle row) mixing with ProK. Scale bar = 100 nm. 107

Figure 4.11. TEM images of small (a, d), medium (b, e), and large (c, f) Au NP single helices before (top row) and after (bottom row) incubating with 0.02 mg/mL ProK. Scale bar = 100 nm. 108

Figure 4.12. Negatively stained TEM images of small (a, d), medium (b, e), and large (c, f) Au NP single helices before (top row) and after (bottom row) mixing with ProK. Scale bar = 100 nm. 109

Figure 4.13. Normalized emission at 485 nm of ThT in the presence of $C_{18}-(PEP_{Au}^{M-ox})_2$ and different concentrations of urea as a function of time. 111

Figure 4.14. Negatively stained TEM images of $C_{18}-(PEP_{Au}^{ox})_2$ assembly after incubating with urea of different concentrations. Urea concentrations: (a) 0.5 M, (b) 1 M, and (c) 2 M. 111

Figure 4.15. Effects of different concentrations of urea on Au NP single helices of increasing constituent NP sizes. TEM images of small (a, b, c), medium (e, f, g), and large (i, j, k) Au NP single helices after incubating with different urea concentrations (a, e, i: 0.5 M. b, f, j: 1 M. c, g, k: 2 M) for 1 d. Normalized ThT emissions for small (d), medium (h), and large (l) Au NP single helices at 480 nm recorded for up to 1 d (urea concentrations: black, 0.5 M; red, 1 M; blue, 2 M). See Fig. S12 for full ThT emission spectra. 113

Figure 4.16. ThT emission spectra excited at 450 nm of small, medium, and large Au NP single helices upon incubating with different concentrations of urea. NP sizes: (a, b, c) small, (d, e, f) medium, (g, h, i) large. Urea concentrations: (a, d, g) 0.5 M, (b, e, h) 1 M, (c, f, i) 2 M. 114

Figure 4.17 Synthetic scheme for peptide conjugate C₁₈-(PEP_{Au}^{M-ox})₂. 116

Figure 4.18. Molecular structure of C₁₈-(PEP_{Au}^{M-ox})₂. 118

Figure 4.19. Molecular structure of thioflavin T (ThT). 120

Preface

It has finally come to the end of my Ph.D. studies. It is indeed a challenging yet rewarding journey, and the final prize would be this Ph.D. dissertation. The results of this research undertaken at the Department of Chemistry of the University of Pittsburgh would not have been possible without the help of many people, and I am fortunate to have all of them along the way.

I would like to first thank my advisor, Prof. Nathaniel Rosi, for his mentorship. I benefited a lot from his guidance both academically and personally. I first grew my interest toward peptide and nanoparticle research when I was an exchange student to UCLA in the summer of 2012. At the start my graduate studies here at Pitt, it was very lucky for me to continue my interest in this field of research in Prof. Rosi's group. Of course, there were ups and downs in the lab, and even setbacks, but I appreciate Prof. Rosi's efforts for keeping me focused on what is important and critical during research. I am honored to have his mentorship and it is truly a rewarding one.

There are many people in the group with whom I shared fond friendship. Dr. Andrea Merg is the first member in the group who taught me the specifics of all experiment steps he knows. I benefited a lot from his benchtop expertise. He is a great mentor in lab and a great friend in life. Dr. Chen Zhang and Dr. Chong Liu are both great researchers in lab with whom I shared many late nights in lab. I appreciate their assistance with my experiments and they sometimes have just the answer to a question I have. I would also like to thank Dr. Alex Spore who is always keeping the spirit of the group high! I also enjoyed my collaboration with Dr. Soumitra Punekar who is a diligent researcher in lab and a close friend out of lab. Dr. Tian-yi Luo and Dr. Patrick Muldoon are excellent researchers and I learned a lot from them. It is also my honor to work together with the current group members, Dr. Prasenjit Das, Dr. Yi Han, Yiwen He, Dr. Yeon-Hye Kwon,

Matheus de Souza, Dr. Mona Mohamed and Zack Schulte; in particular, I would like to mention Sydney Brooks, who worked hard for making the review article in *Advanced Materials* possible. I also enjoyed my time in the group with many undergraduate and visiting researchers.

I would express my gratitude to my committee members, Prof. Jill Millstone, Prof. Alexander Star and Prof. Sachin Velankar. I also want to thank our collaborators at Department of Structural Biology of Pitt, Prof. Peijun Zhang, Dr. Dapeng Zhang, and Dr. Zhengyi Yang, as well as many staff members at Department of Chemistry and Department of Biology, especially Dr. Tom Harper at Department of Biology who is a helping and warm friend.

The biggest influence in my life has been my parents, and I cannot thank them enough for their unconditional love and support. I also want to thank my grandpa who was there for me all the time. It is also my privilege to have many friends along the way, but I would like to name Pengfei Cheng, in particular, for his companionship, assistance and care, and I cherish every moment we spend together.

It is truly honored and privileged to have all these people with me and I could not thank you enough for everything you have done.

1.0 Introduction to Peptide-Directed Gold Nanoparticle Assembly

PARTS OF THIS CHAPTER are under review as a book chapter entitled “Peptide-based methods for the assembly of plasmonic nanostructures.”

Nanostructures are a family of materials that have at least one dimension between 1 and 100 nm.¹ Compared to bulk materials, nanostructures are particularly exciting to researchers because they exhibit unique and exceptional chemical,² physical,³ and/or biological⁴⁻⁶ properties due to the fact that at least one dimension is confined to the nanometer regime. Control over the size, shape, and composition of nanostructures allows for control over the fundamental properties of the material.⁷ Furthermore, ensembles of nanostructures give rise to the emergence of new collective and complex properties when the nanostructures are organized in a hierarchical manner. Nanostructures, along with their assemblies, are promising building blocks for materials with advanced functional capabilities.⁸⁻¹¹

Peptides are a family of linear biomolecules composed of sequences of amino acids linked via amide bonds. As a result, many properties of peptides, such as self-assembly and surface recognition, are sequence-specific. Therefore, tuning the sequence of amino acid residues within a peptide could lead to precise control of the overall properties of the peptide, which, of course, includes control of self-assembly architecture and inorganic surface binding. Based on the unique properties of peptides, their ability to direct and regulate the assembly of nanoparticles, especially gold nanoparticles (Au NPs), is attracting much research interest.¹²⁻³⁴ By rationally designing the peptide, the morphology and properties of the resulting Au NP assemblies can be systematically modified, which exemplifies the capability of peptides as excellent assembly agents for constructing complex Au NP superstructures.

Introducing reversibility to nanoparticle assemblies is of great importance in material science as it serves a new route toward the development of stimuli-responsive materials. In particular, stimuli-responsive Au NPs, which have many unique properties such as drug delivery³⁵⁻³⁷ or bio-sensing,³⁸⁻³⁹ are probably one of the most studied nanomaterials. Precisely controlling the reversible morphological transitions of AuNP assemblies is very important, because many physical and chemical properties of these assemblies are governed by their morphology and/or metrics. Our aim is to adapt design methodology developed for constructing morphologically-tunable peptide-based assemblies to prepare and study structurally-responsive nanoparticle superstructures.

The structural stability of Au NP superstructures should be a controllable feature. Some downstream applications may require highly robust materials while others may require intermediate stability. It is important to examine the stability of peptide-based NP superstructures under a wide range of conditions, such as at elevated temperatures, under photo-irradiation, at acidic/neutral/basic pHs, within biofluids, and in the presence of other biomolecules. More broadly, understanding the factors impacting the NP and NP assembly stability is important for developing safe, durable, and effective materials for biosensing, therapeutics, and electronic devices.

Motivated by the discussion above, in this chapter I will first set the stage by introducing and reviewing plasmonic nanoparticles and their assemblies. Discussion will then be focused on peptide-based Au NP superstructures in particular. Next, I will present advances made in controlling NP assembly in the presence of external stimuli and in controlling the colloidal stability of NPs. Finally, a brief introduction to the three projects I have completed in my Ph.D. studies will be provided.

1.1 Plasmonic Nanoparticles

Inorganic nanostructures have attracted widespread attention over the last several decades. For example, research on metallic nanoparticles, semiconducting nanoparticles,⁴⁰ and metal oxide nanoparticles are abundant and expanding constantly due to their capabilities as bio-imaging tools,^{11,41-42} drug delivery vehicles,⁴³⁻⁴⁷ bio-sensors,^{5,26,42,48-49} and catalysts.^{2,50-53} The performance and properties of inorganic nanomaterials can be tuned and optimized through systematic tuning of their composition, size, and assembly architecture.

To construct a specific nanostructured material, two common strategies are used: the “top-down” approach or the “bottom-up” approach (Figure 1.1). The first approach usually starts from a bulk material and one or more dimensions of the material is gradually reduced to nanometer scale. This process resembles how a sculpture is carved from bulk marble. Control over the size and shape of the resulting product can be precise; however, hierarchy or complexity of the material, such as composition mixing or layer-by-layer arrangement, may present a challenge. On the contrary, the “bottom-up” approach often involves hierarchical manipulation of atomic, molecular, and nanoparticle building units. This approach is flexible, and the chemical or physical properties of the final nanostructure can be tailored through rational design and synthesis of the constituent building blocks.

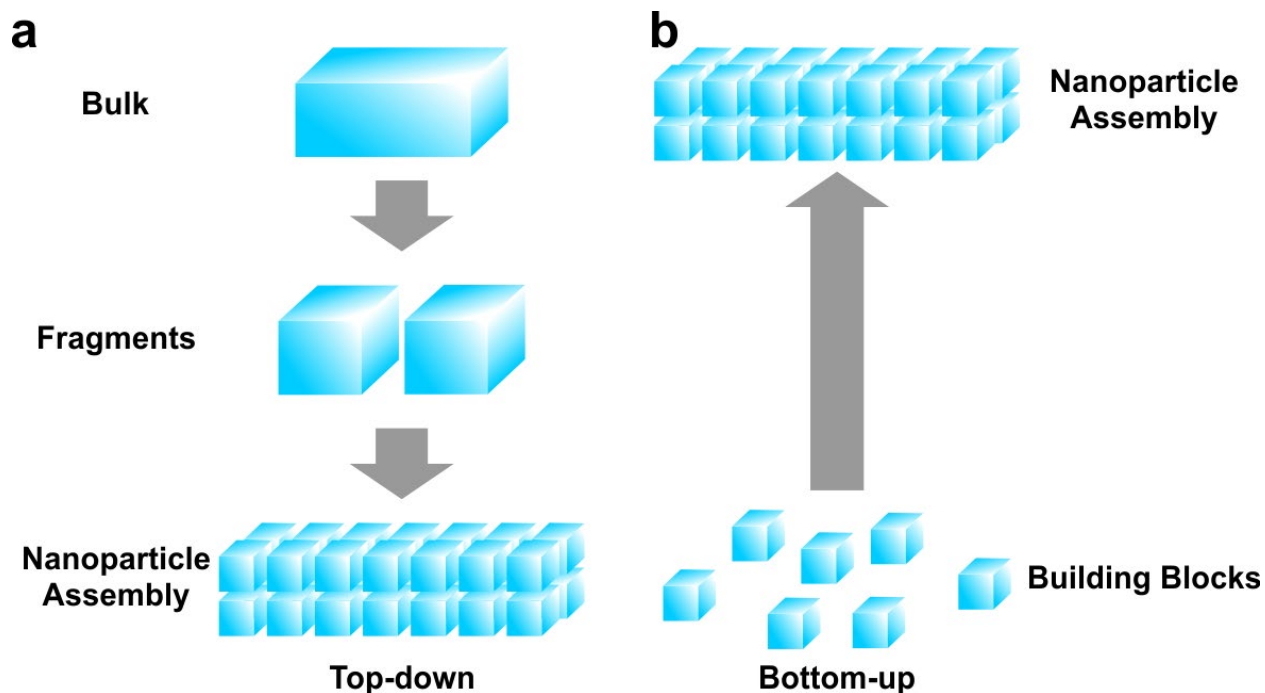


Figure 1.1. Two strategies of constructing nanostructured materials: (a) “top-down” approach and (b) “bottom-up” approach.

Plasmonic nanostructured materials, in particular, have attracted considerable attention because they exhibit unique size- and shape-dependent optical properties. The dimensions of the material lead to geometric confinement of electrons. When the oscillation of conduction electrons matches the frequency of incident light, a phenomenon called localized surface plasmon resonance (LSPR) occurs (Figure 1.2).^{49,54} Based on the composition, size, shape, dielectric environment, and/or assembly/aggregation state of the metallic NPs,⁵⁵⁻⁵⁷ the position of the LSPR varies from the visible to near infrared (NIR) regime in the spectrum, which allows for a wide variety of applications, especially in optical sensing.⁴²

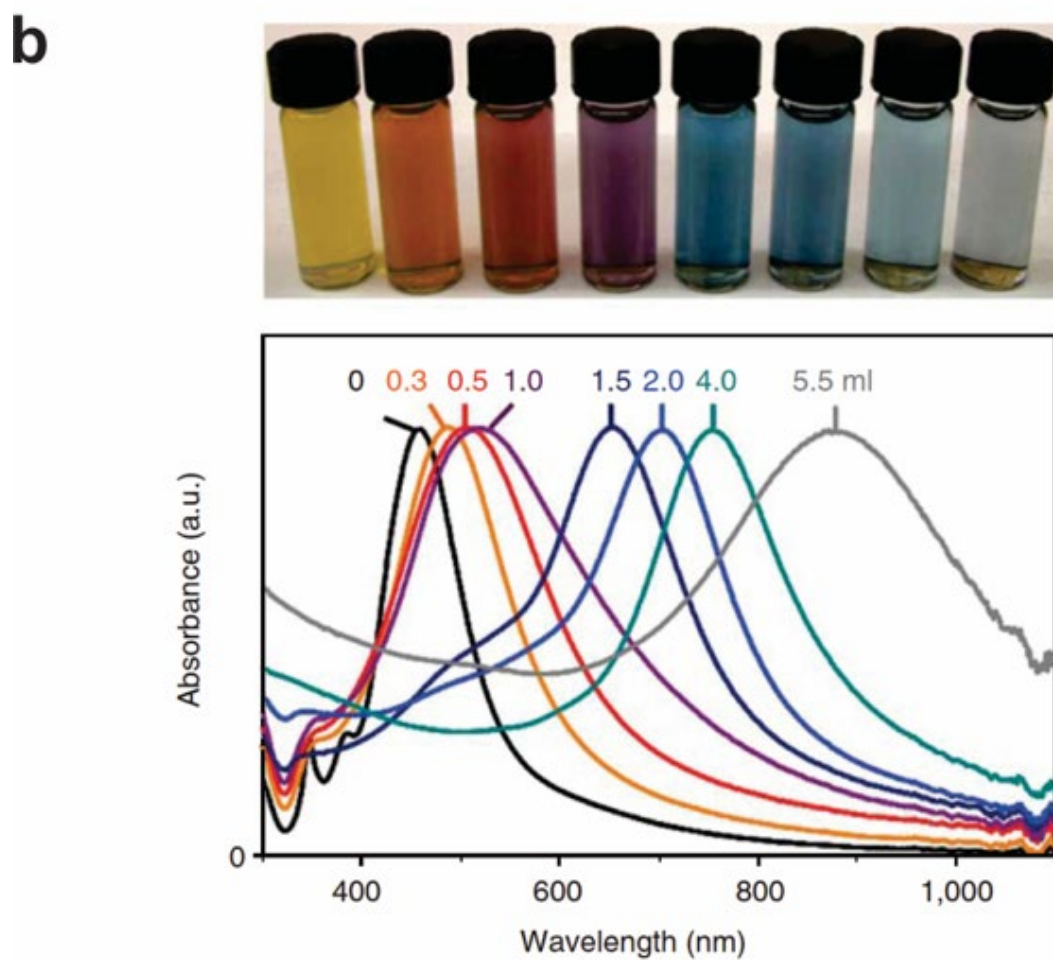
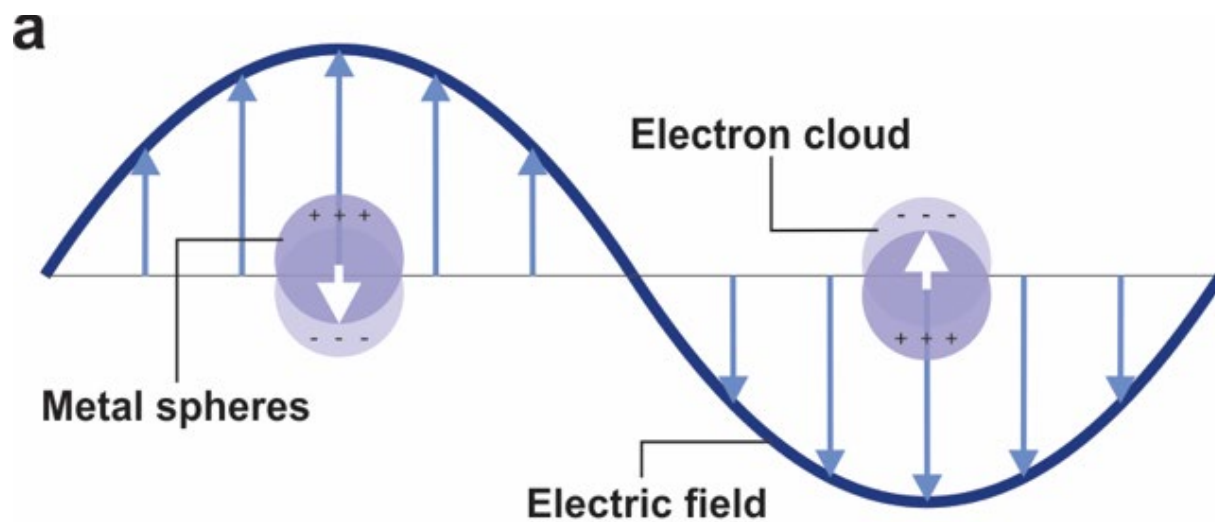


Figure 1.2. (a) Schematic representation of localized surface plasmon resonance (LSPR) of nanoparticle. (b) Example of Au NPs of different sizes exhibit different LSPR effect. Reproduced with permission.⁵⁷ Copyright 2007, Nature Publishing Group.

One way of uncovering new and unusual plasmonic optical properties of nanoparticles is to assemble them into structurally well-defined superstructures which will exhibit collective optical properties that depend on the arrangement of the constituent nanoparticles. There are many biomolecules such as nucleic acids, carbohydrates, proteins,⁵⁸ and peptides⁵⁹ that are themselves “nanoscale” and can be used to impact nanomaterial properties and influence their assembly. We focus exclusively on peptides as directing agents for nanoparticle synthesis and assembly. Peptides are excellent candidates for this task due to their unique sequence-specific self-assembly and inorganic surface recognition capabilities.

1.2 Peptide-Based Au NP Superstructures

1.2.1 Peptide Assembly

Peptides have multiple levels of structure, with the simplest being the primary structure – the sequence of amino acids in a polypeptide chain. The next level of structure is the secondary structure, which is due to interactions between atoms along the peptide backbone. Depending on the sequence, conformation, and stereo-configuration of the constituent amino acids, peptides may exhibit many different secondary structures, with α -helix and β -sheet being the most common. In terms of self-assembly of peptides, extensive effort has been invested in studying the β -sheet secondary structure due to its ability to direct and form a variety of structures, as well as its critical role in peptide fibrilization in Alzheimer’s disease.⁶⁰⁻⁶¹

Intra- or inter-peptide hydrogen bonding is the driving force for forming the secondary structure, which is essentially the interaction between different amino acid residues. However, forming a designated structure could still be challenging based solely on interactions between amino acid residues. To address this challenge, various molecules can be attached to peptides to further adjust and affect their assembly, thus expanding the possibilities of assembled structure. The resulting peptide-base molecules are often termed “peptide conjugates.” They can assemble into various well-defined nanoscale structures, such as spherical or tubular micelles or vesicles,⁶²⁻⁶³ twisted or coiled nanoribbons,⁶⁴⁻⁶⁵ and two dimensional nanosheets,^{22,66} often *via* non-covalent interactions, such as hydrophobic/hydrophilic interactions, electrostatic interactions, hydrogen bonding, and π - π stacking. Not only do these conjugated moieties facilitate the formation of superstructures, but they also introduce new functionalities, such as cell recognition,⁶⁷ stimuli responsiveness,⁶⁸ and fluorescence labeling.⁶⁹ Conjugation of peptides with other molecules greatly expands their capabilities both as directing agents for self-assembled nanostructures and as biocompatible functional materials.^{29,70-71}

1.2.2 Recognition Abilities of Peptides

In addition to the self-assembly properties of peptides, peptides are also widely used based on their sequence-specific recognition abilities to both biological^{29,72-73} and non-biological materials.⁷⁴ For example, a short peptide sequence, Arg-Gly-Asp (RGD), was identified as the minimal recognition sequence within proteins in the extracellular matrix (ECM) required for cell attachment.⁷⁵⁻⁷⁷ The RGD sequence, or sometimes a longer sequence, Arg-Gly-Asp-Ser (RGDS), has been incorporated into a variety of synthetic materials to promote cell interaction and

adhesion.⁷⁸⁻⁷⁹ For my work, I will focus on the role and capability of peptides to recognize, bind, and influence the synthesis and assembly of inorganic, specifically plasmonic, nanomaterials.

Although both peptides and proteins exist in natural systems and can promote the formation of functional inorganic materials,⁸⁰⁻⁸¹ peptides are obviously less complex in terms of sequence, synthesis, and purification, and peptides could possess the same recognition sequence for inorganic materials as proteins. There are many peptide sequences (Table 1.1) that bind exclusively to a certain inorganic surface which have been identified, selected, and isolated both in natural systems and through laboratory *in vitro* selection.

Table 1.1. Examples of peptide sequences that are known to bind to plasmonic nanoparticles.

Nanoparticles	Sequence	References
Au	AYSSGAPPMPPF	14,82
	DYKDDDDKP	14
	AHHAHHAAD	83-84
	WAGAKRLVLRRE	17
	WALRRSIRRQSY	17
	MHGKTQATSGTIQS	23,85
Ag	AYSSGAPPMPPF	82
	NPSSLRRYLPSD	82,86
	SLTATQPRTTPV	82
Cu	HGGGHGHGGGHG	87

A good example of selection from a natural system is a sequence AHHAHHAAD (HRE) from the histidine-rich protein II of *Plasmodium falciparum* (a unicellular protozoan parasite of humans)⁸⁴ which has been found to mediate the aqueous assembly of Ag and Au clusters, in

addition to several other metal sulfide and metal oxide materials.⁸⁸ Matsui and coworkers showed that the Au precursor-HRE complex forms initially, followed by nanocrystals nucleation.⁸³

In addition to peptide sequences found in natural systems, a wider variety of peptide sequences with inorganic surface binding capabilities have been identified and selected by the phage-display method,⁸⁹ which is illustrated in Figure 1.3. This bio-panning strategy is used to isolate peptide sequences that bind strongly to the inorganic surface of interest. Apparently, the possible peptide sequences selected via phage display are only limited to the number of inorganic surfaces that are tested, thus leading to discovery of peptides having high affinity not only to plasmonic nanoparticles, such as Ag⁸² and Au,⁹⁰⁻⁹² but to other inorganic materials including ZnO,⁹³⁻⁹⁴ GaAs,⁴⁰ Pt,^{88,95} Pd,⁸⁸ CdS,⁹⁶⁻⁹⁸ ZnS,⁹⁸ FePt,⁹⁹ and Ti.¹⁰⁰⁻¹⁰¹ It should be noted that many of the peptides listed above are able to mineralize inorganic materials at room temperature, where preparation of the corresponding inorganic nanomaterials can be easily conducted at mild conditions.

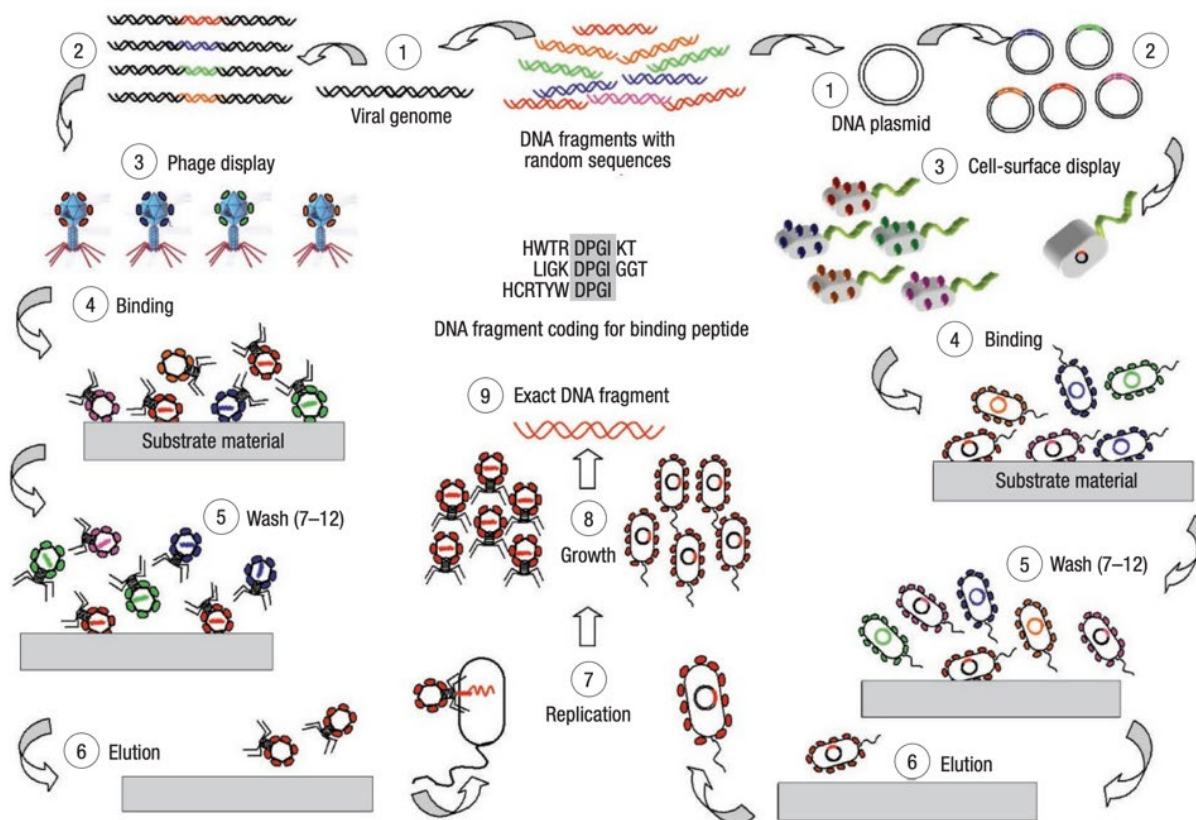


Figure 1.3. Phage display and cell-surface display. Reproduced with permission from ref.⁸⁹ Copyright 2003, Nature Publishing Group.

1.2.3 Peptide Scaffolds for Nanoparticle Superstructures

As discussed above, peptides are ideal candidates for constructing nanoparticle superstructures due to their unique self-assembly and surface-recognition capabilities. The process of constructing nanostructures using peptide-based materials usually involves the following steps: 1) peptides assemble into a defined template structure such as one-dimensional linear fibers or spherical vesicles; 2) synthesis and purification of constituent plasmonic nanoparticles (NPs); and 3) assembly of NPs onto constructed peptide scaffolds. Alternatively, the assembly of the peptide scaffold and the nucleation and growth of the NPs can be combined in a one-pot synthesis to yield a NP superstructure. I will present each of these methods in the following sections.

1.2.3.1 Step-wise Assembly of Nanoparticles

Starting from early examples, research on assemblies of plasmonic NPs mediated by peptide molecules focused on two directions: 1) discovery of new peptide candidates for new structures, and 2) control over structure parameters based on rational design and modification of peptide molecules.

One of the earliest examples of one-dimensional AuNP single chain assembly was demonstrated by Matsui and co-workers in 2002 (Figure 1.4).⁸³ They showed that a histidine-rich peptide with the sequence AHHAHHAAD could be immobilized at the amide binding sites of 1-D fibers assembled using a heptane dicarboxylate molecule derivative. After incubating with a gold precursor, ClAuMe₃, nucleation of Au nanocrystals occurred on the surface of the fiber upon addition of a reducing agent NaBH₄, leading to formation of Au NP-coated nanowires. Although the peptide itself was not integral to the structure of the 1-D fiber, this unique result showcased the capability of peptides as agents for directing NP assembly onto 1-D scaffolds.

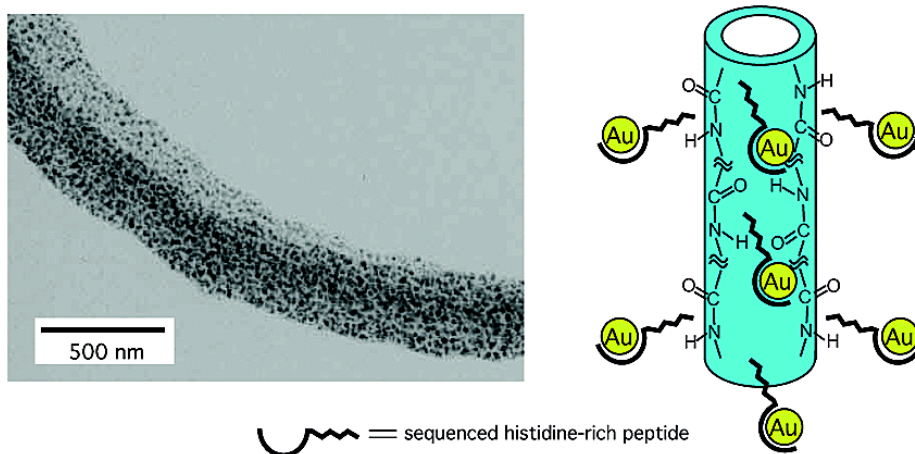


Figure 1.4. Au nanowire by histidine-rich peptide nanotubules. Reproduced with permission from ref.⁸³ Copyright 2002, American Chemical Society.

A short time later in 2003, Fu *et al.* reported the preparation of double-helical arrays and single-chain arrays of Au and Pd nanoparticles based on peptide fibrilization (Figure 1.5).¹⁰² Peptide fibrils assembled using a synthetic 12-mer peptide, T1, served as a template for depositing pre-synthesized Au or Pd nanoparticles. The NPs anchored onto the peptide fibrils through electrostatic interactions between the positively charged peptide scaffold and the negatively charged Au or Pd NPs. It was found that the structure of the assemblies could be influenced by the pH of the reaction media and the size of the Au or Pd NPs.

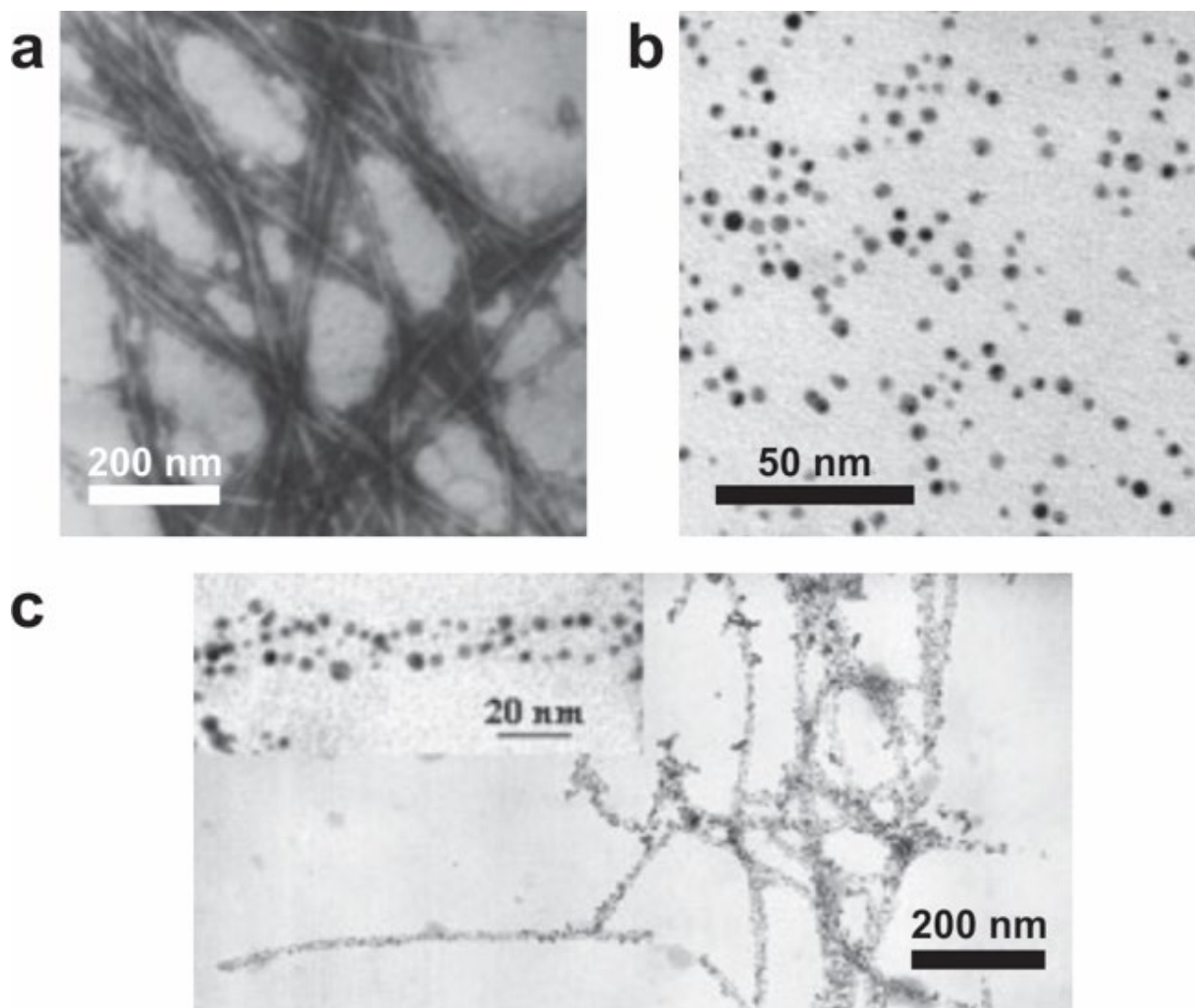


Figure 1.5. Double helical Au NP assembly based on peptides. TEM images of (a) T1 peptide fibrils, (b) Au colloidal NPs, and (c) double helical assembly of Au NPs directed by T1 peptide at pH = 6. Reproduced with permission from ref.¹⁰² Copyright 2003, Wiley-VCH.

Stupp *et al.* described the preparation of a new 1-D assembly of Au NPs via co-assembly of a tripeptide fiber-forming amphiphilic molecule and a thymine containing molecule (Figure 1.6).⁶³ The co-assembly of the two molecules in the organic solvent CCl_4 afforded nanofibers, which were then decorated by diaminopyridine (DAP) functionalized Au NPs, forming a long, linear chain-like superstructures of assembled Au NPs. Diphenylalanine (FF) peptide is a popular dipeptide sequence that exhibits strong capability to assemble into nanofibers,⁶⁰ and it has been

employed in many cases as a nanofiber promoting moiety. Gazit's group proposed a strategy of co-assembling several FF containing short peptides into nanotubes, which served as scaffold organizing for Ag and Au NPs.¹⁰³

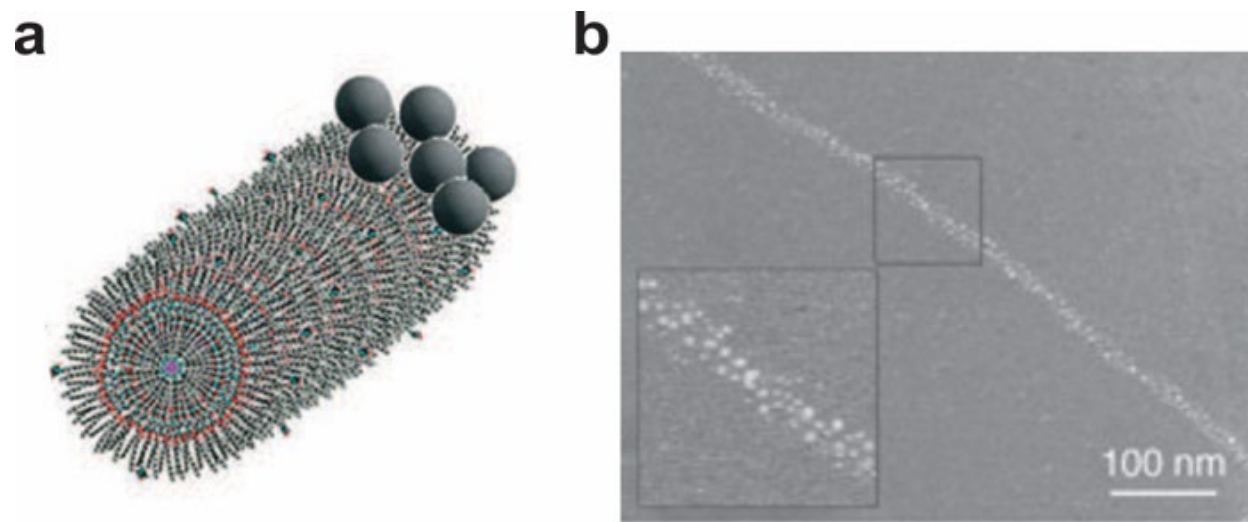


Figure 1.6. Schematic (a) and TEM images (b) of a tripeptide, fiber-forming amphiphile assisted linear assembly of Au NPs. Reproduced with permission from ref.⁶³ Copyright 2005, Wiley-VCH.

In addition to the static assemblies described above, peptides have also been used to prepare dynamic assembly systems. Liedberg *et al.* presented an example of controlling the aggregation state of peptide-capped Au NPs via Zn^{2+} ion-induced peptide folding.¹⁵ Upon addition of Zn^{2+} ions, the polypeptides JR2E, immobilized on the surface of Au NPs, experienced dimerization and folding between two different peptides located on separate particles, thus leading to aggregation of particles. This example provides a new strategy for designing peptide-based Au NP superstructures in a dynamic manner based on responsive behavior of the capping peptides.

It should be emphasized that there exists a multitude of natural and non-natural peptide- and protein-based fiber nano-assemblies, and the examples detailed above serve as proof of principle that such fibers can serve as templates for the deposition of inorganic NPs. However,

such methods do not allow for a sufficient level of synthetic control necessary for fine-tuning structures and optimizing properties.¹⁰⁴

1.2.3.2 One-Pot Synthesis of NP Superstructures

In the previous section, I discussed how plasmonic NP superstructures were designed and constructed via step-wise syntheses, and we highlighted some of their potential applications. The assembly strategy usually involves 1) peptide template construction, 2) NP synthesis and purification, and 3) NP superstructure formation on the peptide template. It should also be noted that sometimes steps 1) and 2) may occur in a single step where peptide template formation is mediated by a metal precursor. However, combining all of the synthetic steps in a single one-pot procedure may be simpler in practice and reduce the complexity of sample preparation.

Our group developed a one-pot peptide-based strategy for synthesizing and assembling NP into structurally well-defined NP superstructures (Figure 1.7). We have used this strategy to prepare diverse classes of Au NP superstructures, including hollow spheres, double helices, and single helices. These materials were constructed using peptide conjugate molecules that incorporate the Au binding peptide,^{14,82} AYSSGAPPMPPF (termed A3 or PEP_{Au}, identified and isolated via phage display method). The peptide conjugates are designed in such a way that they will assemble into a target assembly, such as a 1-D fiber or a spherical vesicle. In a typical NP superstructure synthesis, a specific Au-binding peptide conjugate molecule (R-PEP_{Au}) is dissolved in a mild reducing buffer 4-(2-hydroxyethyl)-1-piperazineethanesulfonic acid (HEPES). Then an aliquot of dissolved Au salt is added. During the synthesis, the Au salt is reduced by the HEPES buffer, forming Au NP. Simultaneously, the Au-binding peptide conjugates bind to the Au particles *and* direct their assembly into a superstructure. The morphology of the NP superstructure is dictated by the assembly of R-PEP_{Au}. In essence, all of the structural features of the product NP

superstructure can be programmed into R-PEP_{Au} at the design stage. R-PEP_{Au} is highly tailorable. The 'R' group can be any organic molecule (e.g., aliphatic, aromatic, etc.) and can be designed to be responsive to external stimuli. The PEP_{Au} sequence can also be modified. Members from our group realized that the N-terminal amino acids of PEP_{Au} (AYSSGA) engage in β -sheet formation, which facilitates the assembly of some R-PEP_{Au} into twisted amyloid-like fibers. This β -sheet region can be modified to adjust the assembly propensity by adding additional hydrophobic amino acids, for example. Finally, the chirality of the amino acids themselves can be either R or S, which can impact the chirality of the resulting assembly. Below, I highlight some of the unique materials prepared using this methodology.

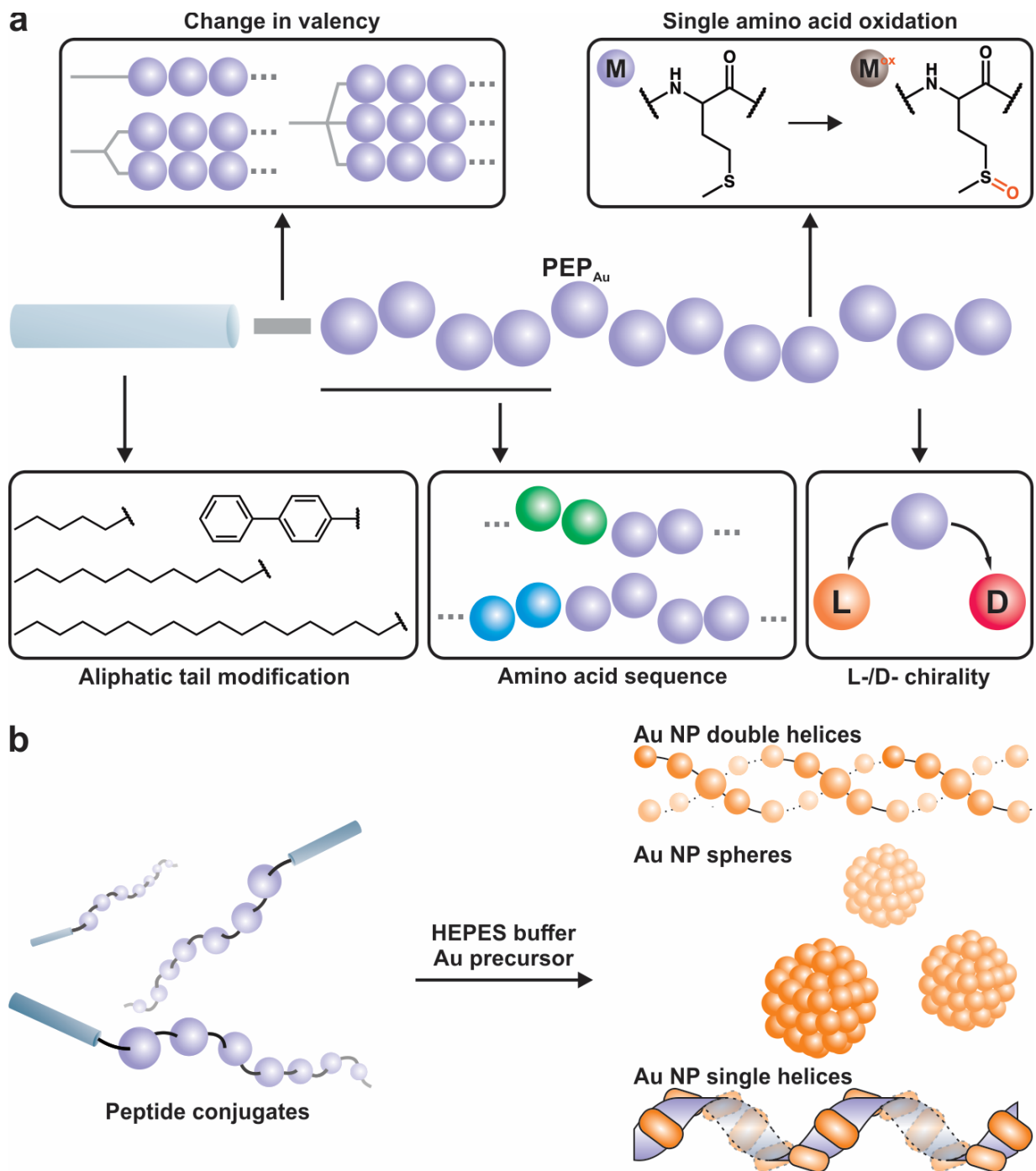


Figure 1.7. Schematic representation of examples of modification of peptide conjugates and some resulting Au NP superstructures directed by peptide conjugates. (a) Many aspects of peptide conjugates can be systematically modified such as aliphatic tails, valencies, amino acid sequences and chirality, and oxidation state of single amino acid residue. (b) When a certain type of peptide conjugates is dissolved in HEPES buffer in the presence of an Au precursor, various Au NP superstructures are obtained depending on the kind of peptide conjugate chosen.

As a first demonstration of the utility of this synthetic method, C_{12} -PEP_{Au} (a 12-carbon aliphatic chain conjugated to PEP_{Au}) was used to direct the synthesis and assembly of AuNP double helices (Figure 1.8a-c).¹⁶ It should be highlighted that the assembled Au NP double helices exhibited exceptional structural fidelity; that is, the Au NPs were fairly mono-dispersed (~8 nm), the helical pitch was consistent (~83 nm), and the predominant product in the synthesis was Au NP double helices. Many structural features, such as NP size and interparticle distances, could be further tuned by adjusting synthetic conditions (Figure 1.8d-f).¹⁰⁵ A molecular model for the peptide conjugates was proposed which was then used for the design and rational construction of future superstructures.

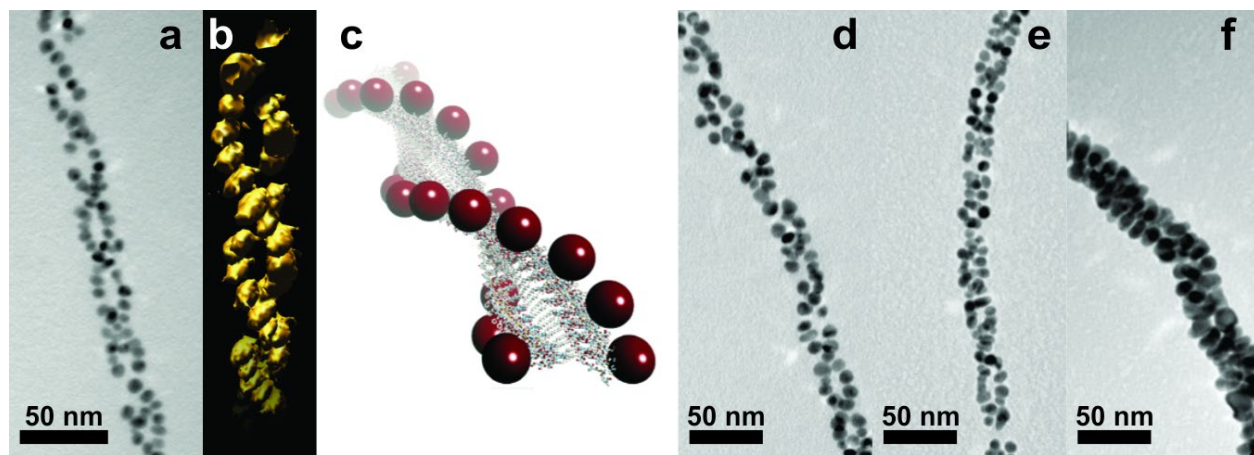


Figure 1.8. Double helical Au NP superstructures. TEM image (a), rendered tomographic reconstruction image (b), and schematic model (c) of Au NP double helical superstructures directed by peptide conjugate C_{12} -PEP_{Au}. Structural parameters such as constituent NP size (d-f) could be tuned for Au NP double helices. (a-c) Reproduced with permission from ref.¹⁶ Copyright 2008, American Chemical Society. (d-f) Reproduced with permission from ref.¹⁰⁵ Copyright 2010, American Chemical Society.

Due to the helical nature of the superstructure, the Au NP double helices exhibited circular dichroism (CD) at the plasmon frequency. As a result, it could be rationally proposed that the handedness of the superstructures could be tuned by using left- or right-handed constituent amino

acids. It was then demonstrated that conjugates consisting of all L-amino acid residues yielded left-handed helices and D-amino acid right-handed,¹⁰⁶ and mirrored CD signals were observed for these two assemblies, respectively (Figure 1.9). The experimental CD signals also corresponded well with computational results. These findings demonstrated that rational molecular level modification of the peptide conjugate could be used to control the assembly and chiroptical properties of the helical superstructure.

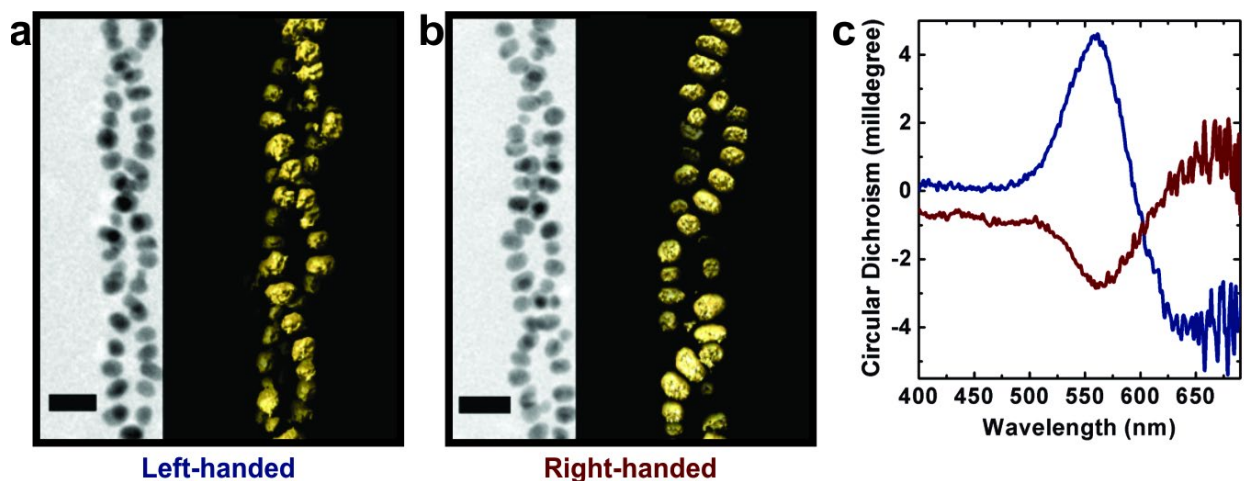


Figure 1.9. Chirality of the Au NP double helices could be dictated by using all L- or D-amino acids for C_{12} -PEP_{Au} conjugates. (a) Left- and (b) right-handed Au NP double helices are observed under TEM. Scale bar = 20 nm. (c) Mirrored chiroptical signals are observed for the two superstructures respectively. Reproduced with permission from ref.¹⁰⁶ Copyright 2013, American Chemical Society.

A variety of other superstructures were also prepared by systematically modifying the composition of the peptide conjugate. These modifications focus on the following aspects of the conjugates: 1) R-group, 2) the valency of the conjugate (number of the peptides attached to one R-group), and 3) amino acid residues. For example, as an early attempt to explore this strategy, biphenyl groups were conjugated to PEP_{Au} instead of the C_{12} aliphatic.¹⁰⁷ It was reasoned that peptide assembly could be promoted due to the π - π stacking interactions of the biphenyl groups. The biphenyl-PEP_{Au} promoted formation of 1-D AuNP assemblies along the peptide fibers.

Based on known design principles for amphiphile assembly, it was known that the length of the aliphatic component could potentially affect the assembly morphology of a peptide conjugate.¹⁰⁸ Thus, tuning the length of the aliphatic chain could lead to variation in the morphology of Au NP superstructures. Following this strategy, spherical Au NP superstructures were prepared by using the peptide conjugate, C₆-AA-PEP_{Au} (a 6-carbon chain conjugated to PEP_{Au} spaced by two additional alanine residues) (Figure 1.10a-c).²⁰ A shorter aliphatic chain allowed for the formation of peptide vesicles instead of peptide fibers. Furthermore, the size of the spherical Au NP superstructure could be tuned by carefully adjusting the synthetic conditions.²⁴ The resulting Au NP spheres exhibit a hollow interior. Taking advantage of this feature, it was further shown that these spherical superstructures had potential application in drug-loading and release (Figure 1.10d).¹⁰⁹ More specifically, it was demonstrated that the Au NP spheres could take up a common drug doxorubicin (DOX), and upon addition of proteinase K, a non-specific peptidase, large Au NP superstructures (~150 nm in diameter) started to release DOX upon digestion of the peptide scaffold. Additionally, in the presence of light irradiation at 805 nm, both large and medium (~70 nm in diameter) Au NP spheres showed degradation behavior which led to the release of DOX.

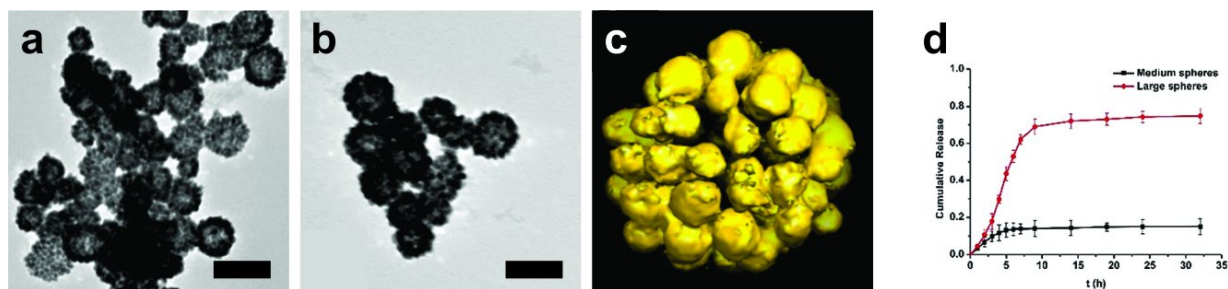


Figure 1.10. Spherical Au NP superstructures constructed using C₆-AA-PEP_{Au}. (a, b) TEM images of Au NP spherical superstructures. (c) 3-D surface rendering of the tomographic volume of Au NP spheres. Reproduced with permission from ref.²⁰ Copyright 2010, American Chemical Society. (d) Cumulative release profile of DOX-loaded Au NP spheres. Reproduced with permission from ref.¹⁰⁹ Copyright 2015, Royal Society of Chemistry.

In 2016, a new class of single-helical superstructure with tunable features was constructed using $C_x\text{-(PEP}_{\text{Au}}^{\text{M-ox}})_2$ ($x = 16\text{-}22$, M-ox indicates methionine sulfoxide), in which two PEP_{Au} sequences were tethered to the same aliphatic tail (Figure 1.11a-f).^{25,27-28} This family of peptide conjugates assemble into helical ribbons and the Au NPs decorating the helical ribbons were consequently assembled in a single-helical fashion. As the tail length increases from C_{16} to C_{22} , the pitch length of the Au NP helices increases from ~ 80 nm to ~ 128 nm, while the size of the constituent Au NPs decreases from ~ 14 nm to ~ 6 nm. Meanwhile, the intensity of the corresponding chiroptical signals of the Au NP single helices, which was predicted to be inversely proportional to pitch length, decrease as the aliphatic tail length increases from C_{16} to C_{22} . The CD response of the single helices formed using $C_{16}\text{-(PEP}_{\text{Au}}^{\text{M-ox}})_2$ and $C_{18}\text{-(PEP}_{\text{Au}}^{\text{M-ox}})_2$, as quantified by the g -factor (anisotropic factor), were the highest not only among this family but also among the highest reported for helical NP assemblies ($\sim 0.02\text{-}0.04$). This example demonstrated that simple chemical modifications could be employed to control the helical pitch, the nanoparticle size, and the chiroptical properties within a family of helical nanoparticle superstructures.

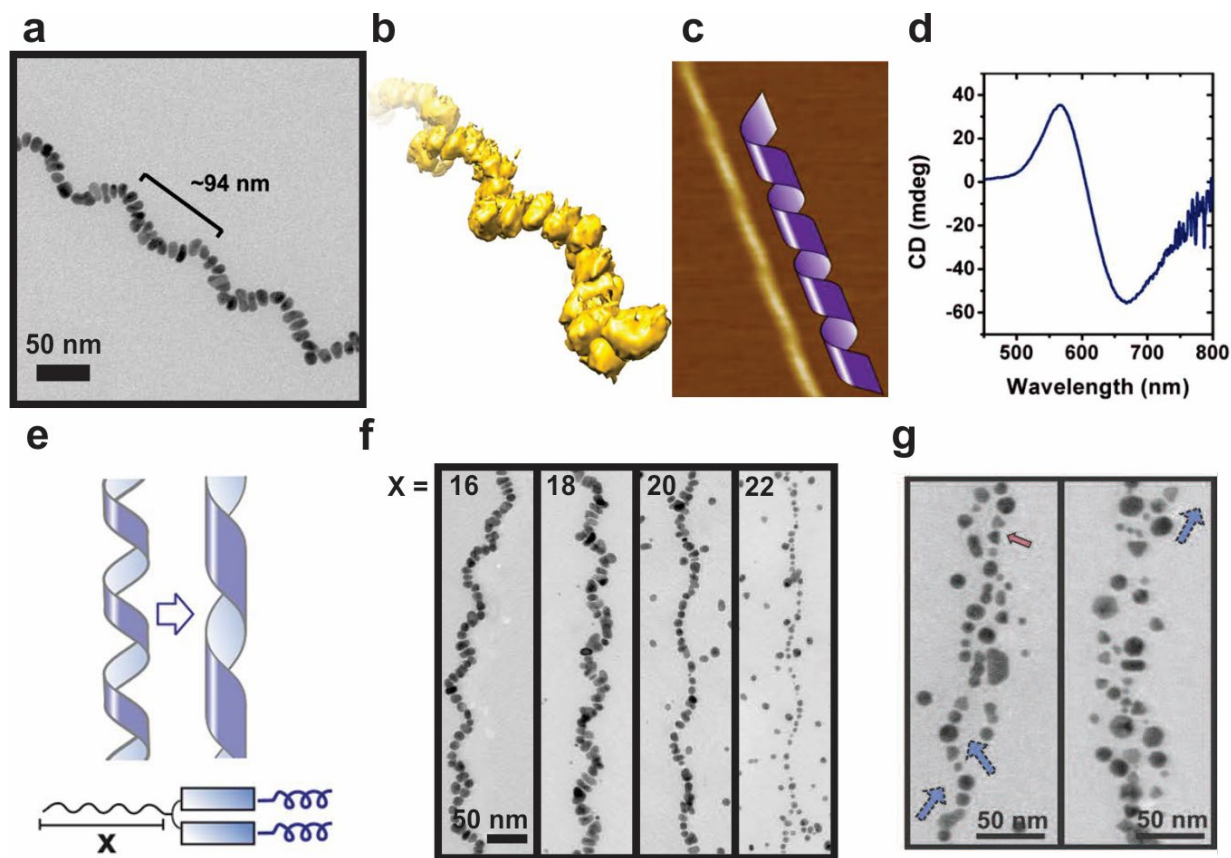


Figure 1.11. Single helical Au NP superstructures. (a) TEM image and (b) 3-D rendering of tomographic rendering of single helical Au NP superstructures directed by peptide conjugate $C_{18}-(PEP_{Au}^{M-ox})_2$. (c) AFM mapping and schematics representation of the underlying coiled ribbon assembly of peptide conjugate. (d) The resulting Au NP single helices showed enhanced chiroptical response with a g -factor of 0.02. Reproduced with permission from ref.²⁷ Copyright 2016, American Chemical Society. (e) Schematic illustration of tuning structural features of single helix assembly by modifying the aliphatic tail of peptide conjugate $C_x-(PEP_{Au}^{M-ox})_2$ ($x = 16-22$). (f) TEM images of single helical Au NP assembly directed by conjugates $C_x-(PEP_{Au}^{M-ox})_2$ ($x = 16-22$). Reproduced with permission from ref.²⁸ Copyright 2017, American Chemical Society. (g) Adding auxiliary particle capping agents to the synthesis of Au NP single helices introduced anisotropy to constituent particles. Reproduced with permission from ref.¹¹⁰ Copyright 2018, Wiley-VCH.

Some features of the assembled structures, such as metrics and morphology, could be further adjusted by introducing external reagents. Citrate, another particle capping agent, could be used to affect the dimensions of the NP within the superstructures.¹⁰⁵⁻¹⁰⁶ Likewise, it was recently demonstrated that adding an external surfactant, cetyltrimethylammonium bromide (CTAB), could

promote anisotropy in the Au NPs within the single-helical superstructures,¹¹⁰ where hexagonal and prismatic particles were observed within the superstructure (Figure 1.11g).

As detailed above, this one-pot, single-step methodology is a straightforward and highly tunable approach for building well-defined Au NP superstructures. Programmable control over the molecular structure of the peptide conjugates allows one to design a diverse collection of superstructures and fine tune their morphology, structural parameters, and physical properties.

1.3 Reversible Assemblies of NPs

The nanoparticle assemblies described above are static in that they do not undergo any significant morphological transitions once they are fabricated. The fabrication and study of dynamic nanoparticle assemblies that are programmed to undergo switchable morphological transitions is a frontier in nanoparticle assembly research. The complex and sophisticated functions of many natural materials are due to some form of responsiveness or reorganization of building blocks in response to external stimuli. These functions and behaviors, such as phototaxis,¹¹¹⁻¹¹² camouflage,¹¹³⁻¹¹⁵ self-healing,¹¹⁶ homeostasis,¹¹⁷⁻¹¹⁸ and signal amplification,¹¹⁹⁻¹²¹ usually originate from dynamic responses of constituent building blocks of biological systems: amino acids, peptides and proteins. Although it is still premature for chemists to fully reproduce the complexity and delicacy delivered by natural systems, research has never stopped toward introducing nature-inspired stimuli-responsiveness to existing building blocks¹²²⁻¹²³ in order to impart switchable optical, catalytic, and electronic properties. Among these building blocks, NPs are particularly attractive. As discussed above, the NPs could be synthesized with different sizes, shapes and compositions, each with unique properties. In addition, by carefully tuning the surface

chemistry of NPs, it is easy to control the degree of aggregation/assembly, which could further impact the chemical and physical properties.

Many different external stimuli could be used to initiate a morphological transition for a nanoparticle superstructure. Common stimuli include light,^{43,53,124-136} temperature,¹³⁶⁻¹⁴¹ pH,^{47,142-143} metal ions,^{18,144-145} gases,^{127,146-147} electric fields,¹⁴⁸⁻¹⁵⁰ magnetic fields,¹⁵¹⁻¹⁵³ and biomacromolecules (DNA,¹⁴⁰ protein,⁵⁸ enzyme,^{31,154} etc.). Sometimes, one nanostructured material can even simultaneously respond to more than one type of stimuli. In the following subsections, I will present a selection of these stimuli and how they impact the NP and their assemblies, which will ultimately lead to my motivation to study dynamic Au NP assemblies using photo-responsive peptide conjugates.

1.3.1 Light

Among the abovementioned stimuli, light is probably the most popular one due to several reasons: 1) it is an external stimulus which can be delivered remotely; 2) one can precisely control the location where the photo-irradiation is applied; 3) the degree of response could be controlled by the time length of irradiation; and 4) different reactions could be triggered based on the wavelength of the light selected. A common model for constructing dynamic NP assemblies is to introduce photo-responsive moieties, such as azobenzenes, to the capping ligands of metallic NP building blocks. As shown in Figure 1.12, upon UV irradiation, the stable *trans* azobenzene rapidly isomerizes into the relatively unstable *cis* conformation, resulting in changes in two aspects – geometry and polarity: the linear, non-polar *trans* azobenzene isomerizes into the bent, polar *cis* conformation. Either visible light irradiation or thermal relaxation could induce the *cis* \rightarrow *trans* isomerization. Consequently, for the NP building blocks, the distances between capping ligands

or between NPs and the surface polarity of NPs can be adjusted and tuned, leading to the disassembly, aggregation, or reorganization of NP building blocks depending on the capping ligand and solvent used.^{135,155} Moreover, the assembly-disassembly can be often repeated for multiple times due to the chemical robustness of azobenzene.

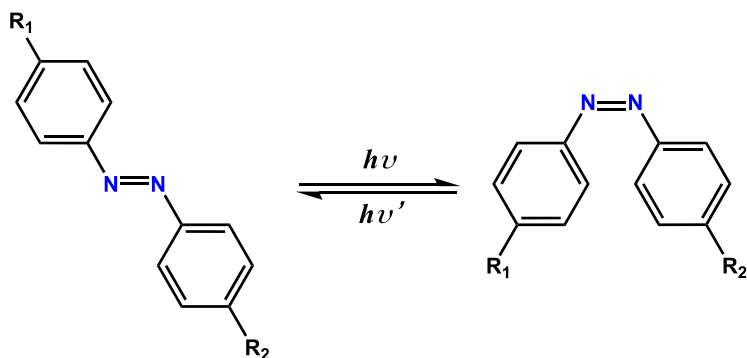


Figure 1.12. Photo-isomerization of azobenzene.

As mentioned in previous sections, one of the most interesting properties of plasmonic NPs and their assembly is the LSPR. Thus, controlling the assembly or disassembly of these NPs leads to a change in color. An early endeavor to control the assembly/disassembly of NPs was made by Prasad and coworkers.¹⁵⁵ As shown in Figure 1.13a, they prepared a Au NP network linked by an azobenzene thiolated ligand. The linkage ligand consists of two thiols “arms” connected by an azobenzene moiety. Upon UV or visible light irradiation, interparticle distances decreased or increased, respectively, due to the *trans-cis* photo-isomerization of azobenzene. The resulting change in interparticle distances induced a red or blue shift in the LSPR peak of the Au NP network. Klajn and coworkers presented a similar work to control the LSPR of NPs, however, with more precise control of NP – creating crystal-like NP assembly (Figure 1.13b).¹³¹ Using a dithiol ligand, upon light irradiation, NPs could assemble into highly-ordered, three dimensional reversible or irreversible superstructures: light-reversible or irreversible crystals or NP superspheres of various sizes. They can also control the degree of crystal formation based on the

strength of the light applied, the dipole-dipole interactions between the NPs, and the ligand coverage on the NPs. Not only do these assembly morphologies exhibit different LSPR bands, but for some the reversible assembly could be repeated multiple times. Klajn *et al.* also prepared a self-erasable nanoparticle “ink”.¹²⁹ An organogel-based film was soaked with Au or Ag NPs functionalized with thiolated azobenzene ligands (Figure 1.13c). Upon UV irradiation, the color of the NP embedded film turned purple, which later turned back to pink after illumination by visible light or thermal relaxation. If a certain area of the film was covered by a mask pattern, only the exposed area of the film would be irradiated by UV light, leading to customized patterning of the film. It should also be noted that the lifetime of the pattern could be easily controlled by adjusting the coverage ratio of the azobenzene ligand on the surface of the nanoparticle.

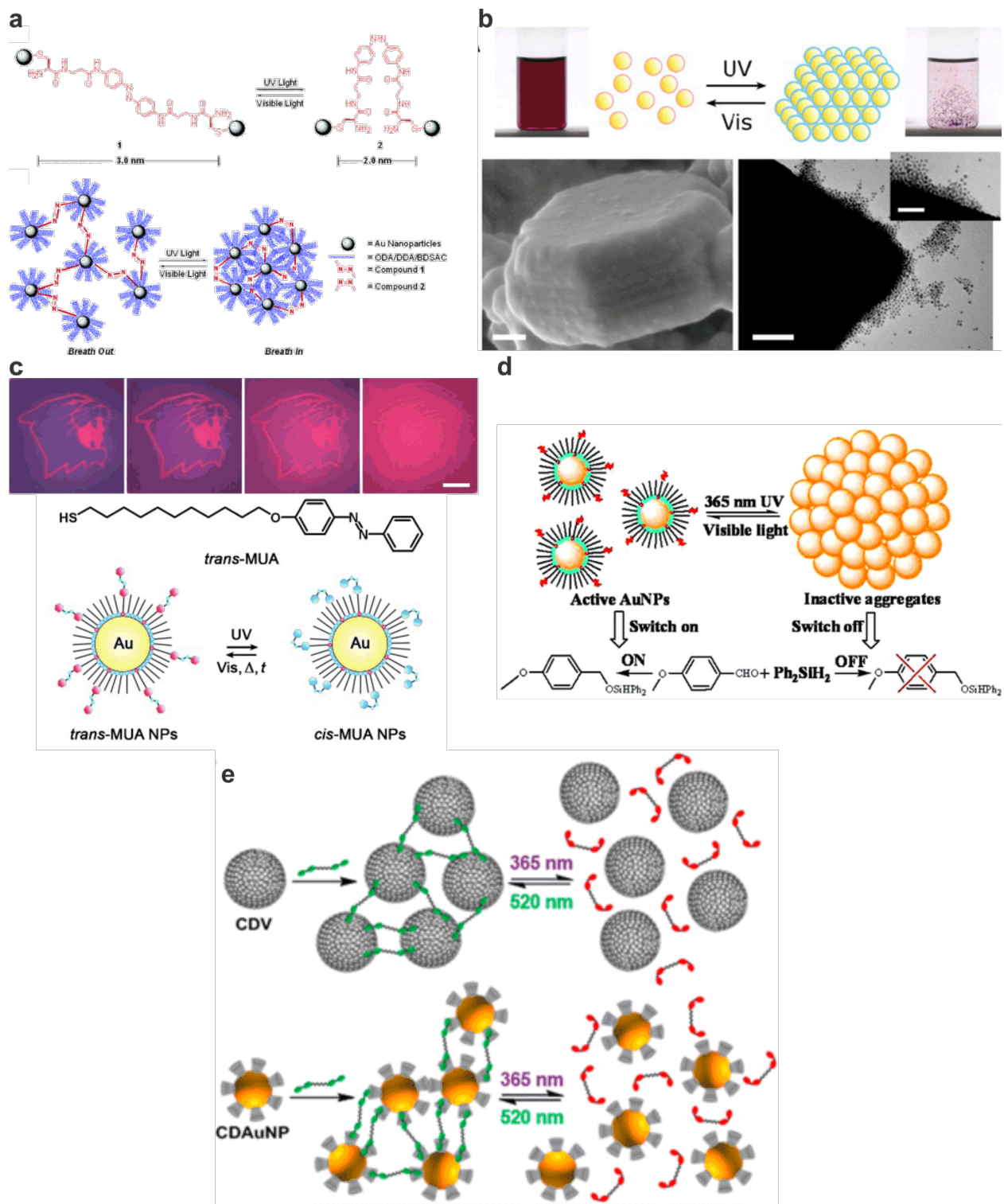


Figure 1.13. Controlling NP assembly using light. (a) An early example of controlling aggregation of Au NPs by functionalizing the surface of Au NPs with a dithiolated azobenzene ligand. Reproduced with permission from ref.¹⁵⁵ Copyright 2005, American Chemical Society. (b) Assembling Au NPs into well-defined crystalline superstructures using light. Reproduced with permission from ref.¹³¹ Copyright 2007, The National Academy

of Sciences of the USA. (c) Light-induced self-erasable film doped with photo-responsive Au NP. Reproduced with permission from ref.¹²⁹ Copyright 2009, Wiley-VCH. (d) Catalysis that can be turned “on” and “off” by using photo-responsive Au NPs. Reproduced with permission from ref.⁵³ Copyright 2010, American Chemical Society. (e) Tuning Au NP assembly and disassembly based on azobenzene- β -CD host-guest interactions. Reproduced with permission from ref.¹⁵⁶ Copyright 2016, American Chemical Society.

One other interesting feature of NPs is their catalytic activity. Researchers from Grzybowski’s group designed a photoswitchable catalytic system induced by dynamic aggregation of Au NPs (Figure 1.13d).⁵³ A hydrosilylation reaction could be turned “on” and “off” based on active, disassembled Au NPs and inactive, aggregated Au NPs, respectively. As the Au NPs were functionalized by azobenzene thiolated ligands, the transition between disassembled and aggregated Au NPs was easily induced by shining UV and visible light, respectively.

In addition to using azobenzene alone for reversible assembly of NPs, researchers from Ravoo’s group designed an azobenzene-cyclodextrin host-guest system to access reversible self-assembly by light (Figure 1.13e).¹⁵⁶ Azobenzene is known to interact with cyclodextrin molecules, with the *trans* isomer residing inside the cyclodextrin (in this case, β -cyclodextrin or β -CD) cavity; whereas the *cis* isomer becomes detached from the β -CD molecule. By using bis-arylazopyrazole as the non-covalent, photo-responsive “glue”, they were able to construct assemblies with Au NP functionalized with β -CD. Similar to azobenzene, arylazopyrazole can be toggled between *trans* and *cis* conformations by illuminating samples with UV or visible light; however, arylazopyrazole showed higher efficiency in photo-isomerization and higher thermal stability in *cis* isomer than azobenzene. The disassembly-reassembly cycle could, thus, be repeated for multiple times without observable fatigue.

1.3.2 Other Stimuli

1.3.2.1 Temperature

Apart from light, other triggers are also widely studied and utilized in preparing dynamic NP assemblies. For example, temperature is a readily accessible stimulus that can be delivered universally to a sample. A common strategy is to use elevated temperatures to induce NP disassembly. Lewandowski, Górecka *et al.* synthesized thermally responsive Ag NPs, whose surfaces were fabricated with liquid-crystal-like molecules.¹³⁹ Capitalizing on the temperature dependent phase transitions of liquid crystals, they were able to manipulate the ordered or amorphous assembly of Ag NPs by cooling or heating the sample, respectively. In some cases, increasing the temperature can also induce assembly of NPs. Bishop and coworkers found that equal amounts of positively and negatively charged Au NPs were stable as a colloidal solution in a high ionic strength solution at 10 °C, but the Au NP started to aggregate when the temperature was elevated to 40 °C.¹³⁸ The charge-driven assembly was attributed to the desorption of stabilizing ions which was responsible for the colloidal stability of Au NPs at low temperatures. When temperature increased, the Au NPs with positive and negative charged aggregated due to Coulombic interactions.

1.3.2.2 Biomolecules

Biomolecules can also trigger assembly or disassembly, which is one of the underlying driving forces for living systems. An early example using DNA as the input switch was demonstrated by Hazarika and coworkers.¹⁴⁰ The aggregation of two kinds of Au NPs modified with two distinct DNA sequences (A and B) was initiated by inputting a DNA strand, F_a , complementary to both A and B. The reverse process – disassembly – was triggered by inputting

a DNA strand, F_d , complementary to F_a . Furthermore, the assembly-disassembly cycle could be repeated for several cycles, only leaving the F_a - F_d DNA duplex as the chemical waste. Proteins are also potentially useful for controlling the reversible assembly of NPs. Gurunatha *et al.* succeeded in assemble Au NPs based on artificial repeat proteins.⁵⁸ The strong pairing of two proteins, A3 and $\alpha 2$, induced Au NPs functionalized with these two proteins to co-assemble upon mixing. The degree of co-assembly could be easily controlled by the ratio of the protein to the NPs.

1.3.2.3 pH

Another popular stimulus among researchers is pH. Since the colloidal stability of NPs is largely dependent on the NP surface charge, it is only natural for chemists to assemble or disassemble NPs by changing the pH of the solution. By grafting the NPs with pH-responsive ligands, assembly or disassembly can occur in acidic or basic environments. Grzybowski and coworkers modified Au NP with a 2-fluoro-4-mercaptophenol ligand, whose protonation and deprotonation took place around neutral pH.¹⁵⁷ When the pH decreased from ~ 9 to ~ 7 , deprotonation of the terminal $-O^-$ groups led to assembly of Au NPs, while the reverse process of assembly occurred for NPs modified with basic ligand.

1.4 Objectives of the Dissertation

My research has focused on the development of peptide-based methods for building NP superstructures that can undergo morphological transitions in response to light and elucidating the

factors that influence the stability of peptide-based nanoparticle superstructures in various conditions.

In Chapter 2, I introduce an azobenzene moiety, a photo-responsive switch, to a gold-binding peptide conjugate to induce light-triggered reversible assembly of one-dimensional Au NP superstructures. A family of peptide conjugates were synthesized with systematically tuning of organic tail and β -sheet sections of the conjugates, allowing for systematic tuning of reversible morphology transitions of Au NP superstructures upon UV or visible light irradiation. Hydrophobic-hydrophobic interactions and β -sheet hydrogen bonding interactions are adjusted to carefully control the transitions between one-dimensional and spherical Au NP superstructures.

Inspired by the findings in Chapter 2, I continue to explore other possibilities based on the azobenzene peptide conjugates. In Chapter 3, I utilized the photo-induced host-guest interaction between azobenzene and β -cyclodextrin (β -CD) to establish a novel strategy for directing the assembly of discrete Au NPs into one-dimensional superstructures using UV irradiation. Discrete Au NPs were first synthesized using the azobenzene/ β -CD conjugates, where the bulky azobenzene/ β -CD conjugate inhibited assembly of Au NPs into a well-defined superstructure. Upon UV light irradiation, the β -CD was released from the peptide conjugates, allowing for assembly of one-dimensional Au NP superstructures.

Chapter 4 describes a systematic study of the stability of Au NP single helices in the presence of three environmental conditions: elevated temperature, and two peptide denaturants, protease K (ProK) and urea. I found that the stability of the Au NP single helices could be enhanced by increasing the constituent NP size within the Au NP single helices.

2.0 Design and Preparation of Photo-Responsive Peptide Conjugates for the Construction of Gold Nanoparticle Superstructures Having Photo-Regulated Morphological Transitions

This work is completed with collaboration with Andrea D. Merg, Dapeng Sun, Zhengyi Yang, Peijun Zhang and Nathaniel L. Rosi. A manuscript is in the final stages of preparation.

Azobenzene-based peptide conjugates have been used to control the reversible assembly of gold nanoparticles. A series of peptide conjugates, Azo-(CH₂)_m-A_n-PEP_{Au} (m = 1-3; n = 0-2; PEP_{Au} = AYSSGAPPMPFF), with varied hydrophobic and β -sheet interactions were designed to systematically tune the assembly structure and control the reversibility behavior (Figure 2.1). By increasing the length of the aliphatic spacer or the number alanine residues between the azobenzene moiety and the peptide section, the resulting gold nanoparticle superstructure shifts from spherical to linear and becomes less responsive to UV or visible light irradiation. The results provide new methods for switching the morphology of Au nanoparticle superstructures using light.

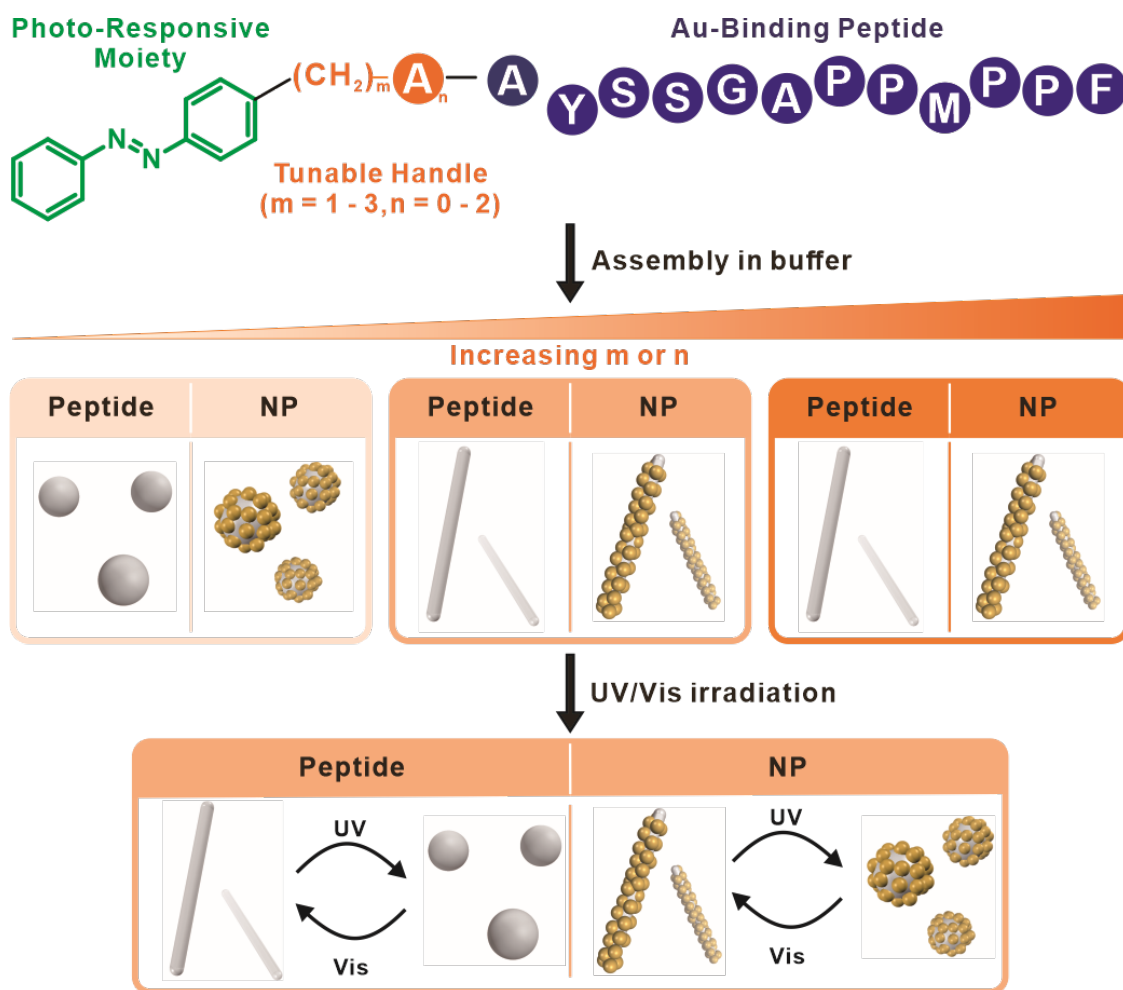


Figure 2.1. Schematic representation of controlling peptide-based photoresponsive Au NP superstructure by systematically modifying peptide conjugates.

2.1 Introduction

Introducing reversibility to nanoparticle superstructures is of great importance in material science as it serves a new route toward development of new stimuli-responsive materials. Nanoparticle superstructures that can undergo a reversible morphological change in response to an external input could potentially be used for a variety of applications including sensing⁴² and drug delivery.⁴³⁻⁴⁷ Compared to other stimuli such as pH^{47,158-159} and temperature,^{137,160}

light^{129,131,155,161-162} is probably the most thoroughly investigated and most broadly used stimulus because it can be controlled remotely at precise location and duration. While there exist many examples of photo-induced aggregation/dispersion of nanoparticles,^{125-127,131} we are not aware of examples that report photo-induced transitions between different well-defined superstructure morphologies. It is well-established that the properties of a NP superstructure depend on the 3-D structure and the organization of nanoparticles within the structure; therefore, creating shape-shifting NP superstructures that can interconvert between different morphologies upon input of a stimulus may allow one to switch the properties of the superstructure on demand. For example, an ultimate goal may be to create superstructures that can switch between chiral and achiral 3-D structure; such materials could be used for chiral sensing or as ‘on/off’ negative index metamaterials.

We have established a peptide-based method to assemble AuNPs into various morphologies and fine-tune their optical and chiro-optical response by systematically modifying the underlying peptide conjugates.^{16,27-28,163} The peptide conjugate serves as a structure-directing agent that directs the assembly of AuNPs into target superstructures. Previous reports from the literature show that azobenzene moieties are useful and efficient for controlling the assembly behavior of peptide assemblies.¹⁶⁴⁻¹⁶⁵ We reasoned that a photo-responsive organic moiety could be appended to the peptide to create photo-responsive peptide conjugates that might be used to create photo-responsive NP superstructures: the π - π stacking between azobenzene moieties would facilitate assembly of the conjugates and, upon UV irradiation, the linear *trans* azobenzene would isomerize into the bent *cis* azobenzene, which could disrupt conjugate packing and assembly and thus affect the assembly and structure of the NP superstructures.

2.2 Results and Discussion

Herein, we report a family of photo-reversible peptide conjugate molecules termed Azo- $(\text{CH}_2)_m\text{-A}_n\text{-PEP}_{\text{Au}}$ ($m = 1\text{-}3$, $n = 0\text{-}2$, Figure 2.2a). In addition to the cis/trans switching of the azobenzene moiety, the conjugates feature two other tunable features: the number of methylene spacers (m) between the peptide and the azobenzene and the number of alanine residues (n) at the N-terminus of PEP_{Au} . The additional methylene groups both increase the distance between the peptide and the photoresponsive azobenzene and increase the length and hydrophobicity of the ‘organic tail’ portion of the conjugate, which could affect assembly morphology and propensity. Additional alanine residues can affect the hydrophobicity of the N-terminus and inter-peptide hydrogen bonding, two factors that can also influence assembly propensity and morphology. By systematically adjusting each component of the peptide conjugates, we envision that the assembly morphology and photo-responsiveness could be carefully modulated.

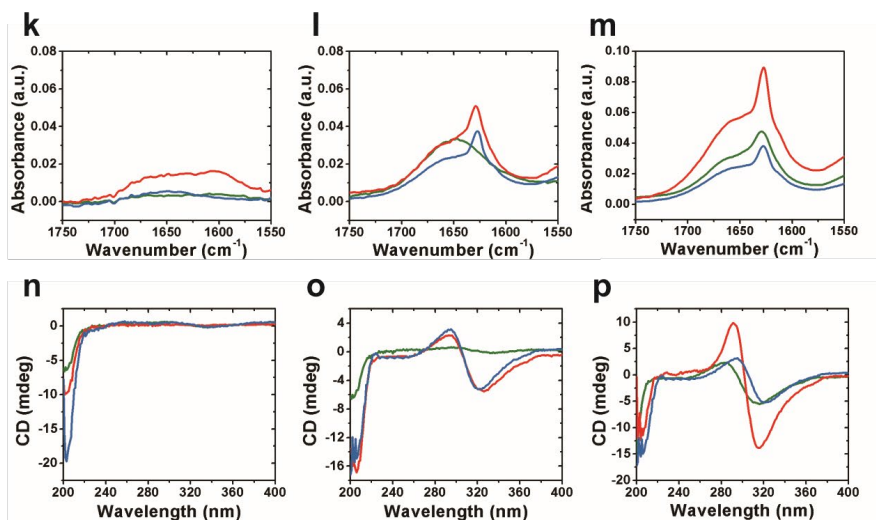
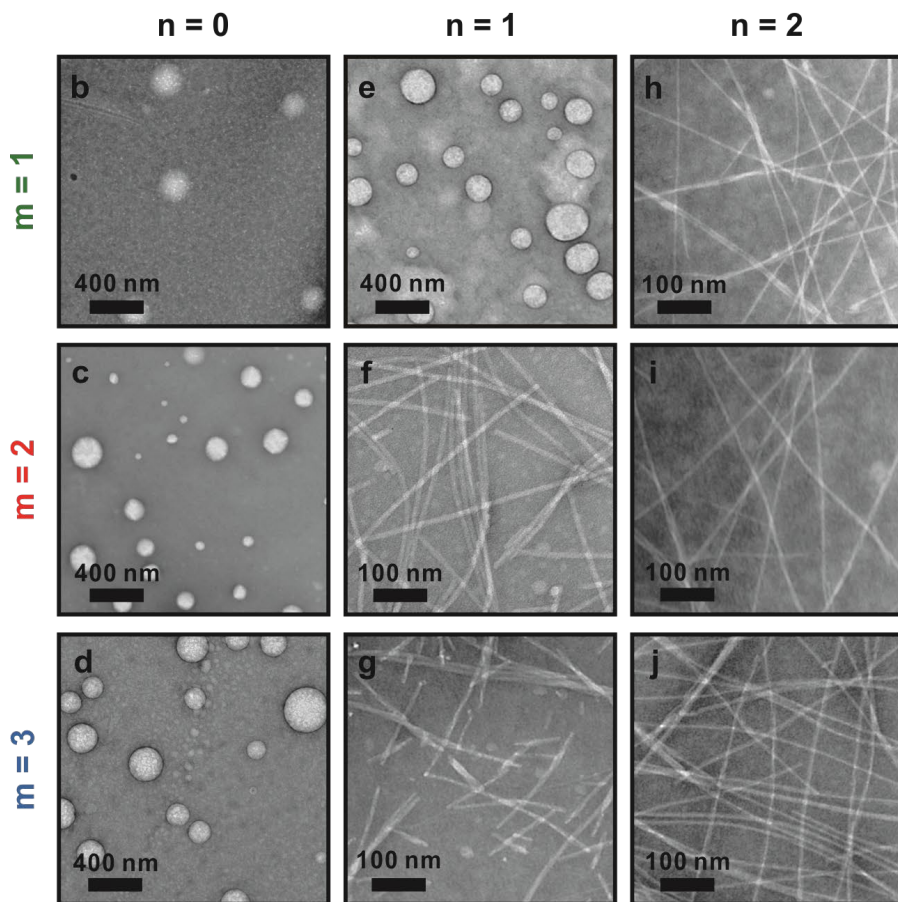
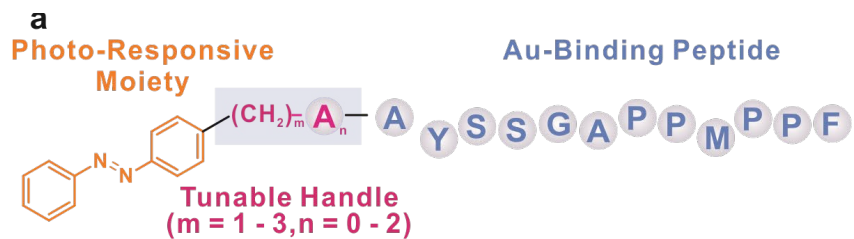


Figure 2.2. (a) Schematic representation of the Azo-(CH₂)_m-A_n-PEP_{Au} (m = 1-3, n = 0-2). (b-j) TEM images of peptide assemblies as a function of number of methylene groups and number of alanine residues: (b) Azo-(CH₂)₁-A₀-PEP_{Au}, (c) Azo-(CH₂)₂-A₀-PEP_{Au}, (d) Azo-(CH₂)₃-A₀-PEP_{Au}, (e) Azo-(CH₂)₁-A₁-PEP_{Au}, (f) Azo-(CH₂)₂-A₁-PEP_{Au}, (g) Azo-(CH₂)₃-A₁-PEP_{Au}, (h) Azo-(CH₂)₁-A₂-PEP_{Au}, (i) Azo-(CH₂)₂-A₂-PEP_{Au} and (j) Azo-(CH₂)₃-A₂-PEP_{Au}. (k-p) FT-IR and CD spectra of Azo-(CH₂)_m-A_n-PEP_{Au}: (k) and (n), n = 0; (l) and (o), n = 1; (m) and (p), n = 2; green line, m = 1; red line, m = 2; blue line, m = 3.

The family of peptide conjugates were synthesized and purified according to established methods,¹⁰⁷ and their identities were confirmed by mass spectroscopy (see Supporting Information, Figure 2.11 and Figure 2.15 for detail). We first investigated conjugate assembly in 0.1 M HEPES (4-(2-hydroxyethyl)-1-piperazineethanesulfonic acid) aqueous buffer. These conditions were chosen because they are used for the nanoparticle synthesis and assembly experiments. Additional Ca²⁺ ions were added to the assembly solution to promote conjugate assembly.¹⁶⁶ Transmission electron microscopy (TEM) was used to characterize the assemblies (Figure 2.2b-j). Depending on the number of methylene spacers and additional alanine residues in each conjugate, either spherical assemblies or 1-D fibers were observed. More specifically, in terms of number of additional alanine residues, a clear trend of transition from nanospheres to 1-D fibers was observed: for conjugates with no additional alanine, Azo-(CH₂)_m-A₀-PEP_{Au} (m = 1 – 3), only spherical structures were observed (Figure 2.2b-d); when one alanine was added, both spherical and fibrous assemblies were observed (Figure 2.2e-g); however, only 1-D nanofibers were formed for conjugates with two additional alanine residues, Azo-(CH₂)_m-A₂-PEP_{Au} (Figure 2.2h-j). It was observed that the methylene spacer also plays an important role in assembly. For the Azo-(CH₂)_m-A₁-PEP_{Au} subset of conjugates, a structure shift from discrete spheres to 1-D fibers occurs when the number of methylene groups is increased. We concluded from these assembly studies that the propensity for a conjugate to assemble into fibers is determined by both the hydrophobic (organic tail) and hydrophilic (peptide) components. We continued to characterize the conjugate assemblies

with Fourier transform infrared (FT-IR) spectrum and circular dichroism (CD) to gain insight into the molecular interactions underlying the formation of the assemblies. For the spherical structures formed using Azo-(CH₂)₁-A₀-PEP_{Au}, Azo-(CH₂)₂-A₀-PEP_{Au}, Azo-(CH₂)₃-A₀-PEP_{Au}, and Azo-(CH₂)₁-A₁-PEP_{Au}, a broad band around 1650 cm⁻¹ is observed in the FT-IR spectra (Figure 2.2k and l). However, for the rest of the samples, which formed nanofibers, a sharp peak at 1627 cm⁻¹ is observed (Figure 2.2l and m), indicating β -sheet secondary structure. Interestingly, we do not observe the characteristic β -sheet signal in CD spectra for conjugates which assemble into fiber structures. All CD spectra showed a negative maximum at around 205 nm (Figure 2.2n-p), indicating a polyproline II (PPII) structure, which is commonly observed with PEP_{Au} and its derivatives containing proline residues.¹⁶⁷⁻¹⁶⁸ For fiber assemblies, a broad peak at approximately 320 nm associated with the azobenzene group was observed for the nanofibers (Figure 2.2o), indicating that azobenzene is in a chiral environment within the fiber assemblies, whereas no signal is observed in the same region for nanospheres. The observation that different assembled nanostructures exhibit different CD profiles can help us spectroscopically determine the morphology of the peptide conjugate assembly. We concluded from these results that if the hydrophobic segment in the conjugate is too short, the likelihood of forming spherical structures increases due to weaker hydrophobic interactions. Likewise, the additional alanine residues provide additional hydrogen bonding sites between peptide strands, promoting conjugates to pack more closely with one another and helping form nanofibers.

We next examined how these assembled nanospheres and nanofibers responded to UV or visible light irradiation. We hypothesize that due to the geometrical differences between *trans* and *cis* isomers of azobenzene, the bent *cis* isomer would be less favorable for dense conjugate packing. This would lead to a structural disruption for spherical and fibrous assemblies. After

incubating in 0.1 M HEPES buffer for 4 hours, each sample was transferred to a quartz cuvette and irradiated with 355 nm laser for 30 min. TEM studies revealed that conjugates Azo-(CH₂)₁-A₀-PEP_{Au}, Azo-(CH₂)₂-A₀-PEP_{Au}, Azo-(CH₂)₃-A₀-PEP_{Au}, and Azo-(CH₂)₁-A₁-PEP_{Au}, which formed nanospheres before UV-irradiation, disassemble upon UV irradiation, with no obvious assembly observed (Figure 2.3a-d). These samples were next left undisturbed under room light for 18 hours. After visible light treatment, the spherical assemblies reformed (Figure 2.4a-d). For the nanofiber samples, such as those formed from conjugates with two additional alanine residues, UV irradiation does not induce any obvious change in morphology (Figure 2.3f-i and Figure 2.4f-i). Interestingly, however, a transition of sphere→fiber→sphere was observed for Azo-(CH₂)₂-A₁-PEP_{Au}, which has two methylene groups and one alanine residue (Figure 2.3e, Figure 2.4e and Figure 2.5a-c). To confirm this process, CD spectra were recorded (Figure 2.5d). Disappearance of the azobenzene peak at 300 nm clearly indicated the disassembly of nanofibers upon UV irradiation and formation of spherical structures. In addition, through dynamic light scattering (DLS) measurements, we observed a transition from multiple peaks (before irradiation, nanofibers), to single peak (after UV irradiation, 304 nm, nanospheres) and then to multiple peaks (after Vis irradiation, nanofibers, Figure 2.6). From these data, it is clear that the reversibility and the assembly morphologies of the conjugates can be gradually tuned by inserting methylene groups and alanine residues. Evidence from Forood *et al.* showed that alanine residues are important in forming intermolecular hydrogen bonding, thus leading to stronger binding between peptide conjugates.¹⁶⁹

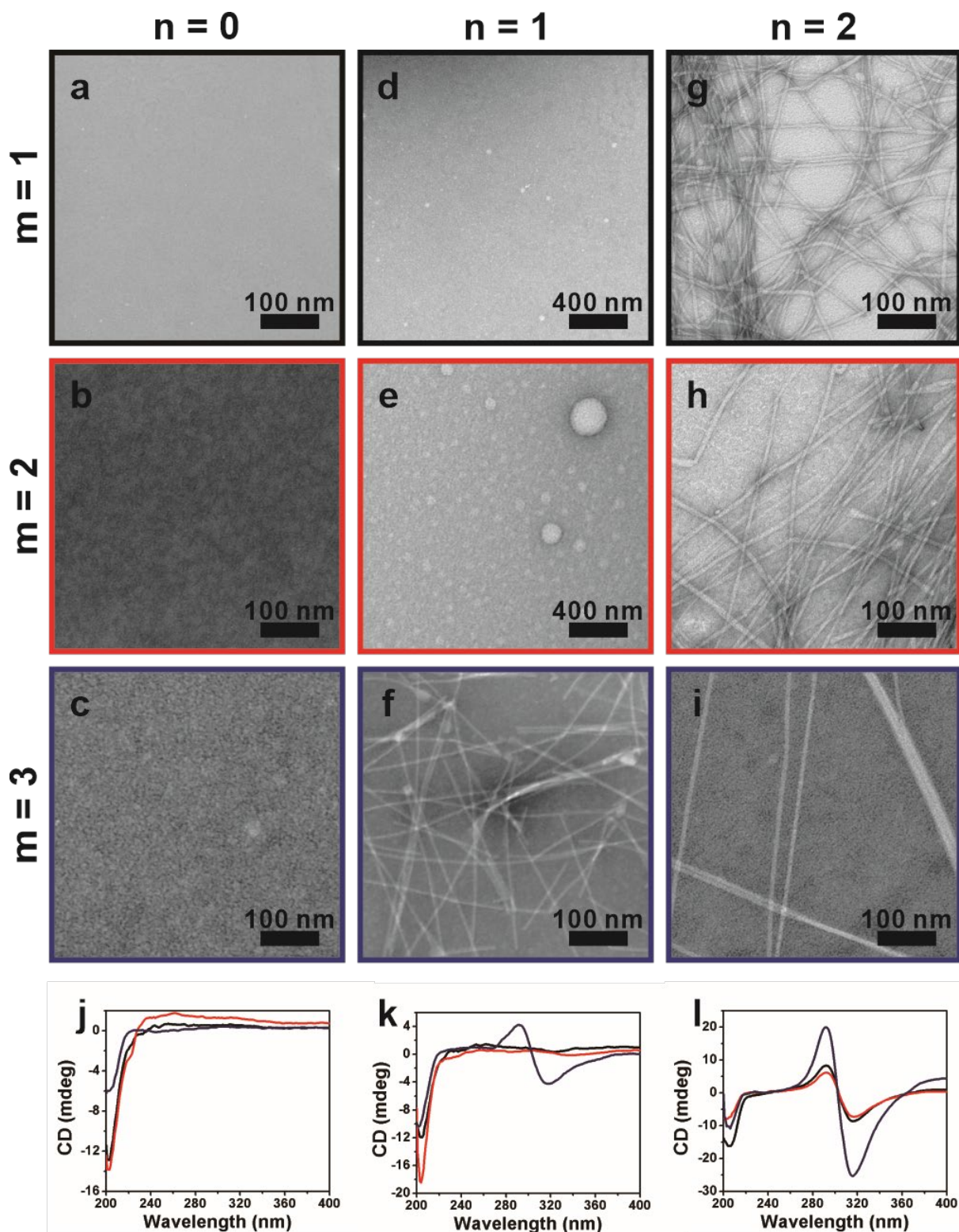


Figure 2.3. TEM images of Azo-(CH₂)_m-An-PEPAu (m = 1-3, n = 0-2) assemblies after UV irradiation for 30 min (a – i), and corresponding CD spectra (j – l). Black: m = 1; red: m = 2; blue: m = 3.

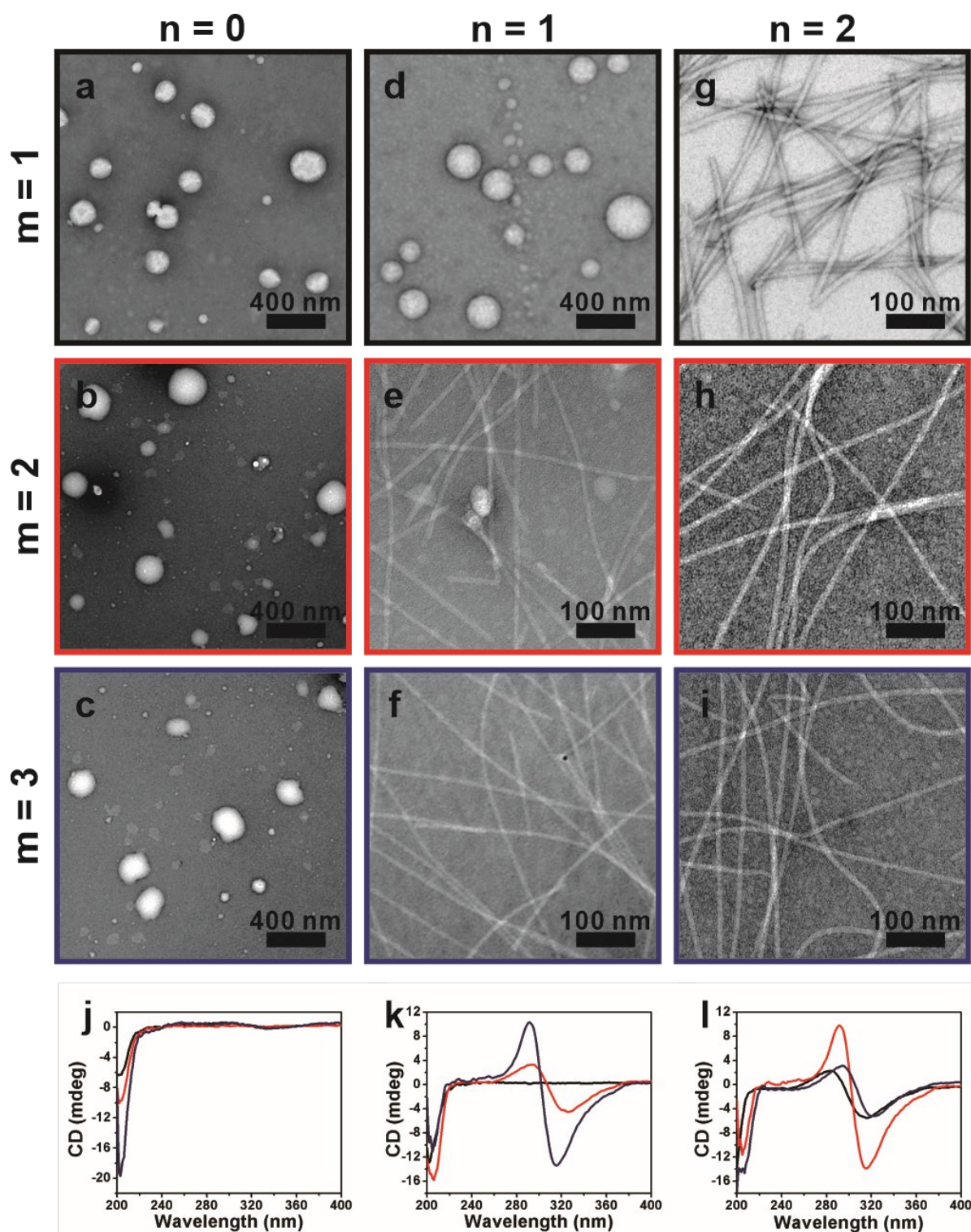


Figure 2.4. TEM images of AzO-(CH₂)_m-An-PEPAu (m = 1-3, n = 0-2) assemblies after visible light irradiation for 18 hrs (a – i), and corresponding CD spectra (j – l). Black: m = 1; red: m = 2; blue: m = 3.

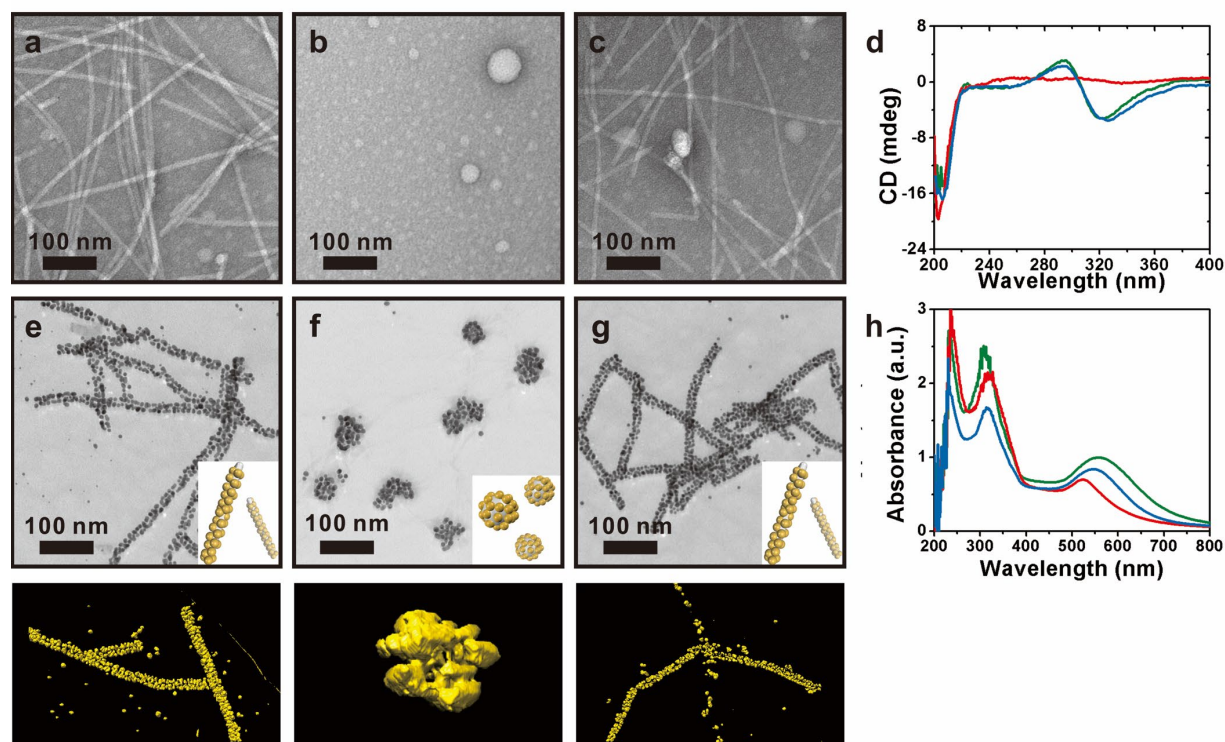


Figure 2.5. UV and visible irradiation of peptide assemblies and NP assemblies formed using Azo-(CH₂)₂-A₁-PEP_{AU}. Top row: peptide assembly before UV irradiation (a), after UV irradiation for 30 min (b) and after visible light irradiation for 18 hrs (c), and corresponding CD signal (d) (Green: before UV irradiation; red: after UV irradiation; blue: after visible light irradiation). Bottom row: NP assembly before UV irradiation (e), after UV irradiation for 30 min (f) and after visible light irradiation for 18 hrs (g), and corresponding UV-Vis spectra (h) (Green: before UV irradiation; red: after UV irradiation; blue: after visible light irradiation).

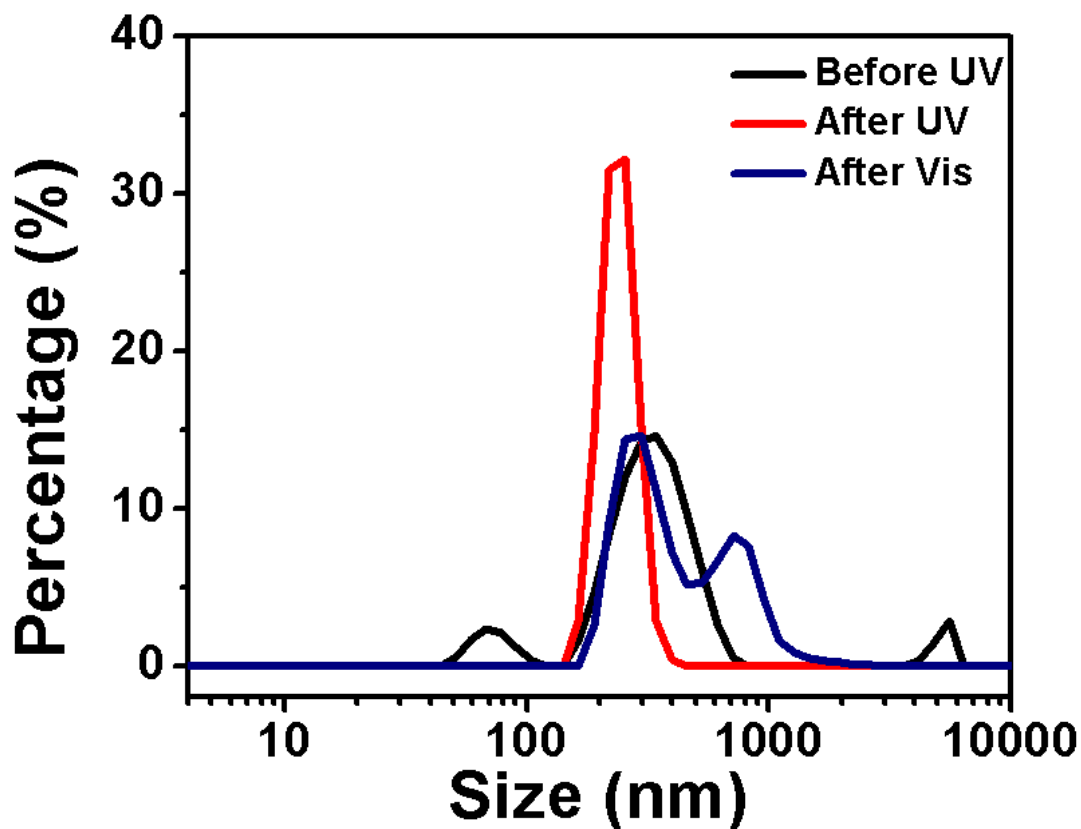


Figure 2.6. Dynamic light scattering results of Azo-(CH₂)₂-A1-PEP_{Au}, assemblies before UV irradiation (black), after UV irradiation for 30 min (red) and after visible light irradiation (blue).

Having explored the peptide conjugate assembly and their responsive behavior to photo-stimulus, we proceeded to prepare nanoparticle assemblies and examine their photo-responsive behavior. The peptide conjugates were dissolved in 0.1 M HEPES buffer, which functions as the primary reducing agent for gold ions and assists in dissolving the conjugates. An aliquot of a solution consisting of HAuCl₄ and triethylammonium acetate (TEAA) buffer was added, and the resulting solution was vortexed and then left undisturbed at room temperature for 4 hours. Because gold ions could also be reduced by UV irradiation,¹⁷⁰ the samples were centrifuged prior to

irradiation to remove excess gold ions. Nanoparticle assemblies were imaged by TEM (Figure 2.5e-g, Figure 2.7, Figure 2.8, and Figure 2.9). The morphology of the nanoparticle assemblies formed from different peptide conjugates corresponds to the morphology of the respective peptide assembly. For Azo-(CH₂)_m-A₀-PEP_{Au} (m = 1 – 3) and Azo-(CH₂)₁-A₁-PEP_{Au}, gold nanoparticles formed pseudo-spherical assemblies and discrete NPs (Figure 2.7), while 1-D nanoparticle superstructures were observed for Azo-(CH₂)₂-A₁-PEP_{Au}, Azo-(CH₂)₃-A₁-PEP_{Au}, Azo-(CH₂)₁-A₂-PEP_{Au}, Azo-(CH₂)₂-A₂-PEP_{Au}, and Azo-(CH₂)₃-A₂-PEP_{Au}. The morphology of the NP assemblies correlates well with the peptide conjugate assemblies.

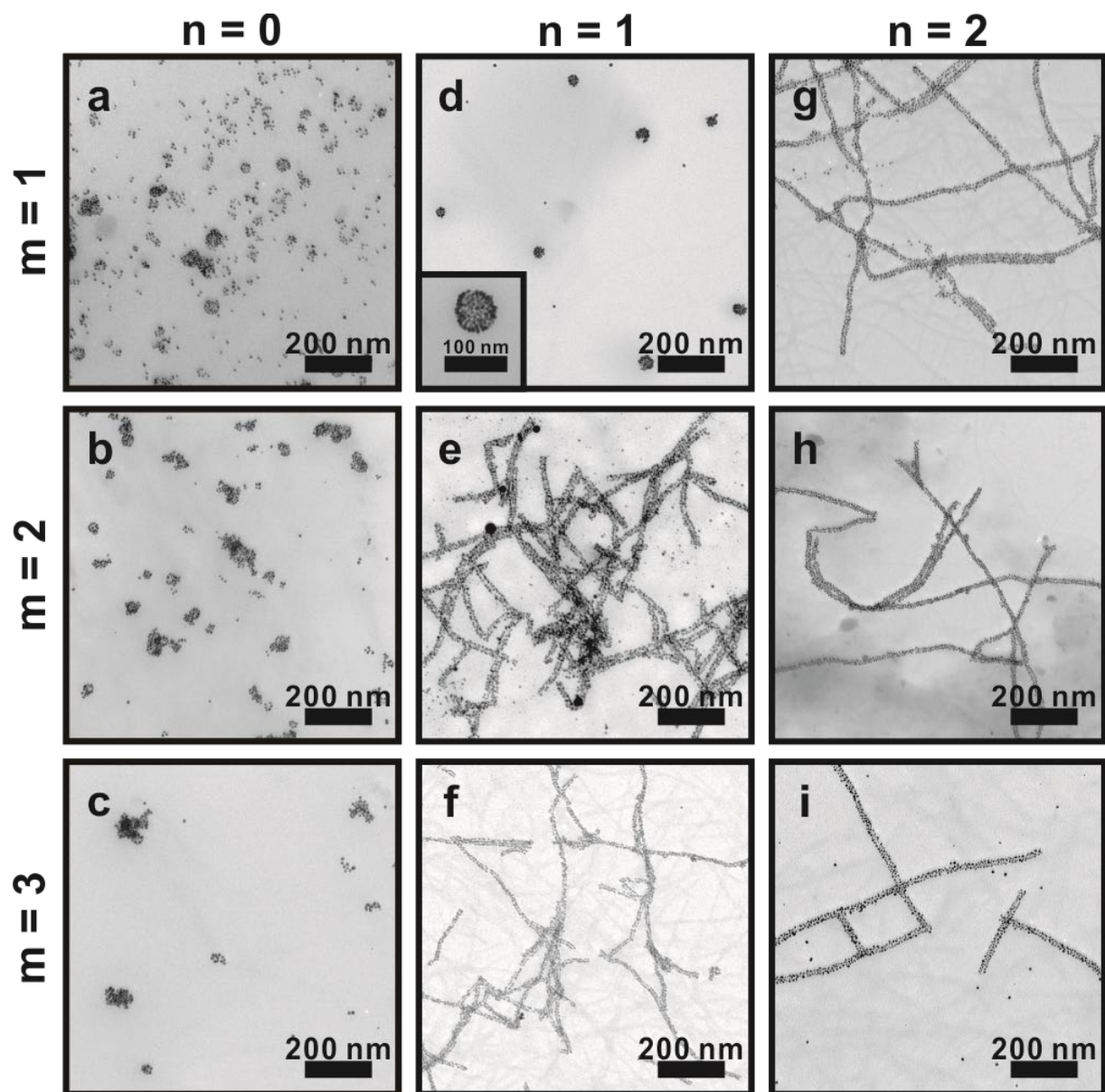


Figure 2.7. TEM images of NP assemblies directed by $\text{Azo}-(\text{CH}_2)_m\text{-A}_n\text{-PEP}_{\text{Au}}$ ($m = 1-3$, $n = 0-2$) before irradiation (a – i).

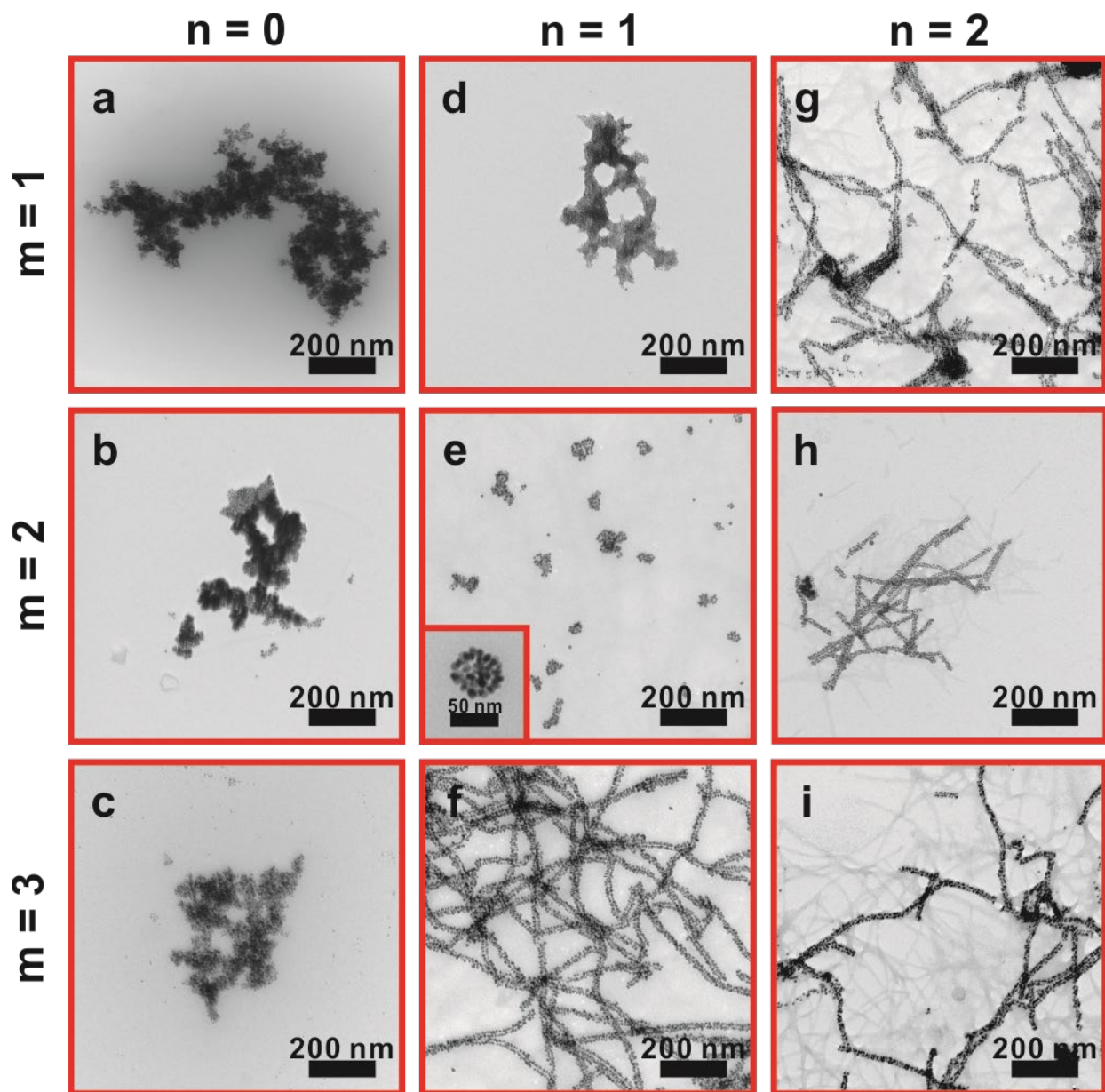


Figure 2.8. TEM images of NP assemblies directed by Azo-(CH₂)_m-A_n-PEP_{Au} ($m = 1-3$, $n = 0-2$) after UV irradiation for 30 min (a – i).

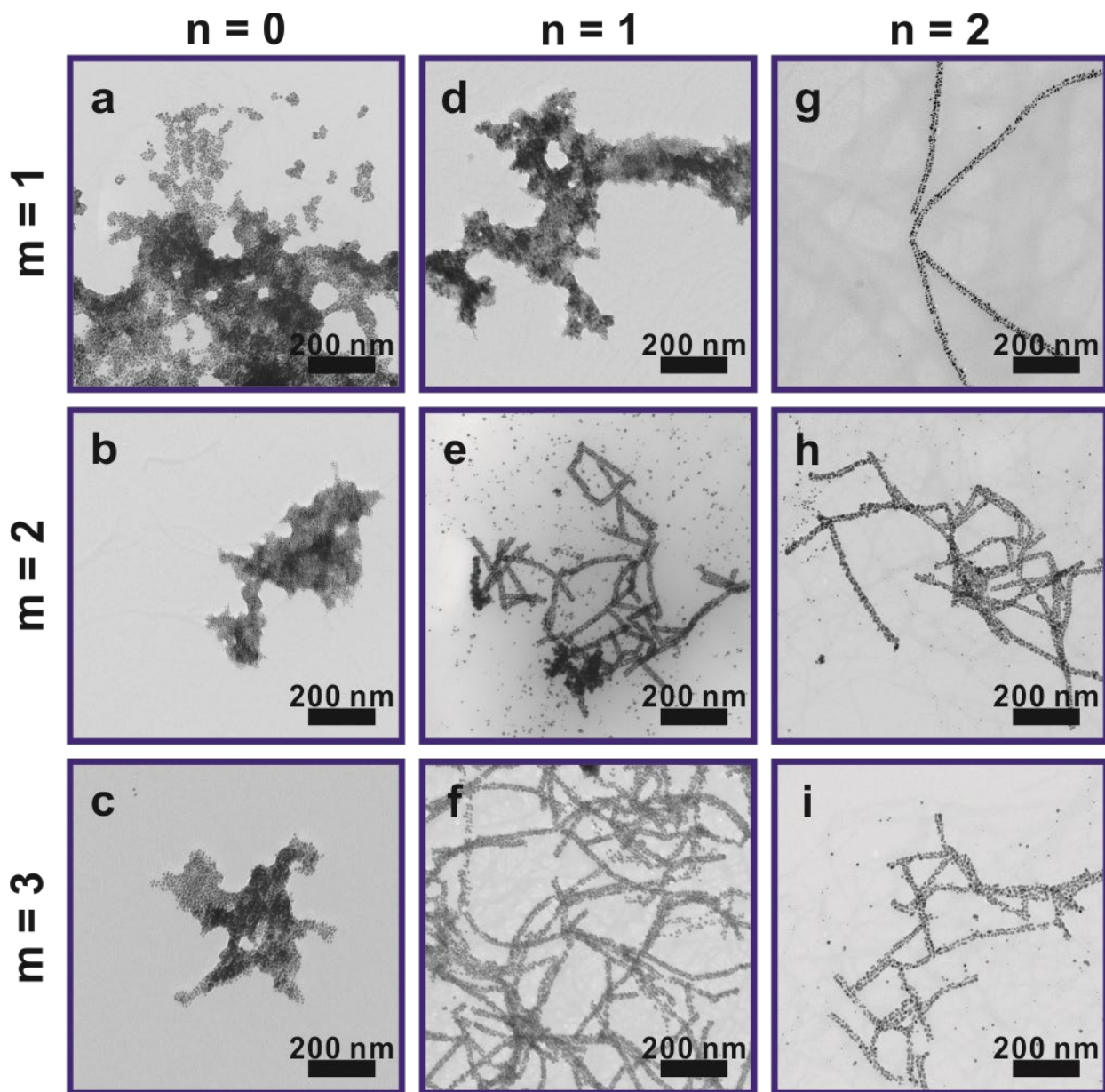


Figure 2.9. TEM images of NP assemblies directed by Azo-(CH₂)_m-A_n-PEP_{Au} (m = 1-3, n = 0-2) after visible light irradiation for 18 hrs (a – i).

We continued to investigate how these assemblies responded to UV and visible light irradiation. After 30 min UV irradiation, spherical assemblies with Azo-(CH₂)_m-A₀-PEP_{Au} (m = 1 – 3) and Azo-(CH₂)₁-A₁-PEP_{Au} disassembled and formed either discrete nanoparticles or irregular aggregates (Figure 2.8 **Error! Reference source not found.**a-d). When these samples were further

treated with visible light, no obvious further changes could be observed via TEM (Figure 2.9a-d). From peptide assembly, we know that nanospheres disassemble and recover upon UV and visible light treatment, respectively (Figure 2.3a-d). However, the nanoparticle assembly does not reassemble.

Irradiation of 1-D nanoparticle superstructures yielded similar results to those of peptide assembly. Upon 30 min UV irradiation, TEM images showed that no obvious changes occurred to assemblies produced using Azo-(CH₂)₃-A₁-PEP_{Au}, Azo-(CH₂)₁-A₂-PEP_{Au}, Azo-(CH₂)₂-A₂-PEP_{Au}, and Azo-(CH₂)₃-A₂-PEP_{Au}; that is, the 1-D assembly remained mostly intact upon UV treatment (Figure 2.8f-i). Subsequently, no further changes could be recorded upon visible light irradiation (Figure 2.9f-i). Even when the superstructures are irradiated with UV for up to 4 hours, no obvious changes can be observed. The nanoparticle assembly results correspond well to the peptide assembly data, indicating that strong intermolecular interactions between the peptide conjugates within the structure.

Among this family of conjugates, Azo-(CH₂)₂-A₁-PEP_{Au} remains the most unique conjugate in terms of its reversible photoresponsive behavior. After 30 min of UV irradiation, the 1-D nanoparticle superstructures formed using Azo-(CH₂)₂-A₁-PEP_{Au} were no longer observable; instead, spherical assemblies and discrete nanoparticles were the major products (Figure 2.5f). After subsequent irradiation under visible light for 18 hours, the 1-D nanoparticle superstructures could be observed again (Figure 2.5g). To better understand the process, we first monitored the process with extinction spectra (Figure 2.5h). Upon UV irradiation, the plasmon band of assembled 1-D superstructures blue-shifted from 557 nm to 525 nm. After visible light irradiation, a red-shift from 525 nm to 545 nm was observed. The extinction spectra could be correlated to the transformation between 1-D and spherical nanoparticle superstructures. We prepared an analogous

biphenyl-based peptide conjugate and compared its behavior to Azo-(CH₂)₂-A₁-PEP_{Au}. BP-AA-PEP_{Au} also assembles into nanofibers and also directs the formation of 1-D nanoparticle superstructures. When these assemblies and superstructures were irradiated with UV or visible light, no morphological changes were observed for either the peptide conjugate assembly or the NP superstructure (Figure 2.18).

In addition, we measured the individual nanoparticle sizes in each stage of the process, and the data indicated the particle sizes remained unchanged, from 6.9 ± 0.9 nm to 7.2 ± 1.3 nm and then to 7.9 ± 1.6 nm before irradiation and upon UV and visible irradiation respectively (Figure 2.19). In addition, no nanoprisms or large (diameter > 20 nm) particles were present, which are the main products from gold ions reduced directly by UV irradiation¹⁷⁰ (Figure 2.20). This suggested that no additional (at least observable) nanoparticles were formed upon UV irradiation. Furthermore, to rule out the possibility that the change in morphology was not induced by the heat from laser irradiation, we monitored the temperature change for each sample during UV irradiation. The temperature of each sample increased from 2 to 4 °C after irradiation (see Table 2.2). While these samples were incubated at elevated temperature, no obvious change can be identified. This indicated that morphological shifts were not caused by temperature variation.

We next examined the NP superstructures formed using Azo-(CH₂)₂-A₁-PEP_{Au} in more detail. In order to gain insight into the structure transition process, TEM images at different stages of transformation were recorded (Figure 2.10). The 1-D superstructures (Figure 2.10a) was irradiated with UV light for 5 min (Figure 2.10b), 10 min (Figure 2.10c), 15 min (Figure 2.10d) and 30 min (Figure 2.10e), resulting ultimately in a final spherical morphology. During this process, linear structures disassembled and spherical structure gradually formed at the same time. For the reverse process (visible light irradiation), spherical assemblies gradually disassembled and

linear assemblies were recovered following visible irradiation for 2 hrs (Figure 2.10f), 4 hrs (Figure 2.10g), 6 hrs (Figure 2.10h), 8 hrs (Figure 2.10i) and 12 hrs (Figure 2.10j). The TEM studies indicated that the morphology transformation is a gradual transition between 1-D and spherical superstructures.

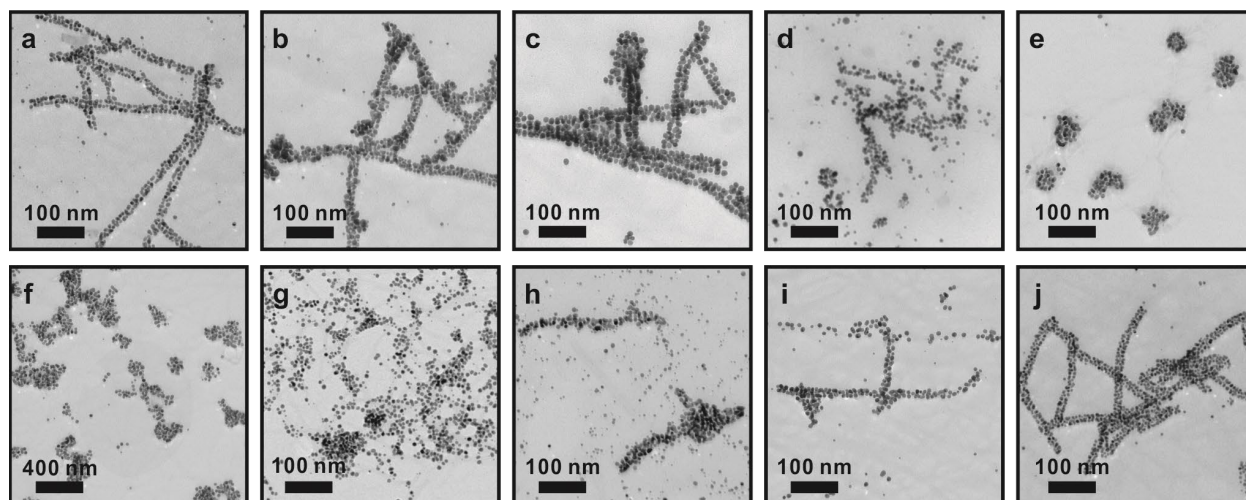


Figure 2.10. UV and visible light irradiation on Azo-(CH₂)₂-A₁-PEP_{Au} directed assemblies as a function of time. Top row: UV irradiation of Azo-(CH₂)₂-A₁-PEP_{Au} directed assemblies for (a) 0 min, (b) 5 min, (c) 10 min, (d) 15 min and (e) 30 min. Bottom row: visible light irradiation of Azo-(CH₂)₂-A₁-PEP_{Au} directed assemblies for (f) 2 h, (g) 4 h, (h) 6 h, (i) 8 h and (j) 12 h.

2.3 Conclusion

In summary, we designed and synthesized a family of photo-responsive peptide conjugates, Azo-(CH₂)_m-A_n-PEP_{Au} (m = 1-3, n = 0-2), with modulated response to photo stimulus based on the number of additional methylene groups and additional alanine residues between the photoresponsive azobenzene moiety and the gold binding peptide sequence. Both hydrophobic interactions (affected by the number of additional methylene groups) and hydrogen bonding

interactions (affected by the number of additional alanine residues) play key roles in 1) controlling the morphology of peptide and Au NP assemblies, and 2) governing the photo responses of peptide assemblies and Au NP assemblies. Reversible, gradual transition between 1-D and spherical structures were observed for peptide assemblies and Au NP assemblies directed by conjugate Azo-(CH₂)₂-A₁-PEP_{Au}, which has moderate hydrophobic and hydrogen bonding interactions. We envision that this photo-reversible peptide method may lead to new strategies for designing and developing novel stimuli-active nanomaterials with switchable optical, electrical, and catalytic properties.

2.4 Supplementary Information

2.4.1 General Information

All chemicals were purchased from Sigma-Aldrich and used without any further purification unless otherwise specified. Peptide conjugate were synthesized using typical solid-state peptide synthesis. ¹H-NMR spectra were recorded on a Bruker DRX 300 spectrometer. Chemical shifts were recorded in ppm (parts per million) based on residual solvent peaks as internal reference (d₆-DMSO δ: 2.54 (¹H)). Reverse-phase high pressure liquid chromatography (RP-HPLC) was performed at ambient temperature with an Agilent 1200 liquid chromatographic system equipped with an Agilent Zorbax 300SB-C₁₈ column. Matrix-assisted laser desorption ionization time-of-flight (MALDI-TOF) mass spectra were obtained on a Bruker ultrafleXtreme™ MALDI-TOF/TOF mass spectrometer (Grant from National Science Foundation CHE-1625002) using α-cyano-4-hydroxy cinnamic acid (CHCA) as the ionizing matrix. Transmission

election microscopy (TEM) samples were prepared by pipetting 5 μL of solution onto a 3-mm-diameter copper grid with carbon film; 2% aqueous uranyl acetate solution (pH adjusted to 7.0 by adding 0.1 M NaOH) was used for negative staining. TEM was conducted on a FEI Morgagni 268 operated at 80 kV and equipped with an AMT side mount CCD camera system. UV-vis spectra were collected using an Agilent 8453 UV-Vis Spectrometer with a quartz cuvette (10 mm path length) at room temperature. Attenuated total reflectance Fourier transform infrared spectra (ATR-FTIR) were collected on a PerkinElmer Spectrum 100 FTIR instrument with a universal attenuated total reflectance sampling accessory coupled to a computer using PerkinElmer Spectrum Express software. The sample was back-corrected in air. Peptide conjugate was dissolved and sonicated in 0.1 M HEPES buffer (100 μM). After 1 day, the assembled spheres or fibers were dialyzed against NP H₂O using D-Tube Dialyzer Midi (Millipore Novagen, MWCO 3.5 kDa) to remove the buffer, and the spheres or fibers were concentrated. The concentrated solution was then drop-cast onto the ATR-FTIR substrate and allowed to air-dry. Circular dichroism spectra were collected using an Olis DSM 17 CD spectrometer. The scan rate was 8 nm/min with a bandwidth of 2 nm. All CD measurements were carried out in 10 mM HEPES (peptide assembly) or 0.1 M HEPES (nanoparticle assembly) with a 1 mm path length quartz cuvette at 20 °C. UV irradiation was conducted on a laser with wavelength of 355 nm. Either peptide assembly samples or NP assembly samples was transferred to a quartz cuvette with 1 cm path length, and irradiated with laser for certain amount of time. 0.1 M HEPES (4-(2-hydroxyethyl)-piperazinethanesulfonic acid) buffer was prepared by directly diluting 1.0 M HEPES buffer (pH = 7.3 \pm 0.1, Fisher Scientific) with water (NANOpure, Barnstead DiamondTM System, 18.2 M Ω).

2.4.2 Syntheses of Azo-(CH₂)_m-A_n-PEP_{Au} (m = 1-3, n = 0-2)

2.4.2.1 Synthesis of Azobenzene Carboxylic Acids

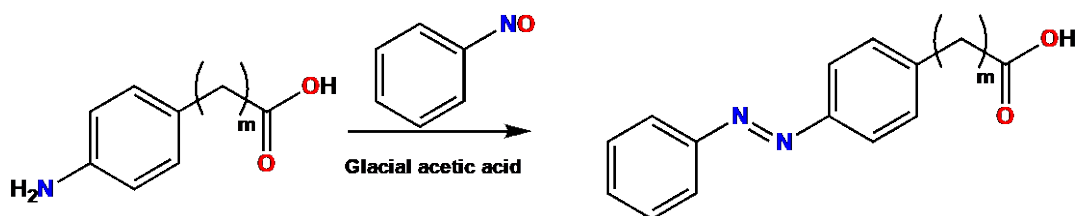
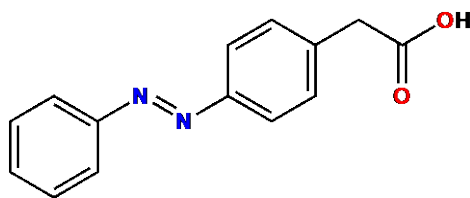


Figure 2.11. Schematic for synthesis of azobenzene carboxylic acids.

All azobenzene carboxylic acids were synthesized using reported method.¹⁷¹

2.4.2.1.1 2-(4-(Phenyldiazenyl)phenyl)acetic Acid (MW = 240.15 g/mol)



2-(4-aminophenyl)acetic acid (3 mmol, 455.1 mg) was dissolved in 5 mL warm glacial acetic acid. Then the mixture was cooled to room temperature. To the cooled solution, nitrosobenzene (3 mmol, 321.3 mg) was added and the reaction vial was vortexed to yield a dark orange solution. The mixture was left undisturbed for 12 hours, during which time orange crystals were precipitated. The orange crystal was filtered, washed by water and recrystallized in ethanol. Yield = 47%. ¹H-NMR spectrum of the product is shown in Figure 2.12, using d₆-DMSO (δ: 2.54 (¹H)) as solvent.

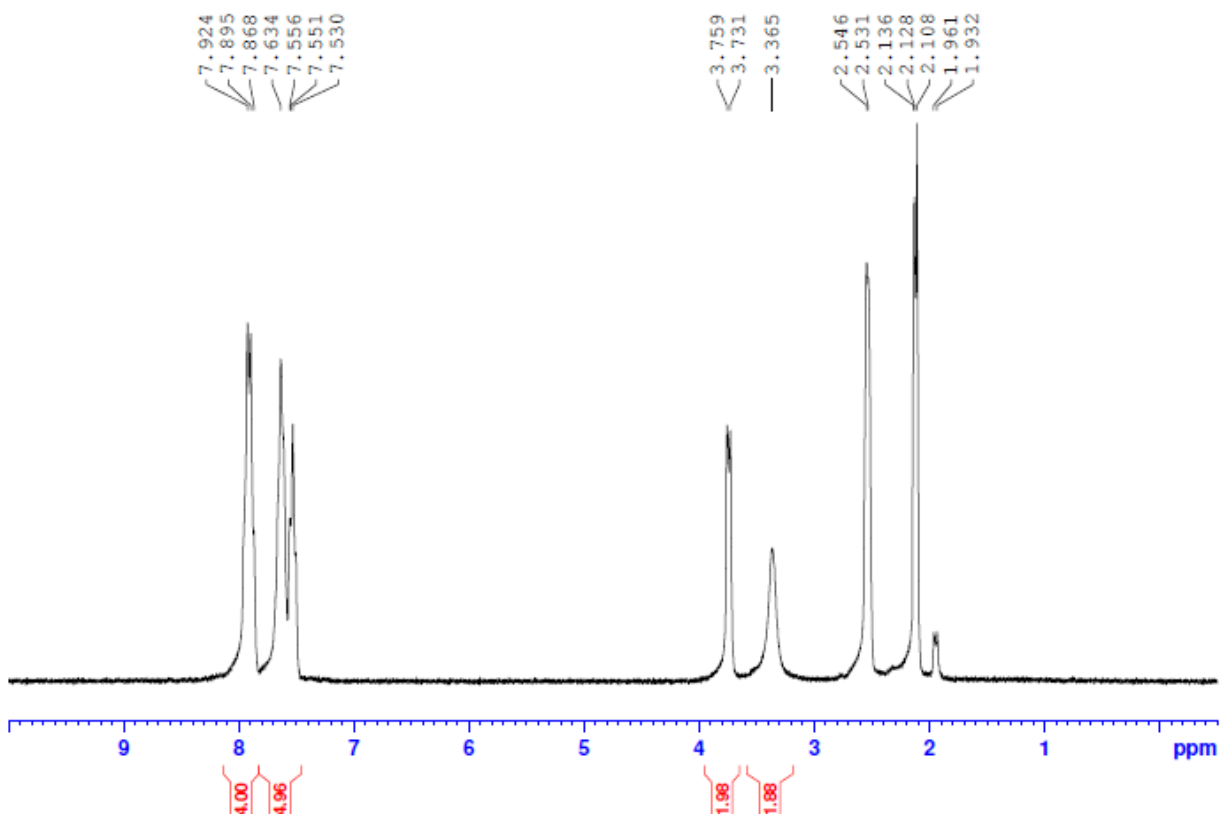
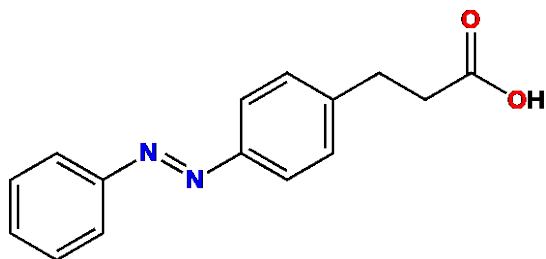


Figure 2.12. $^1\text{H-NMR}$ spectrum of 2-(4-aminophenyl)acetic acid.

2.4.2.1.2 3-(4-(Phenyldiazenyl)phenyl)propanoic Acid (MW = 254.29 g/mol)



3-(4-aminophenyl)propanoic acid (3 mmol, 495.6 mg) was dissolved in 5 mL warm glacial acetic acid. Then the mixture was cooled to room temperature. To the cooled solution, nitrosobenzene (3 mmol, 321.3 mg) was added and the reaction vial was vortexed to yield a dark

orange solution. The mixture was left undisturbed for 12 hours, during which time orange crystals were precipitated. The orange crystal was filtered, washed by water and recrystallized in ethanol. Yield = 66%. $^1\text{H-NMR}$ spectrum of the product is shown in Figure 2.13, using $\text{d}_6\text{-DMSO}$ (δ : 2.54 (^1H)) as solvent.

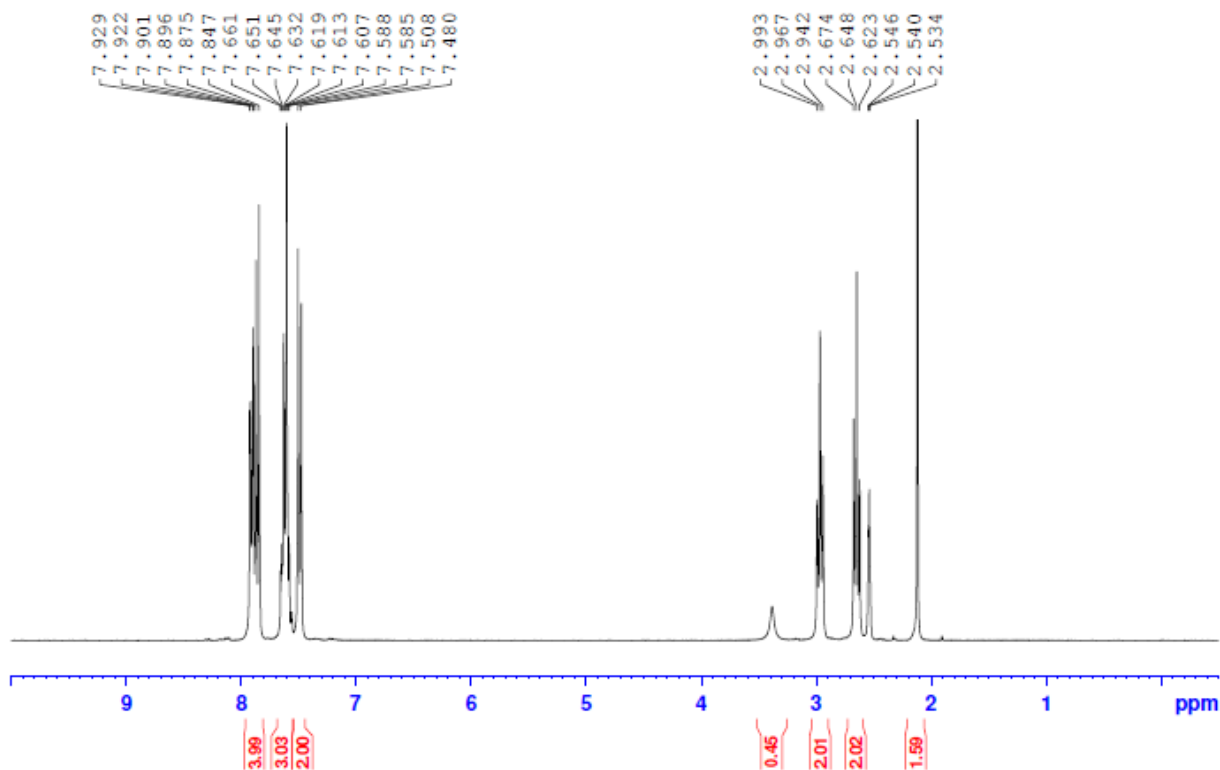
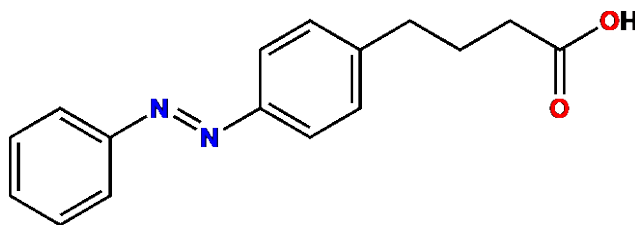


Figure 2.13. $^1\text{H-NMR}$ spectrum of 3-(4-aminophenyl)propanoic acid.

2.4.2.1.3 4-(4-(Phenyldiazenyl)phenyl)butanoic Acid (MW = 268.32 g/mol)



4-(4-Aminophenyl)butanoic acid (1.5 mmol, 268.83 mg) was dissolved in 5 mL warm glacial acetic acid. Then the mixture was cooled to room temperature. To the cooled solution, nitrosobenzene (1.5 mmol, 160.7 mg) was added and the reaction vial was vortexed to yield a dark orange solution. After it was then left undisturbed for 12 hours, 5 mL water was added to precipitate an orange crude product (370 mg, 1.37 mmol, yield = 91.9%). The solid was re-dissolved in warm ethanol, cooled to room temperature, and re-precipitated with water. The solid was then filtered, oven-dried, and dried *in vacuo* (1.34 mmol, yield = 89.4%). ¹H-NMR spectrum of the product is shown in Figure 2.14, using d₆-DMSO (δ: 2.54 (¹H)) as solvent.

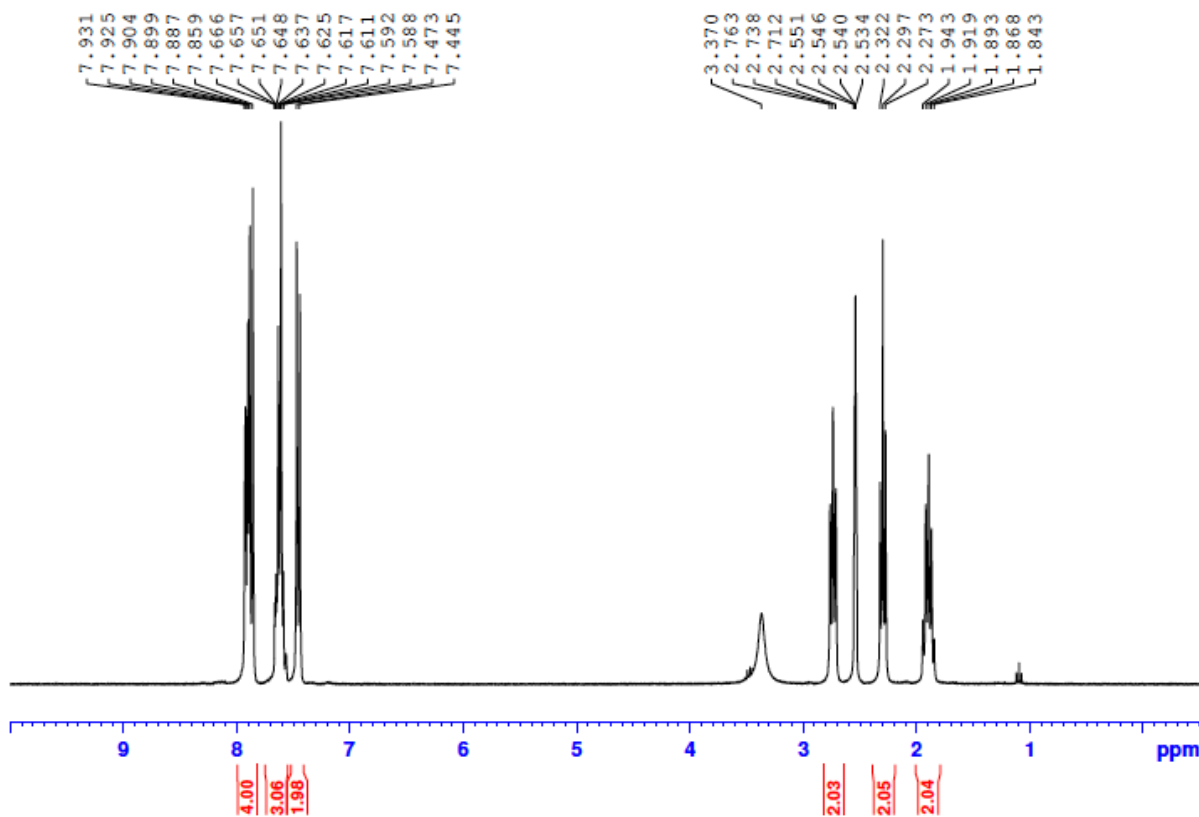


Figure 2.14. ¹H-NMR spectrum of 4-(4-Aminophenyl)butanoic acid.

2.4.2.2 Syntheses of Peptide Conjugates Azo-(CH₂)_m-A_n-PEP_{Au} (m = 1-3, n = 0-2)

2.4.2.2.1 General Information

All reagents were purchased from Sigma-Aldrich unless specified otherwise. All Fmoc-protected amino acids and Fmoc-protected resin were purchased from Novabiochem. *O*-(1H-6-Chlorobenzotriazole-1-yl)-1,1,3,3-tetramethyluronium hexafluorophosphate (HCTU) was purchased from Oakwood Chemical. Formic acid was purchased from J.T. Baker.

2.4.2.2.2 Peptide Synthesis and Purification

All peptide conjugates were synthesized by manual microwave-assisted Fmoc solid phase methods using a CEM MARS microwave and NovaSyn TGA resin. Typical coupling reactions were performed with a 1 min ramp from room temperature to 75 °C followed by a 5 min hold at 75 °C, and Fmoc deprotections performed with a 1 min ramp to 75 °C followed by a 2 min hold at that temperature.

Coupling solutions were composed of Fmoc-protected amino acid (5 equiv relative to resin), HCTU (5 equiv), and DIEA (7 equiv) in 1-methyl-2-pyrrolidinone (NMP). Fmoc deprotections used 20% v/v 4-methylpiperidine in DMF. The resin was washed three times with DMF between each reaction. After the last Fmoc-Ala was coupled and deprotected, corresponding azobenzene carboxylic acid (5 equiv) was activated and coupled following the same procedure described above.

After coupling, the resin was washed three times each with DMF, dichloromethane (DCM) and methanol, and then air-dried. Peptides were cleaved from resin by treatment with TFA and

scavengers for 3.5 hours. Specific cleavage solution was as follows: TFA/H₂O/EDT/TIS (92.5/3/3/1.5 by volume, 2 mL in total volume). (TFA: trifluoroacetic acid. EDT: 1,2-ethanedithiol. TIS: triisopropylsilane.) After filtration, crude peptide in TFA was precipitated in 10 mL cold Et₂O. It was then centrifuged and washed with cold Et₂O for three times. The pellet was then dissolved in 10 mL ACN/H₂O (1/1 by volume) and kept at 4 °C until purification.

Peptides were purified via reverse phase HPLC (RP-HPLC) on a C18 column using gradients between 0.1% TFA in water and 0.05% TFA in acetonitrile (95/5 to 5/95 over 30 min). The identity was confirmed on a Bruker Ultraflex extreme MALDI-TOF mass spectrometer (National Science Foundation, CHE-1625002) with CHCA as ionizing matrix.

2.4.3 Supporting Figures and Tables

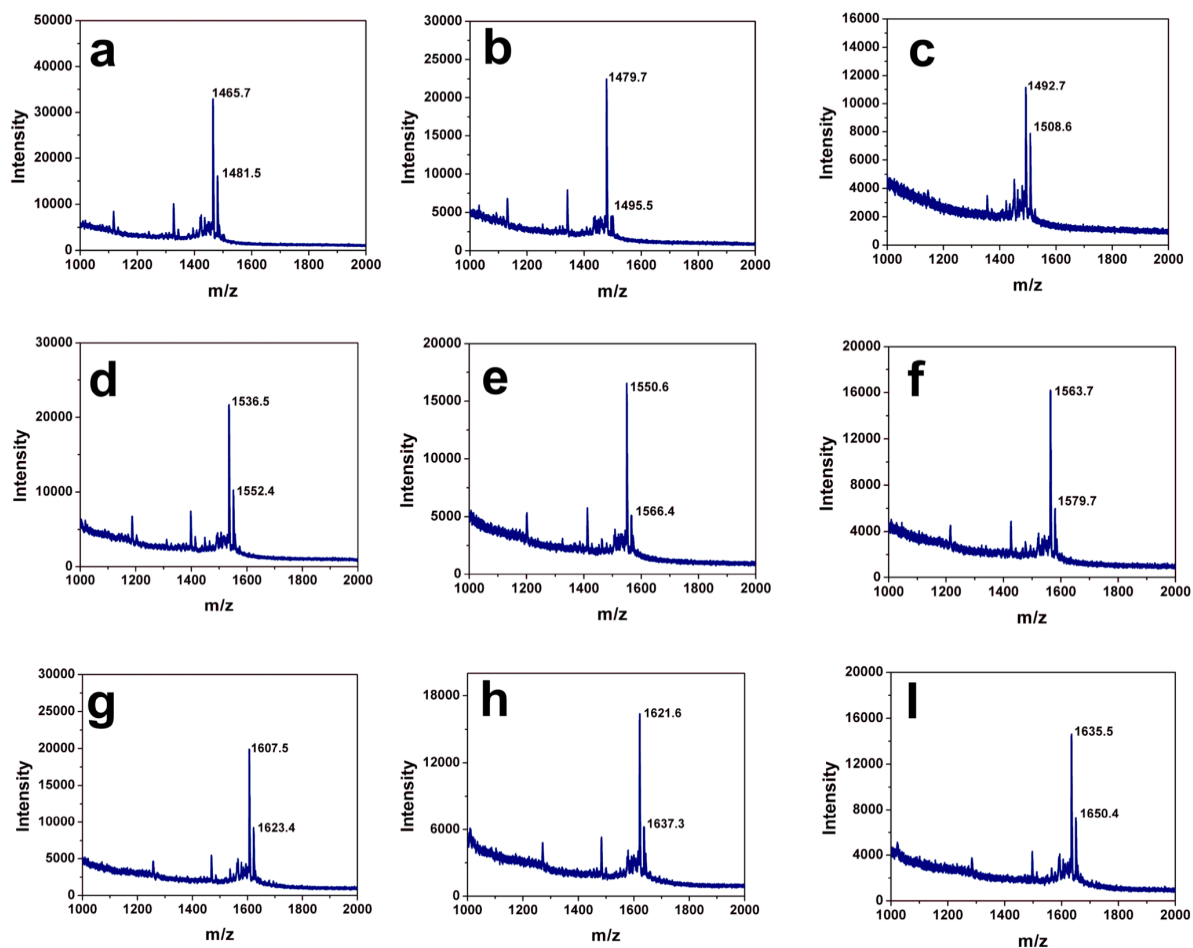


Figure 2.15. MALDI-TOF spectra of Azo-(CH₂)_m-A_n-PEP_{Au} (m = 1-3, n = 0-2). (a)-(c) m = 1-3, n = 0; (d)-(f) m = 1-3, n = 1, (g)-(i) m = 1-3, n = 2.

Table 2.1. Molar masses of conjugates Azo-(CH₂)_m-A_n-PEP_{Au}

Azo-(CH ₂) _m -A _n -PEP _{Au}	m = 1	m = 2	m = 3
n = 0	1442.6	1456.6	1470.6
n = 1	1513.7	1527.7	1541.7
n = 2	1584.7	1598.7	1612.7

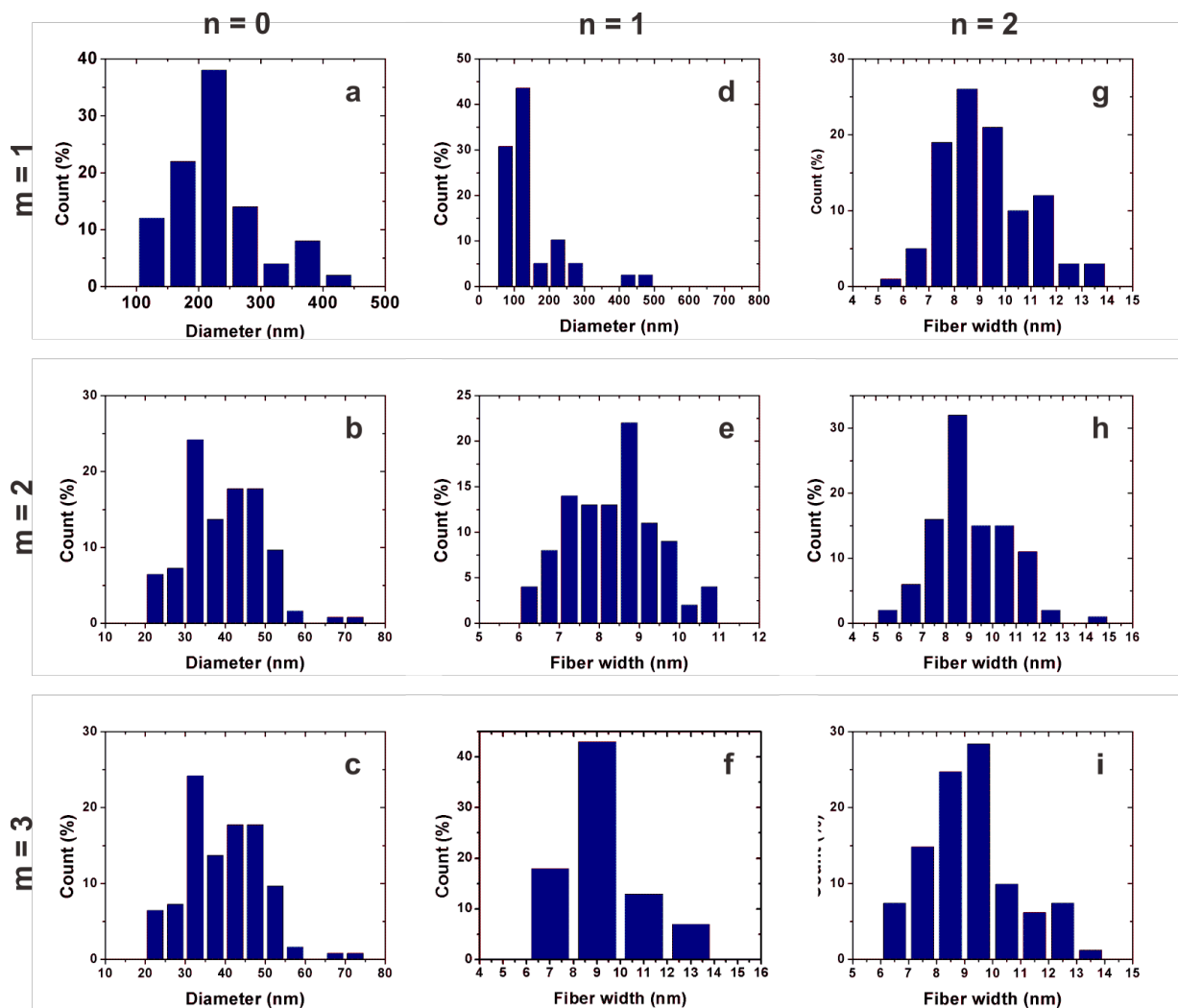


Figure 2.16. Metrics of peptide assemblies formed using $\text{Azo}-(\text{CH}_2)_m\text{-A}_n\text{-PEP}_{\text{Au}}$. For spherical peptide assemblies (a) $\text{Azo}-(\text{CH}_2)_1\text{-A}_0\text{-PEP}_{\text{Au}}$, (b) $\text{Azo}-(\text{CH}_2)_2\text{-A}_0\text{-PEP}_{\text{Au}}$, (c) $\text{Azo}-(\text{CH}_2)_3\text{-A}_0\text{-PEP}_{\text{Au}}$, and (d) $\text{Azo}-(\text{CH}_2)_2\text{-A}_1\text{-PEP}_{\text{Au}}$, diameters are measured based on at least 100 counts. For fiber assemblies (e) $\text{Azo}-(\text{CH}_2)_2\text{-A}_1\text{-PEP}_{\text{Au}}$, (f) $\text{Azo}-(\text{CH}_2)_3\text{-A}_1\text{-PEP}_{\text{Au}}$, (g) $\text{Azo}-(\text{CH}_2)_1\text{-A}_2\text{-PEP}_{\text{Au}}$, (h) $\text{Azo}-(\text{CH}_2)_2\text{-A}_2\text{-PEP}_{\text{Au}}$, and (i) $\text{Azo}-(\text{CH}_2)_3\text{-A}_2\text{-PEP}_{\text{Au}}$, widths of fibers are measured based on at least 100 counts.

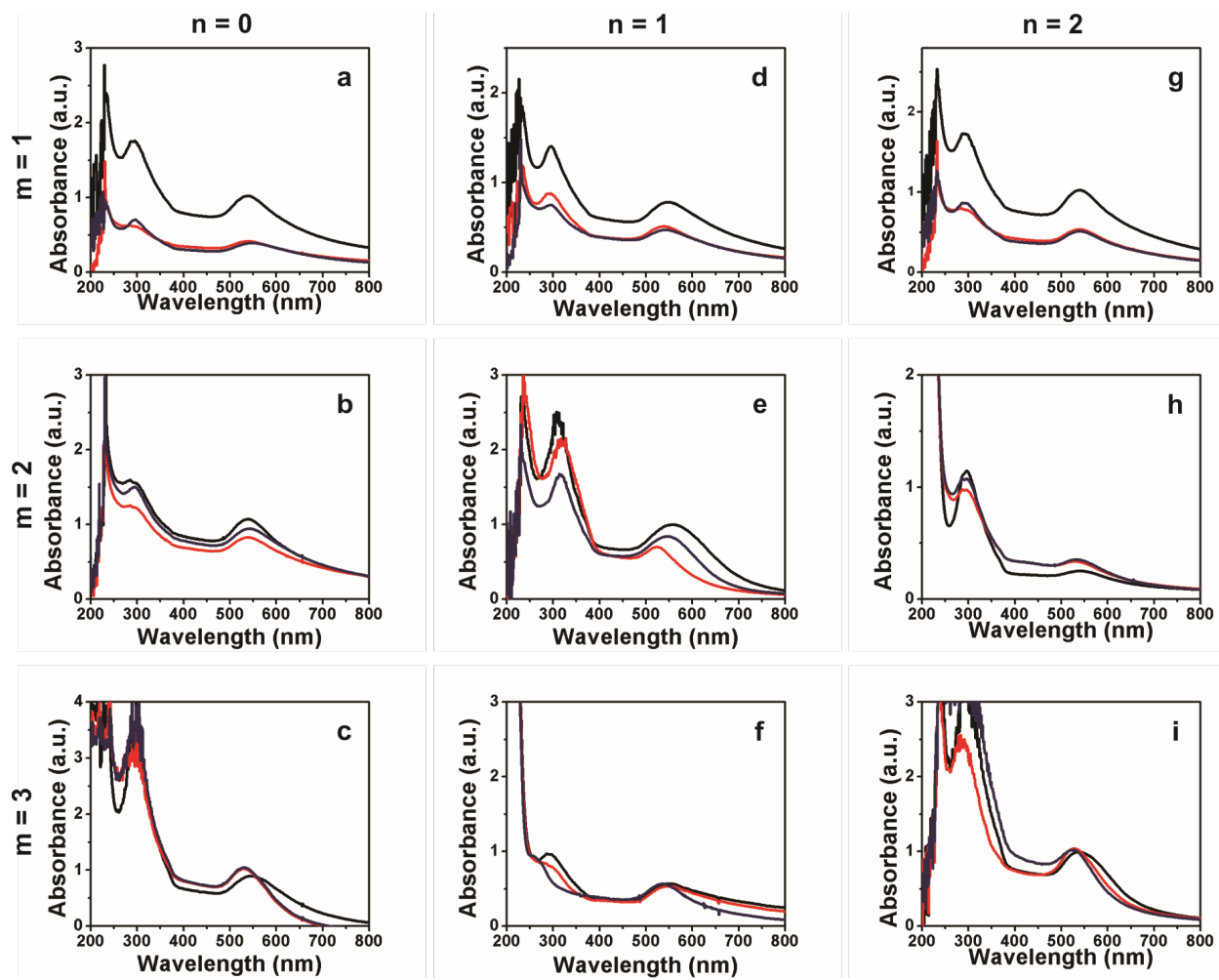


Figure 2.17. UV-Vis spectra of NP assemblies formed using Azo-(CH₂)_m-A_n-PEP_{Au} ($m = 1-3$, $n = 0$) before irradiation (black), after UV irradiation (red) and after visible light irradiation (blue).

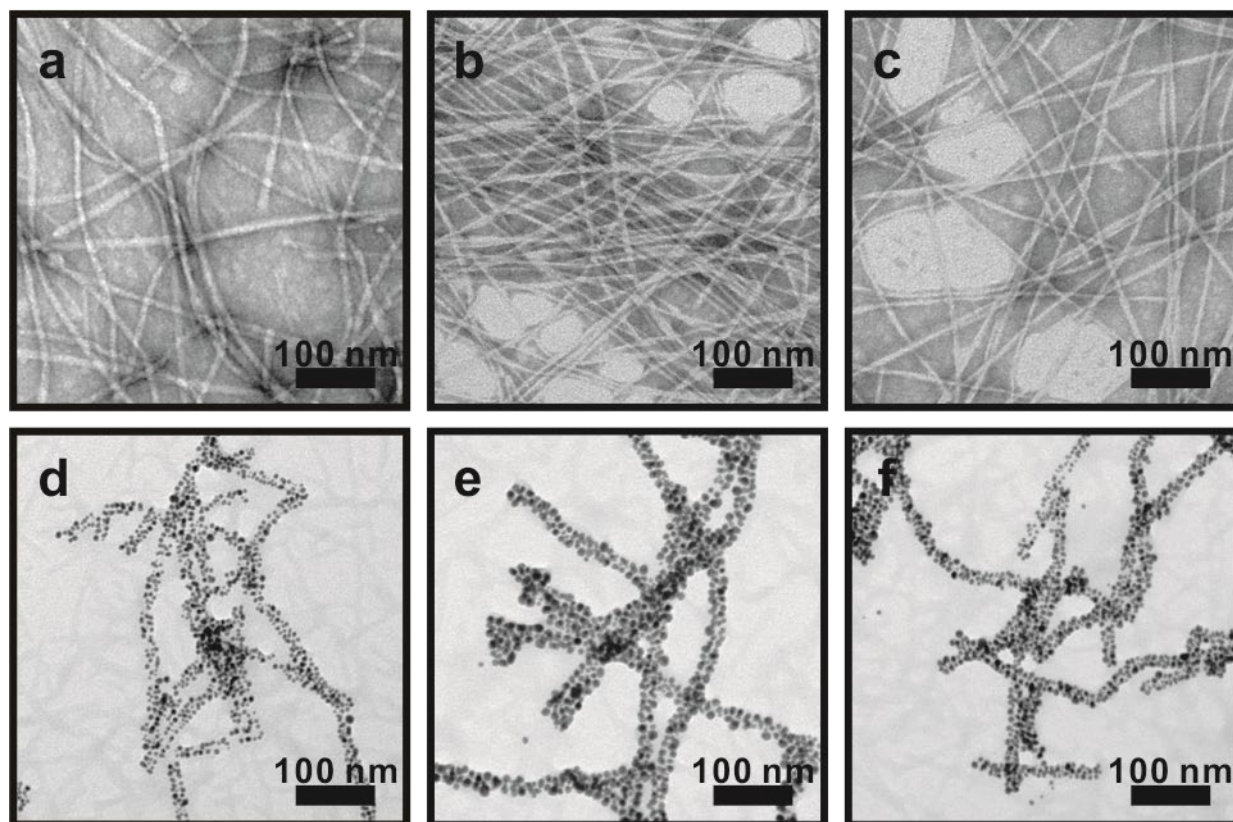


Figure 2.18. TEM images of peptide (a-c) and AuNP assembly (d-f) upon UV and visible light irradiation directed by conjugate BP-AA-PEP_{Au} (BP = biphenyl). (a) and (d): before UV irradiation; (b) and (e) after UV irradiation for 30 min; (c) and (f) after visible light irradiation for 18 hrs.

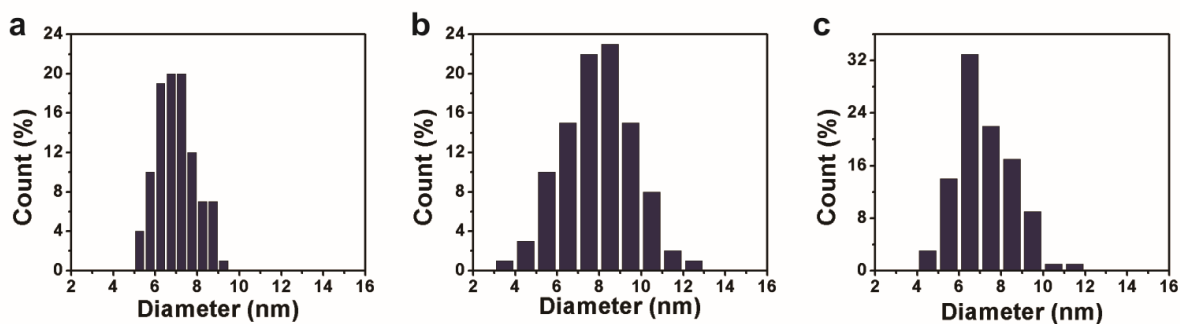


Figure 2.19. NP size measurement in assemblies formed using Azo-(CH₂)₂-A₁-PEP_{Au} before UV irradiation (a), after UV irradiation for 30 min (b) and after visible light irradiation for 18 hrs (c).

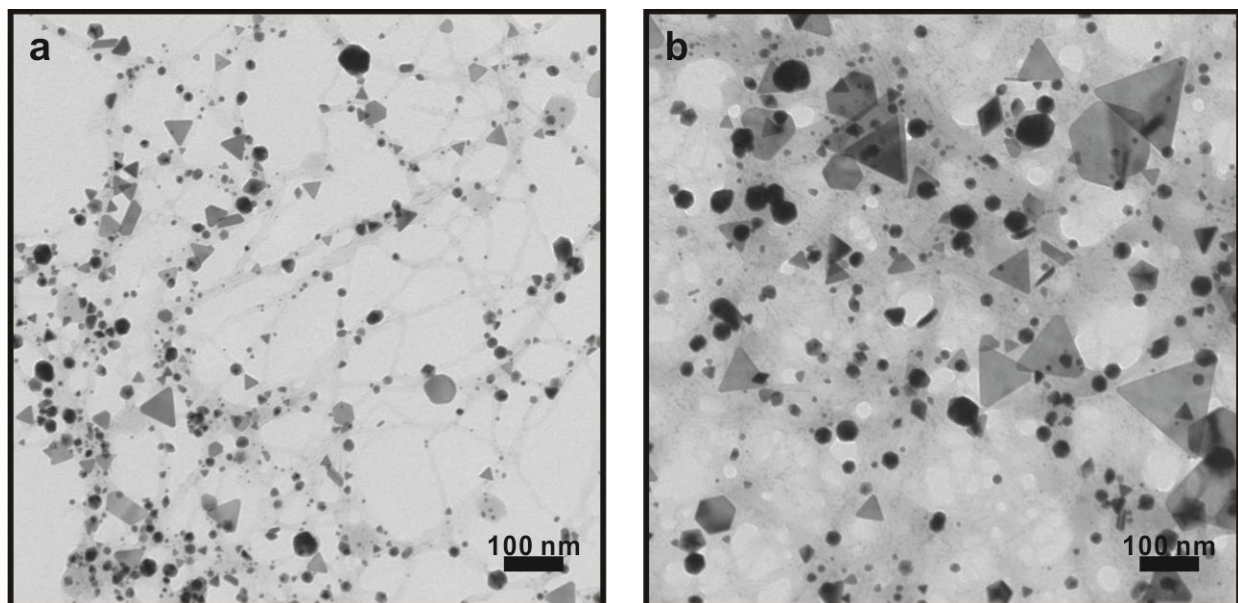


Figure 2.20. TEM images of a sample without addition of any peptide conjugates irradiated by UV light for 30 min.

Table 2.2. Temperature change of AuNP assemblies in HEPES buffer upon UV irradiation for 30 min and 1 hr.

Conjugates	Before irradiation	After UV Irradiation (30 min)	After UV Irradiation (1 h)
Azo-(CH ₂) ₁ -A ₁ -PEP _{Au}	22.16	24.85	25.33
Azo-(CH ₂) ₁ -A ₂ -PEP _{Au}	23.07	24.77	23.55
Azo-(CH ₂) ₁ -A ₃ -PEP _{Au}	22.09	26.05	25.12
Azo-(CH ₂) ₂ -A ₁ -PEP _{Au}	23.13	25.12	25.68
Azo-(CH ₂) ₂ -A ₂ -PEP _{Au}	22.75	24.98	25.79
Azo-(CH ₂) ₂ -A ₃ -PEP _{Au}	22.55	25.35	25.21
Azo-(CH ₂) ₃ -A ₁ -PEP _{Au}	23.31	24.65	25.24
Azo-(CH ₂) ₃ -A ₂ -PEP _{Au}	22.45	23.56	24.79
Azo-(CH ₂) ₃ -A ₃ -PEP _{Au}	23.55	25.19	24.87
H ₂ O	21.55	22.37	22.88
0.1 M HEPES	20.54	22.54	23.17

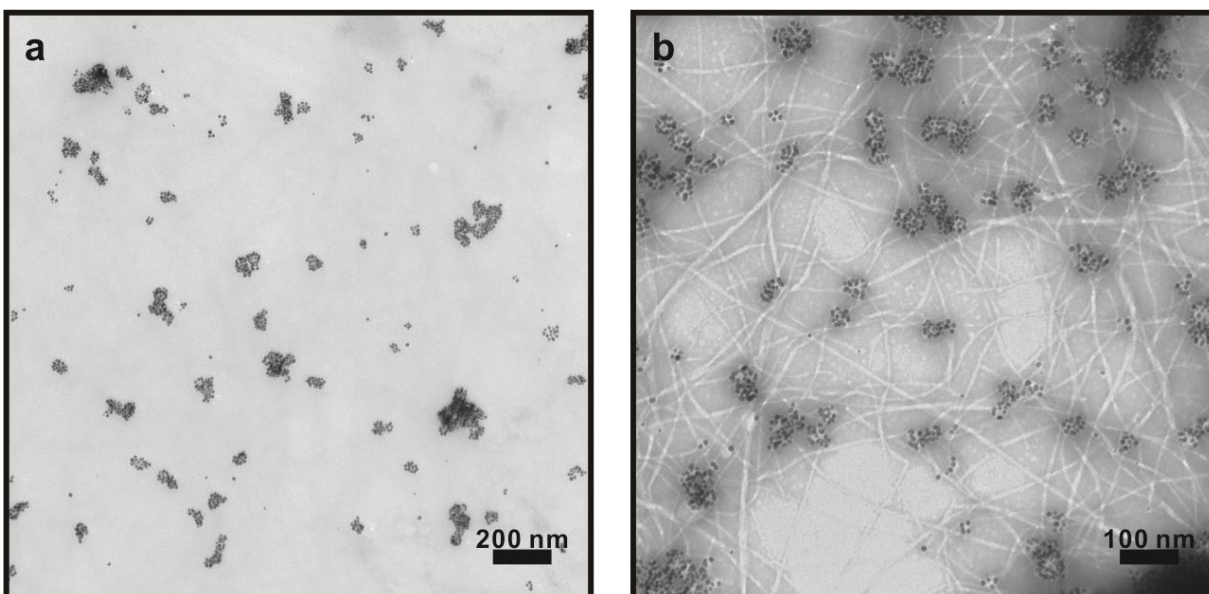


Figure 2.21. Additional TEM images of NP assemblies formed using $\text{Azo}-(\text{CH}_2)_2\text{-A}_1\text{-PEP}_{\text{Au}}$ after UV irradiation for 30 min.

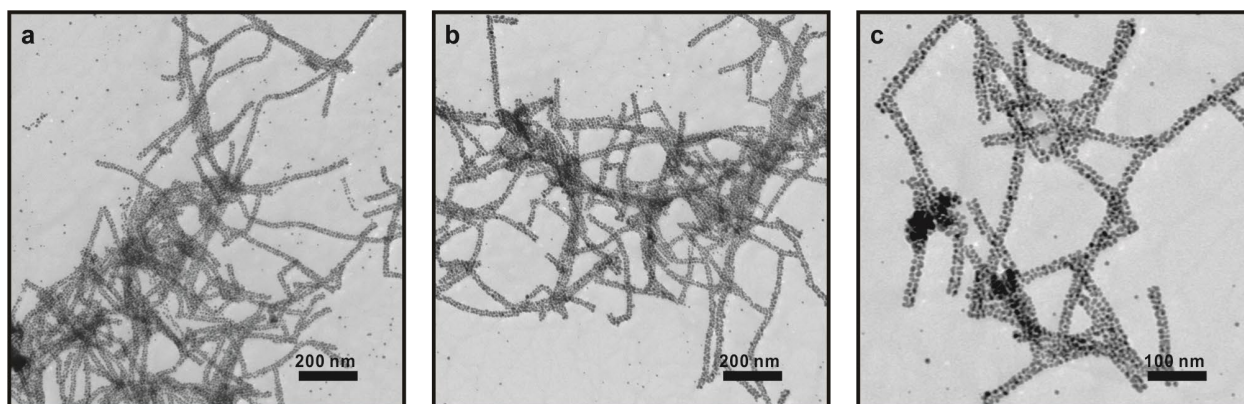


Figure 2.22. Additional TEM images for NP assemblies formed using $\text{Azo}-(\text{CH}_2)_2\text{-A}_1\text{-PEP}_{\text{Au}}$ before UV irradiation.

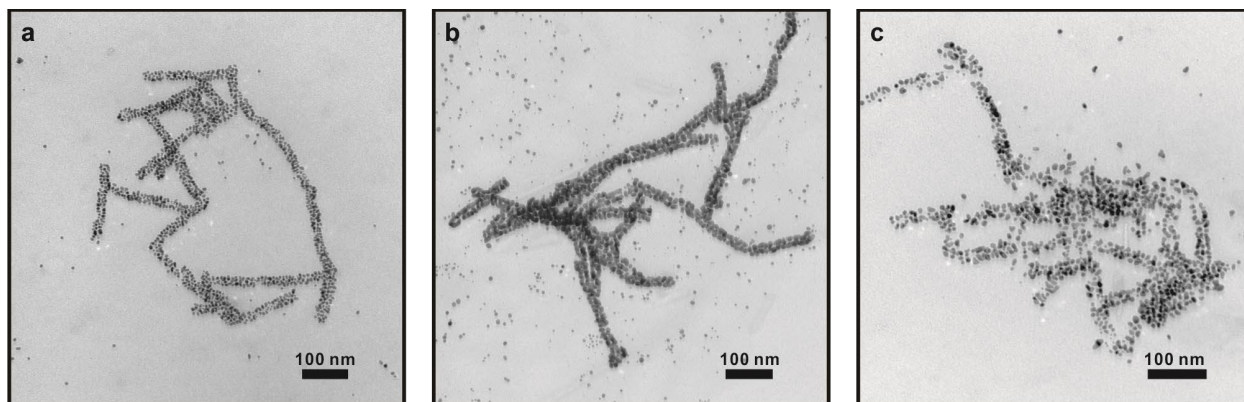


Figure 2.23. Additional TEM images for NP assemblies formed using $\text{Azo}-(\text{CH}_2)_2\text{-A}_1\text{-PEP}_{\text{Au}}$ after UV irradiation for 5 min.

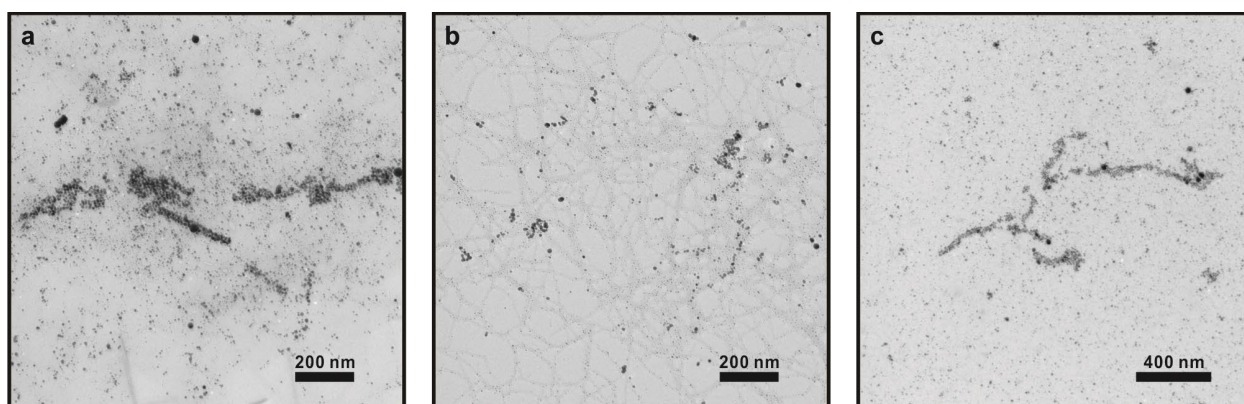


Figure 2.24. Additional TEM images for NP assemblies formed using $\text{Azo}-(\text{CH}_2)_2\text{-A}_1\text{-PEP}_{\text{Au}}$ after UV irradiation for 10 min.

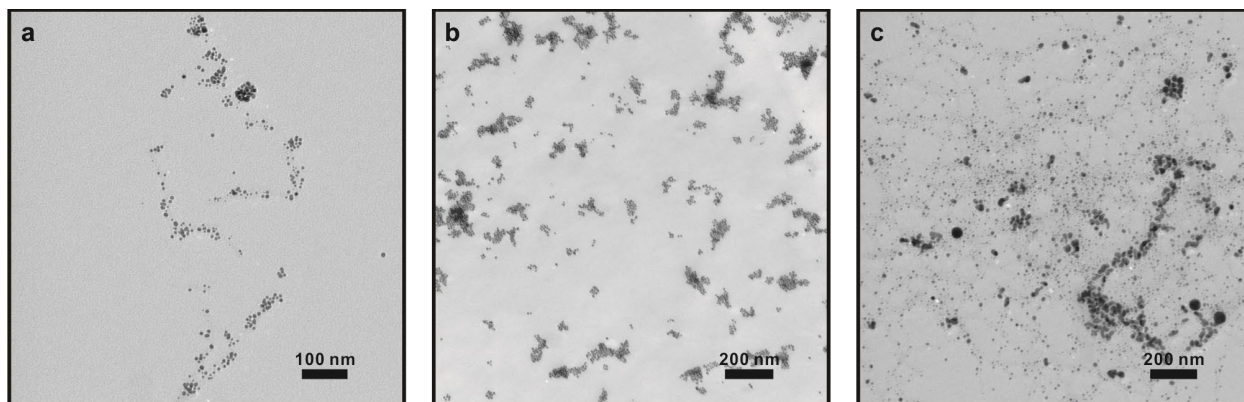


Figure 2.25. Additional TEM images for NP assemblies formed using $\text{Azo}-(\text{CH}_2)_2\text{-A}_1\text{-PEP}_{\text{Au}}$ after UV irradiation for 15 min.

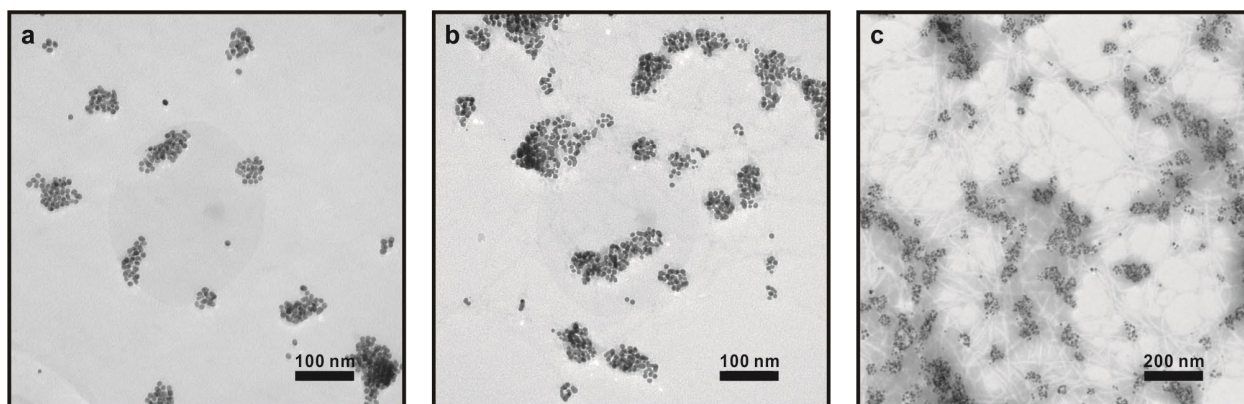


Figure 2.26. Additional TEM images for NP assemblies formed using Az0-(CH₂)₂-A₁-PEP_{Au} after UV irradiation for 30 min.

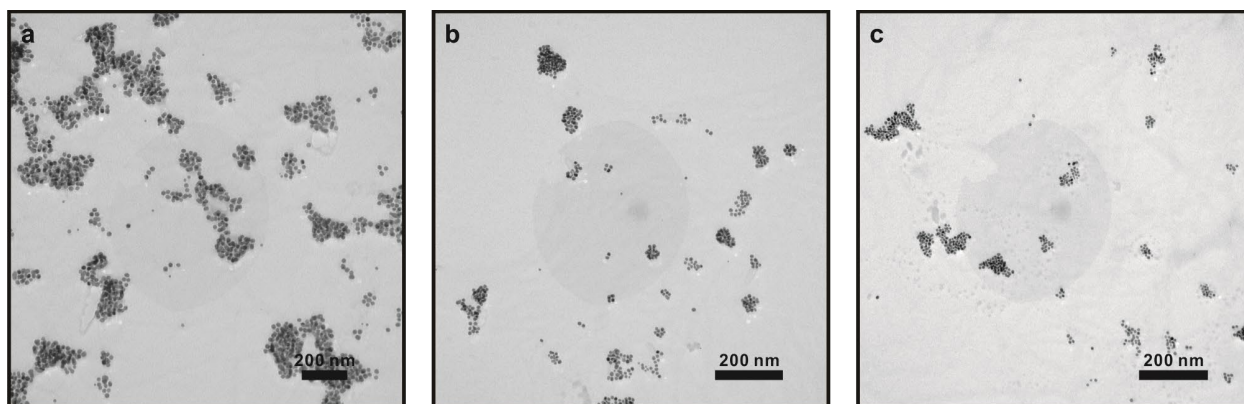


Figure 2.27. Additional TEM images for NP assemblies formed using Az0-(CH₂)₂-A₁-PEP_{Au} after visible light irradiation for 2 h.

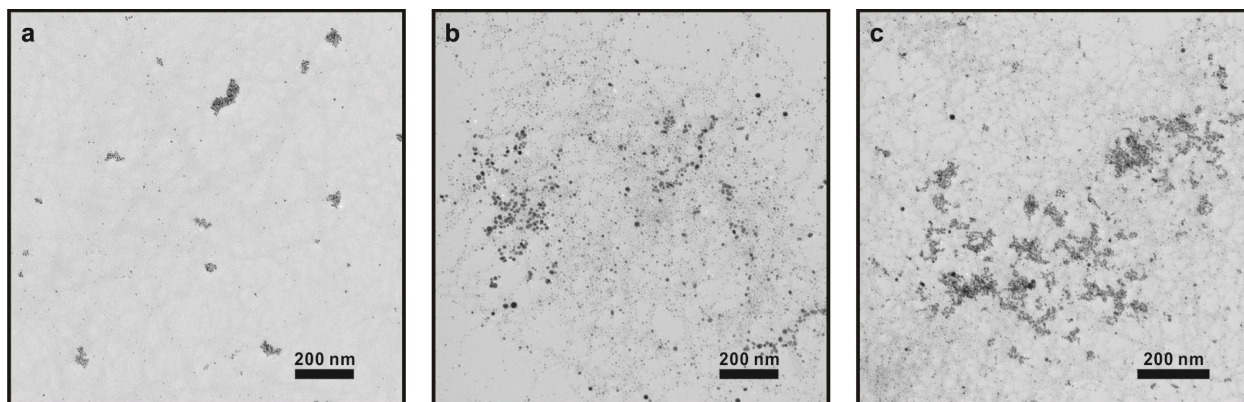


Figure 2.28. Additional TEM images for NP assemblies formed using Az0-(CH₂)₂-A₁-PEP_{Au} after visible light irradiation for 4 h.

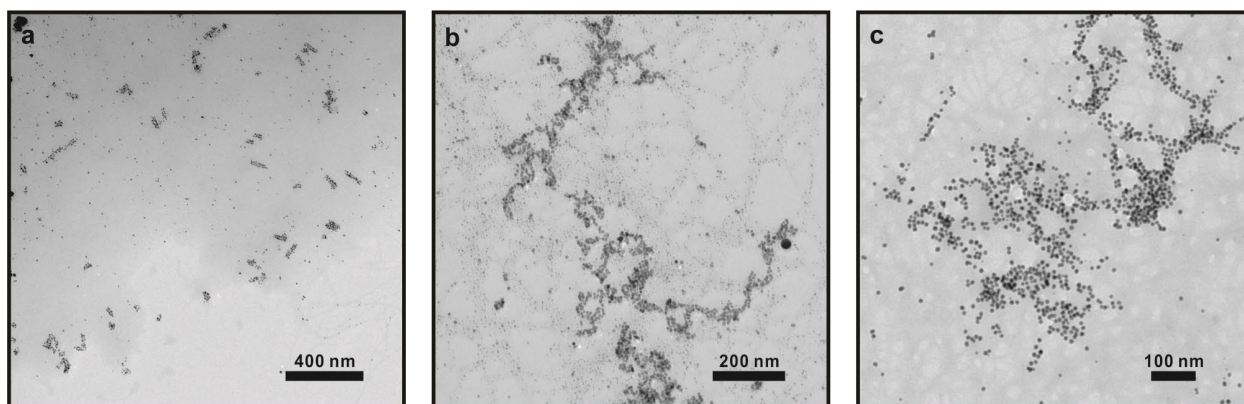


Figure 2.29. Additional TEM images for NP assemblies formed using Azo-(CH₂)₂-A₁-PEP_{Au} after visible light irradiation for 6 h.

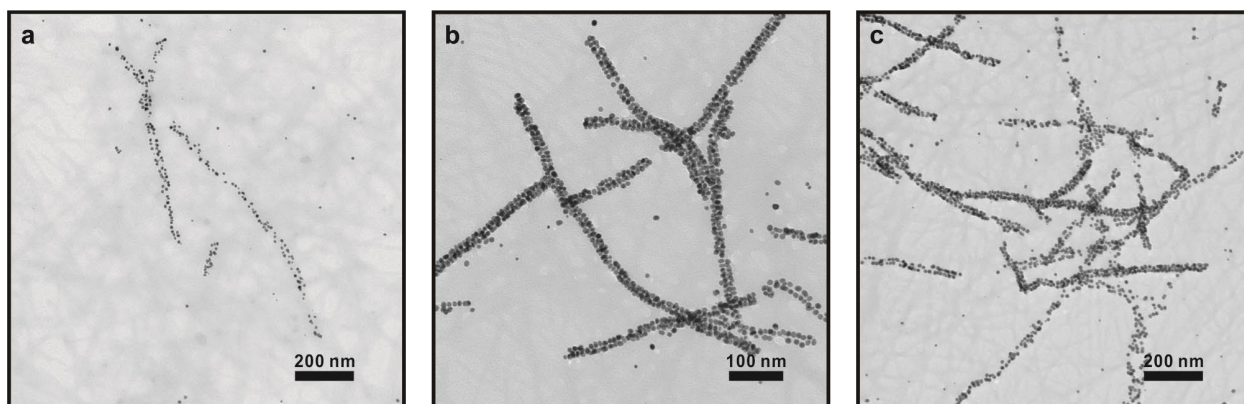


Figure 2.30. Additional TEM images for NP assemblies formed using Azo-(CH₂)₂-A₁-PEP_{Au} after visible light irradiation for 8 h.

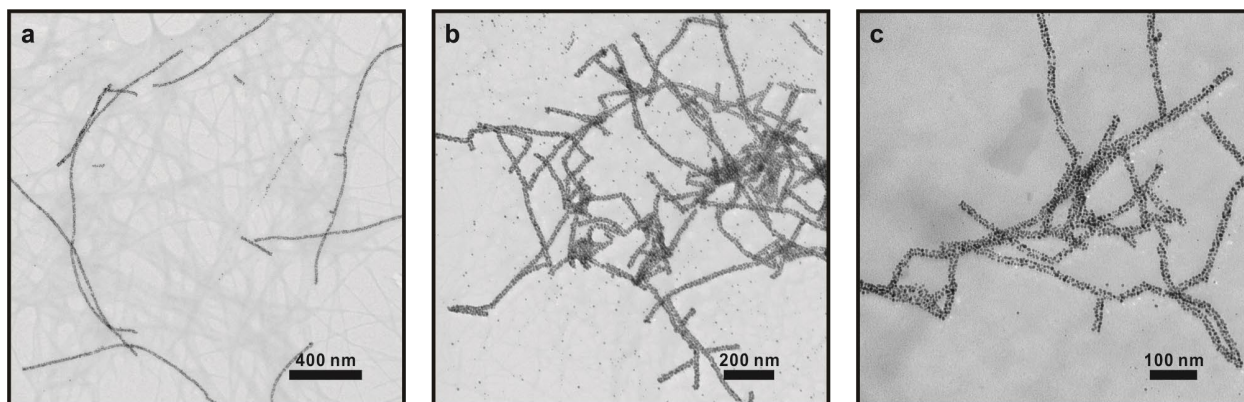


Figure 2.31. Additional TEM images for NP assemblies formed using Azo-(CH₂)₂-A₁-PEP_{Au} after visible light irradiation for 12 h.

3.0 Photo-induced Assembly of One-Dimensional Au NP Superstructures Based on Azobenzene-Cyclodextrin Host-Guest Interactions

This Chapter is based on a manuscript in the final stages of preparation.

3.1 Introduction

In the previous chapter, I described a new photo-responsive strategy for reversibly controlling the 3-D morphology of Au NP superstructures. To be more specific, a series of peptide conjugates, Azo-(CH₂)_m-A_n-PEP_{Au} (m = 1-3, n = 0-2), with varied hydrophobic and β -sheet interactions were designed to systematically tune the assembly structure and control the reversibility behavior. By tuning the length of the aliphatic spacer or the number of alanine residues between the azobenzene moiety and the peptide section, I designed a Au NP superstructure that could reversibly shift between linear and spherical morphology. Further, by adjusting conjugate composition, I was able to design conjugates that were more or less responsive to UV or visible light irradiation. It was also revealed that some superstructures exhibited no change in morphology upon irradiation, because the hydrophobic-hydrophobic and β -sheet hydrogen bonding interactions enable the assembly to remain as one-dimensional fibers regardless of irradiation time. These observations led to the following question: could we design a molecular “lock” that prevents peptide conjugate assembly and, upon release of the lock, could the peptide conjugate assemble? Further, could this strategy enable ‘turn-on’ assembly of Au NPs, where release of the lock would

induce assembly of discrete, dispersed Au NP? We envision that this sort of system could be useful for on-demand triggered assembly of functional NP superstructures at specific times and locations.

My attention was drawn to cyclodextrin (CD), which can form host-guest complexes with azobenzene (Azo) groups.¹⁷²⁻¹⁷⁴ When in the *trans* conformation, Azo can reside in the hydrophobic cavity of the CD molecule;¹⁷⁴ upon UV irradiation, the *cis* Azo isomer is released from the hydrophobic cavity, resulting in dissociation of the two molecules. This interesting host-guest mechanism served as the basis of many stimuli-responsive materials which can be controlled by irradiating UV or visible light,¹⁷³ many of which are potentially useful for optical sensing,¹⁷⁵ cell recognition,¹⁷⁶ and drug release.¹⁷⁷⁻¹⁷⁸

Here, I introduce a new strategy of assembling discrete, dispersed Au NPs into one-dimensional superstructures using Azo/CD-functionalized peptide conjugates upon UV light irradiation (Figure 3.1). The peptide conjugate, termed Azo-(CH₃)₃-A-PEP_{Au}, which was found in Chapter 2 to direct assembly of non-photoresponsive 1-D Au NP superstructures, is functionalized with a β -CD molecule. The modified conjugate, Azo/CD-(CH₃)₃-A-PEP_{Au}, is not capable of directing Au NP assembly into any well-defined morphology; however, upon UV irradiation, the β -CD molecule is released from the conjugate, prompting the Au NPs to assemble into one-dimensional structure directed by Azo-(CH₃)₃-A-PEP_{Au}. The results exemplify the versatility of the peptide conjugate-based platform for Au NP assembly and point toward remote-controlled NP colloids that can assemble into target superstructures upon input of stimulus.

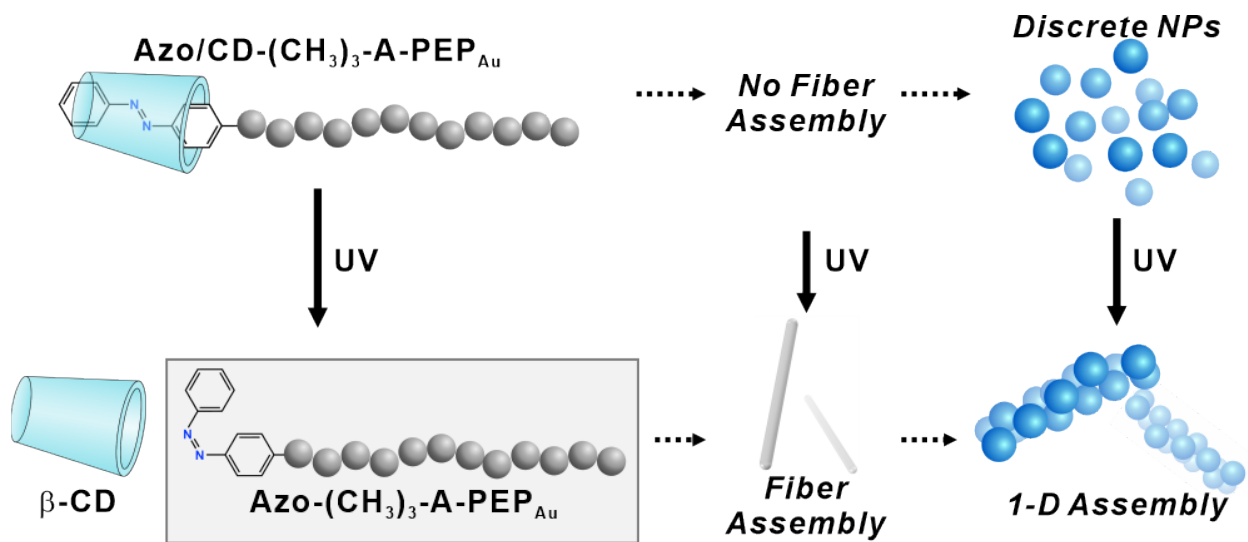


Figure 3.1. Schematic representation of light-triggered peptide fiber assembly and one-dimensional Au NP superstructures by UV-induced β -CD removal from azobenzene incorporated peptide conjugate.

3.2 Results and Discussions

3.2.1 Stability of $\text{Azo/CD-(CH}_3\text{)}_3\text{-PEP}_{\text{Au}}$

The synthesis of peptide conjugate $\text{Azo/CD-(CH}_3\text{)}_3\text{-PEP}_{\text{Au}}$ was completed using the previously reported method using microwave-assisted solid-phase peptide synthesis protocol. Purification of the conjugate via a reverse-phase high-performance liquid chromatography (RP-HPLC) revealed two neighboring peaks in the chromatograph, with the first being $\text{Azo/CD-(CH}_3\text{)}_3\text{-A-PEP}_{\text{Au}}$ (Figure 3.2), as confirmed by MALDI-TOF mass spectroscopy (Figure 3.3); the second peak corresponded to $\text{Azo-(CH}_3\text{)}_3\text{-A-PEP}_{\text{Au}}$. The results from HPLC and mass spectroscopy indicated that the β -CD molecule may not be strongly associated with the Azo peptide conjugate during purification. It is therefore critical to confirm that β -CD remains associated with $\text{Azo-(CH}_3\text{)}_3\text{-A-PEP}_{\text{Au}}$, in particular in the buffer solutions used during preparation of the Au NP

superstructures. Because previous results showed that Azo-(CH₃)₃-A-PEP_{Au} assembles into stable, one-dimensional fibers, even after both UV or visible light irradiation, an ‘unstable’ Azo/CD-(CH₃)₃-A-PEP_{Au} peptide conjugate would very likely form one-dimensional fibers prior to attempting photo-induced removal of β-CD.

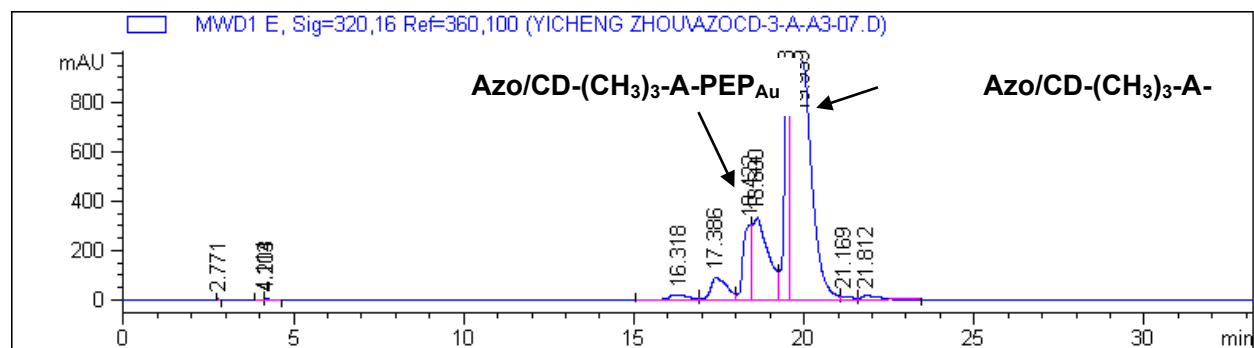


Figure 3.2. RP-HPLC elution of Azo/CD-(CH₃)₃-A-PEP_{Au}

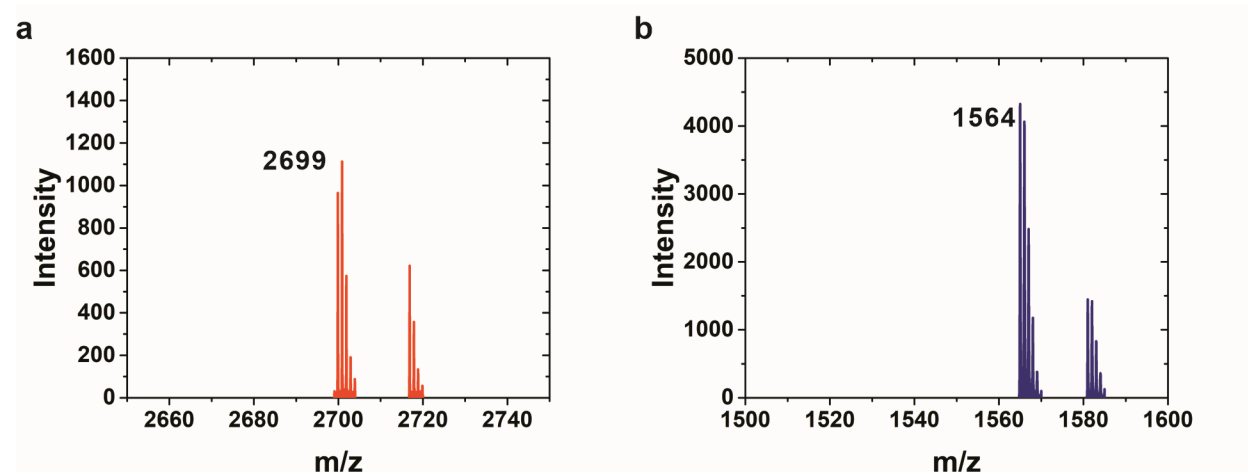


Figure 3.3. MALDI-TOF spectra of (a) Azo/CD-(CH₃)₃-A-PEP_{Au} (calc. 2676, found [M+Na]⁺ = 2699) and (b) Azo-(CH₃)₃-A-PEP_{Au} (calc. 1564, found [M]⁺ = 1564).

We performed several tests to examine the equilibrium between associated and dissociated Azo/CD-(CH₃)₃-A-PEP_{Au}. Purified Azo/CD-(CH₃)₃-A-PEP_{Au} was dissolved in 200 μL 0.1 M 4-(2-hydroxyethyl)piperazine-1-ethanesulfonic acid (HEPES) buffer. After 30 min, negatively

stained TEM images showed a mixture of both spherical and fiber structures (Figure 3.4a, b and Figure 3.5). Our previous studies showed that Azo-(CH₃)₃-A-PEP_{Au} rapidly assembles in HEPES buffer into one-dimensional fibers (Figure 3.16), which suggests that the observed fibers result from dissociation of β -CD from Azo/CD-(CH₃)₃-A-PEP_{Au}. To further confirm fiber formation, dynamic light scattering (DLS) and thioflavin-T (ThT) fluorescence staining were used to monitor the assembly process over time. For DLS studies, as shown in Figure 3.4c, two significant peaks were observed starting at 5 min, a peak corresponding to spherical structures (~200 nm) and another peak at ~6000 nm, which is likely due to anisotropic fiber structures within the sample. ThT fluorescence assays can also be used to monitor amyloid fiber formation. ThT is a fluorescent dye which is commonly used as an indicator for amyloid fibers, especially β -sheet secondary structure in peptide fibers. When excited at 450 nm, ThT emission at 485 nm can be recorded in the presence of peptide fibers. For Azo/CD-(CH₃)₃-A-PEP_{Au} assemblies in 0.1 M HEPES buffer and 5 mM ThT, significant emissions at 485 nm were observed at early stages of assembly (Figure 3.4d), which confirms the formation of peptide fibers. Taken together, the findings from TEM, DLS, and fluorescence studies indicate non-negligible dissociation of β -CD from the conjugate, which could potentially affect our target studies on photo-induced induction of both peptide and NP assembly.

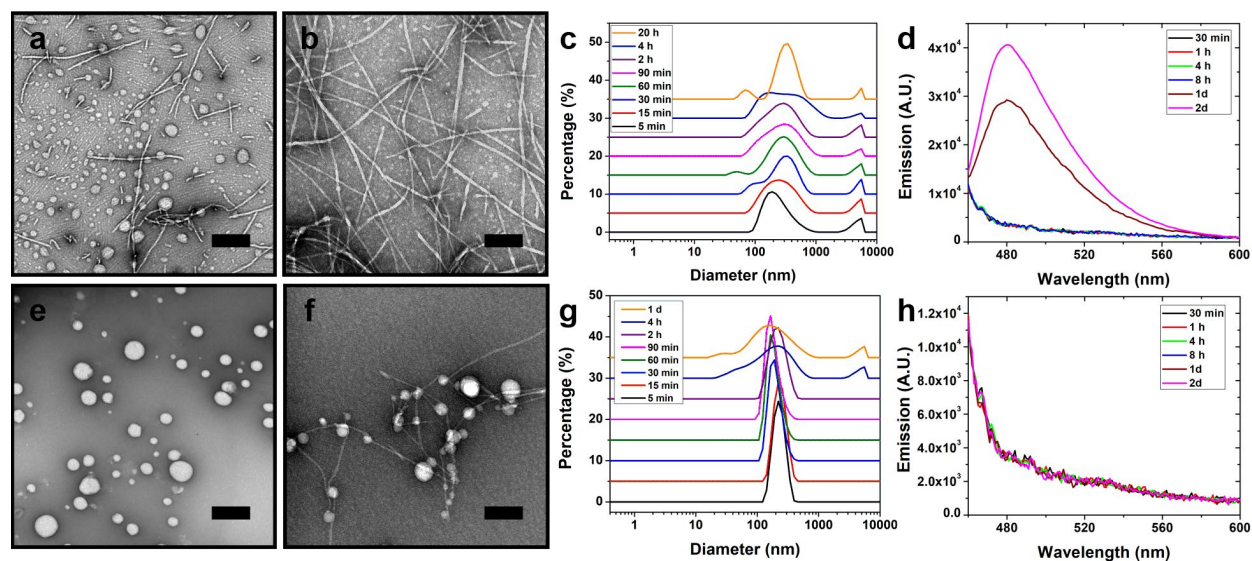


Figure 3.4. Assembly studies of Azo/CD-(CH₃)₃-A-PEP_{Au} in the absence (a-d) and presence (e-h) of additional β -CD in HEPES buffer. (a, b) Negatively stained TEM images of Azo/CD-(CH₃)₃-A-PEP_{Au} assemblies in 0.1 M HEPES buffer at 5 min (a) and 30 min (b). (c) DLS data of Azo/CD-(CH₃)₃-A-PEP_{Au} assemblies in 0.1 M HEPES buffer over a period of 20 hrs. (d) ThT emissions of Azo/CD-(CH₃)₃-A-PEP_{Au} assemblies in 0.1 M HEPES buffer recorded up to 2 d. (e, f) Negatively stained TEM images of Azo/CD-(CH₃)₃-A-PEP_{Au} assemblies in 0.1 M HEPES/ β -CD mixed buffer at 30 min (e) and 1 d (f). (g) DLS data of Azo/CD-(CH₃)₃-A-PEP_{Au} assemblies in 0.1 M HEPES/ β -CD mixed buffer over a period of 1 d. (h) ThT emissions of Azo/CD-(CH₃)₃-A-PEP_{Au} assemblies in 0.1 M HEPES/ β -CD mixed buffer recorded up to 2 d. Scale bar = 200 nm.

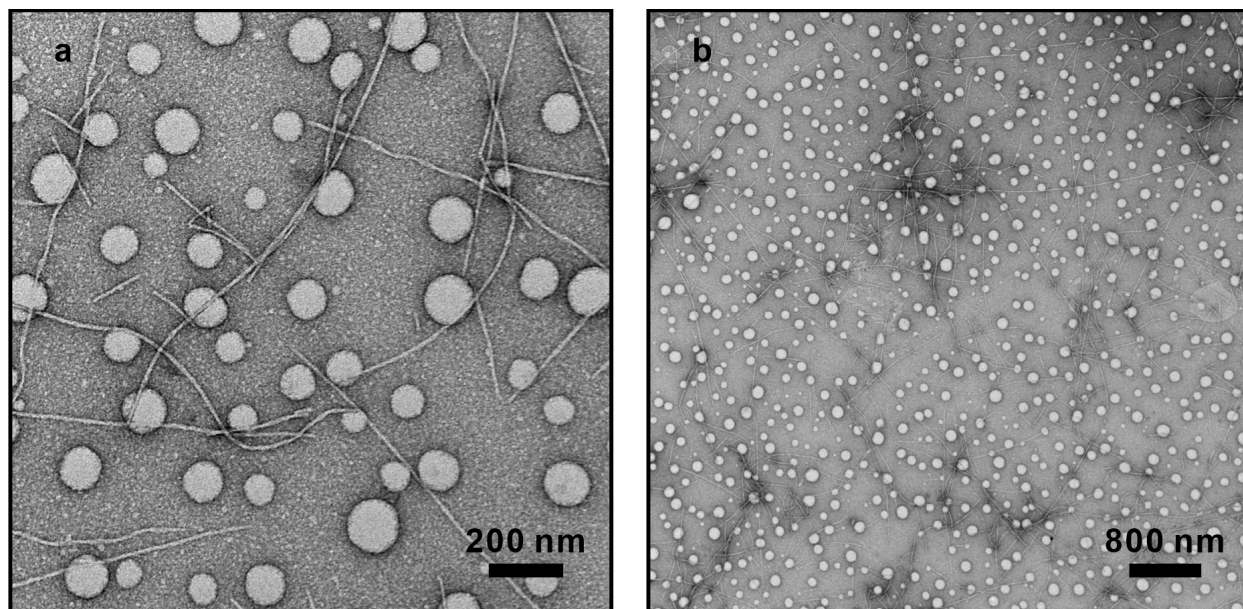


Figure 3.5. Negatively stained TEM images of assemblies of Azo/CD-(CH₃)₃-A-PEP_{Au} in 0.1 M HEPES buffer at 5 min.

To help reduce dissociation of β -CD, we decided to carry out the assembly in the presence of β -CD saturated HEPES buffer. We predicted that a higher concentration β -CD in HEPES buffer would prevent β -CD from dissociating from the conjugate, i.e., shifting the equilibrium toward formation of Azo/CD-(CH₃)₃-A-PEP_{Au}. We conducted the same Azo/CD-(CH₃)₃-A-PEP_{Au} assembly experiments described previously, except now in β -CD saturated 0.1 M HEPES buffer. Negatively stained TEM images revealed that at 30 min incubation time (Figure 3.4e), no fiber assembly was observed. In fact, fiber assembly was only observable after incubating with 0.1 M HEPES/ β -CD mixed buffer for 1 d (Figure 3.4f). Furthermore, the DLS data revealed that only one peak (\sim 200 nm), corresponding to spherical structures, was present at early stages of assembly in the HEPES/ β -CD mixed buffer. For incubation up to 1 d, a second peak emerged (\sim 6000 nm), indicating peptide fiber formations. Additionally, ThT emission experiments showed that the ThT fluorescence signal intensity remained relatively low for assemblies in the HEPES/ β -CD mixed

buffer, which suggests that the peptide fiber formation is prohibited because additional β -CD in the solution inhibited the dissociation of β -CD from Azo/CD-(CH₃)₃-A-PEP_{Au} conjugate. To summarize the results thus far, we demonstrated that by adding extra β -CD to the HEPES buffer can prevent β -CD from dissociating from the Azo/CD-(CH₃)₃-A-PEP_{Au} conjugate. Due to its bulky organic head, Azo/CD-(CH₃)₃-A-PEP_{Au} does not assemble into fiber structures and, we would therefore predict that it likewise would not direct the assembly of 1-D NP superstructures.

3.2.2 UV-Induced Peptide Conjugate Assembly

Based on the results presented in the previous section, we continued to study the assembly of Azo/CD-(CH₃)₃-A-PEP_{Au} in the β -CD saturated HEPES buffer in the presence of UV light. First, 20 nmol of Azo/CD-(CH₃)₃-A-PEP_{Au} was dissolved in 200 μ L β -CD saturated 0.1 M HEPES buffer. After 30 min, spherical assemblies were observed via TEM (Figure 3.6a). At this time, the sample was irradiated with UV light (355 nm) using a laser source for 30 min. After irradiation, peptide fiber assemblies were observed via TEM imaging (Figure 3.6b), and the fibers remained intact after exposure to ambient light for up to 1 d (Figure 3.7). To confirm the formation of fiber assemblies, DLS was employed to monitor the irradiation process. As shown in Figure 3.6c, a hydrodynamic diameter at \sim 200 nm was recorded before UV irradiation. Upon UV irradiation for 30 min, the peak at \sim 200 nm started to disappear and peaks corresponding to larger hydrodynamic diameters were observed. The emergence of larger hydrodynamic diameters might suggest the formation of fiber structures of different lengths, as shown in TEM images in Figure 3.6b. (It should be noted that DLS is most reliable on isotropic samples.) When the sample was left undisturbed after UV irradiation (e.g., for 1 hr), the peak corresponding to smaller spherical

assemblies was not observed, suggesting that the formed fiber structures remain intact after UV is applied. To further examine whether irradiation time affects the degree of the fiber formation, we selected three different time lengths for UV irradiation: 5 min, 30 min and 2 h. The irradiation process was monitored by ThT fluorescence (Figure 3.6d). Before irradiation, no significant emission peak was observed for the sample, indicating the absence of fibers in the solution. Upon UV irradiation for 5 min, the ThT emission peak at 485 nm appeared. Irradiation of the sample for 30 min further increased ThT emission, indicating fiber formation. After 2 h of irradiation, the ThT emission intensity did not increase any further, indicating that the photo-isomerization of azobenzene is complete at 5 to 30 min of irradiation. Based on this result, setting the UV irradiation time at 30 min could ensure complete photo-isomerization. To summarize, the results from these conjugate assembly studies reveal that the photo-induced transition of azobenzene leads to the formation of fiber assemblies by Azo-(CH₃)₃-A-PEP_{Au} due to the dissociation of β -CD from the conjugate.

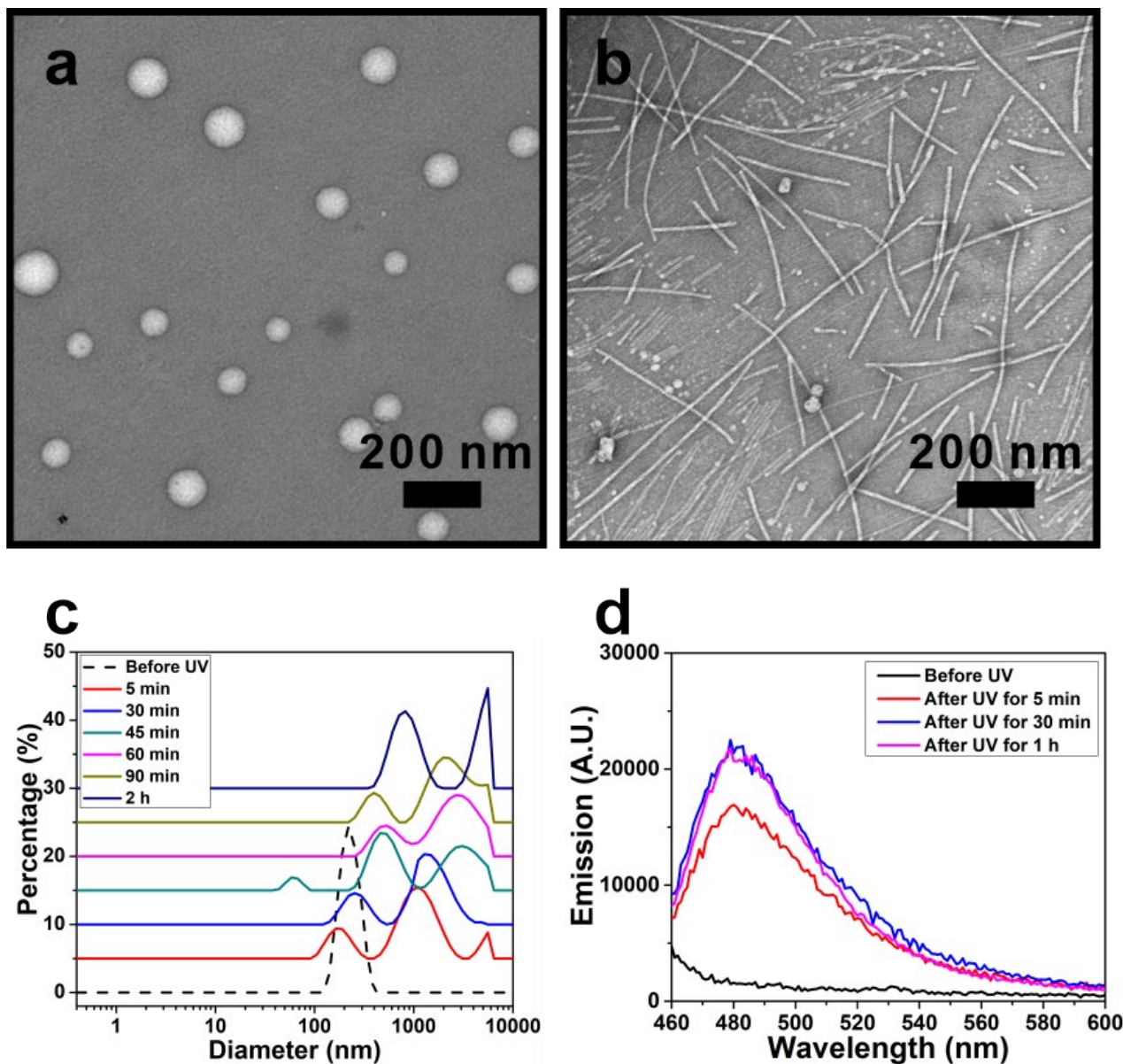


Figure 3.6. UV irradiation of assemblies of Azo/CD-(CH₃)₃-A-PEP_{Au} in β -CD saturated 0.1 M HEPES buffer. (a, b) Negatively stained TEM images of assemblies of Azo/CD-(CH₃)₃-A-PEP_{Au} in 0.1 M HEPES buffer saturated by β -CD before (a) and after (b) UV irradiation for 30 min. (c) DLS data recorded before and after UV irradiation of the sample for 30 min. (d) Effect of the time lengths of UV irradiation monitored via ThT emission spectra.

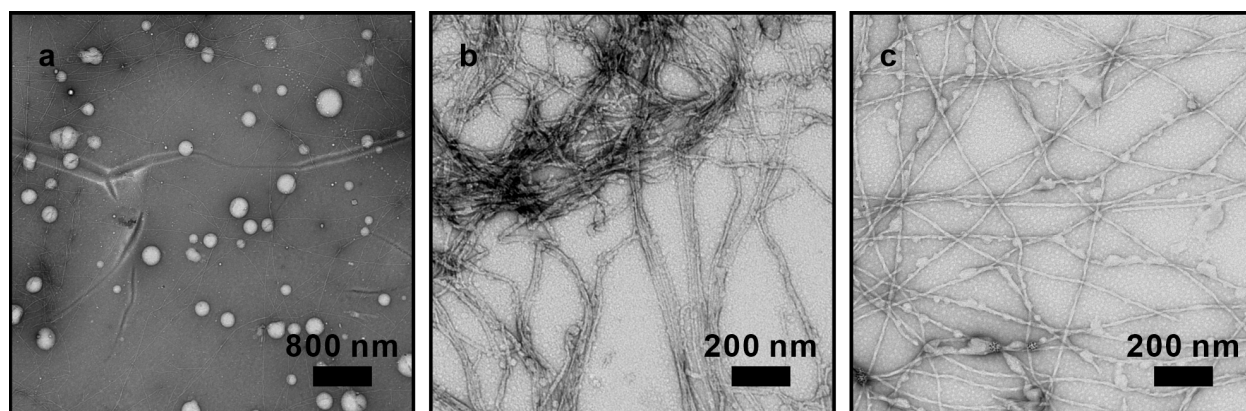


Figure 3.7. Negatively stained TEM images of assemblies of Azo/CD-(CH₃)₃-A-PEP_{Au} in 0.1 M HEPES buffer (a) before irradiation, (b) after UV irradiation for 30 min, and (c) after visible light irradiation for 4 hrs.

3.2.3 NP Assembly

Having explored the assembly of Azo/CD-(CH₃)₃-A-PEP_{Au}, we proceeded to investigate whether Azo/CD-(CH₃)₃-A-PEP_{Au} could be used to as a ‘photo-triggered’ molecular agent for directing the assembly of 1-D nanoparticle superstructures. As we have showed in our previous studies (Ch. 2), Azo-(CH₃)₃-A-PEP_{Au} can direct the assembly of 1-D AuNP superstructures. Based on the assembly data of Azo/CD-(CH₃)₃-A-PEP_{Au}, we predicted that Azo/CD-(CH₃)₃-A-PEP_{Au} would yield spherical NP superstructures that, upon UV irradiation, would transition to linear NP superstructures. We used our established procedures for preparing NP superstructures (see Supporting Information for details). Briefly, 20 nmol of Azo/CD-(CH₃)₃-A-PEP_{Au} was dissolved in 200 μ L of β -CD saturated 0.1 M HEPES buffer for 30 min, at which time a gold precursor consisting HAuCl₄ and triethylammonium acetate (TEAA) was injected into the peptide solution to initiate particle growth. TEM images of the product revealed primarily discrete non-assembled Au NPs and a few NP clusters but no well-defined spherical superstructures (Figure 3.8a, Figure

3.9a-d). The Au NPs remained as discrete NPs for up to 1 d (Figure 3.10a-b). In contrast, the Azo/CD-(CH₃)₃-A-PEP_{Au} would assemble into spherical structures without any Au precursor added as shown in the previous section. However, when the Au NP sample was irradiated with UV light for 30 min, a clear transition in Au NP assembly morphology from discrete NP to linear NP assembly was observed (Figure 3.8b and Figure 3.9). We also noted that there was also a large number of discrete NPs present in the samples after UV irradiation as shown in the TEM images.

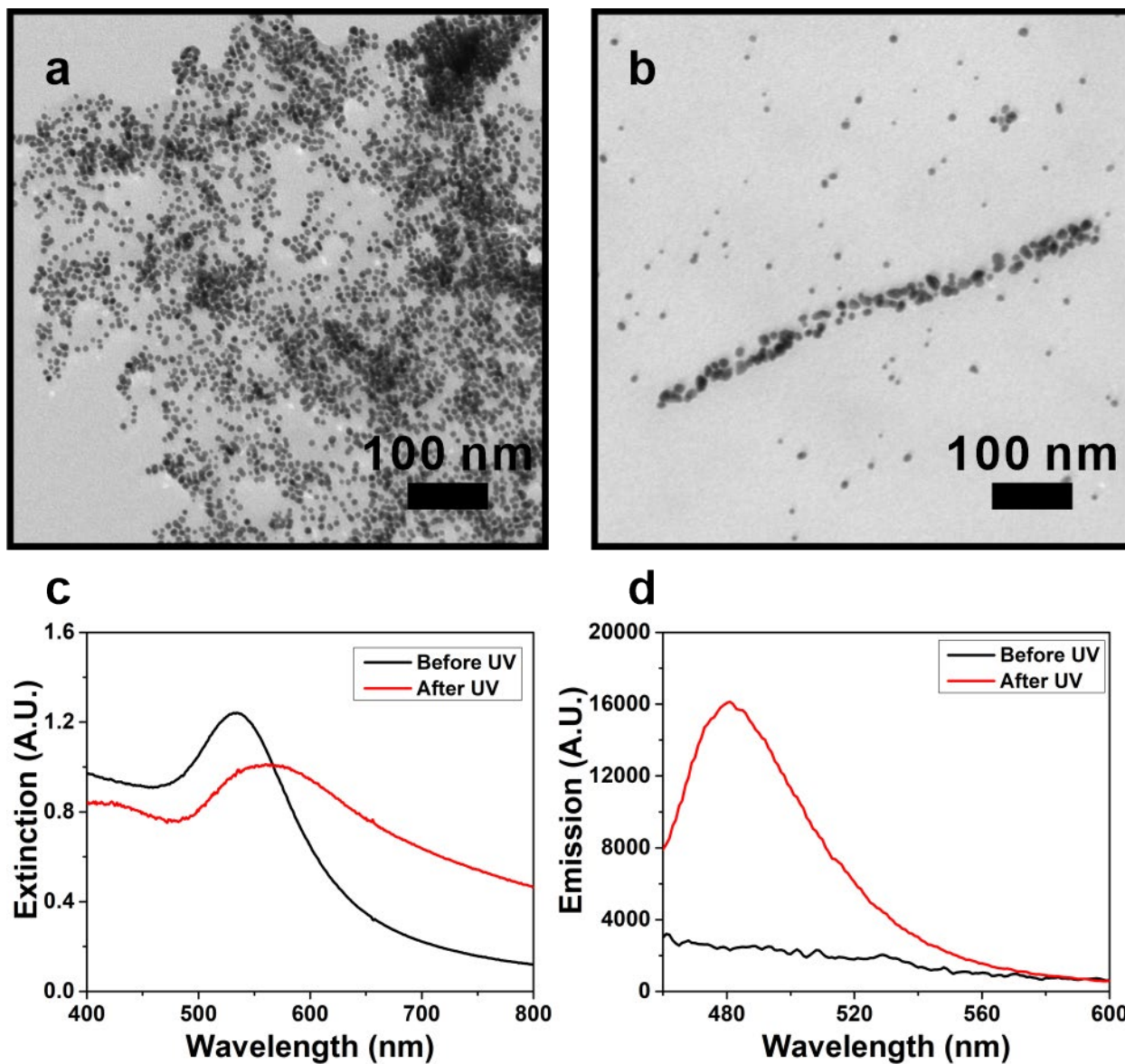


Figure 3.8. UV irradiation of Au NPs directed by Azo/CD-(CH₃)₃-A-PEP_{Au}. (a, b) TEM images of Au NPs directed by Azo/CD-(CH₃)₃-A-PEP_{Au} before (a) and after (b) irradiation for 30 min. (c) UV-Vis spectra of the Au NPs before and after UV irradiation for 30 min. (d) ThT fluorescence emission spectra (ex. 450 nm) of Au NPs before and after UV irradiation for 30 min.

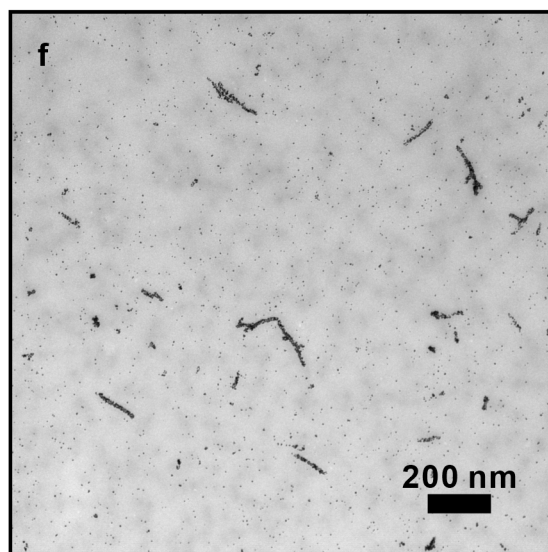
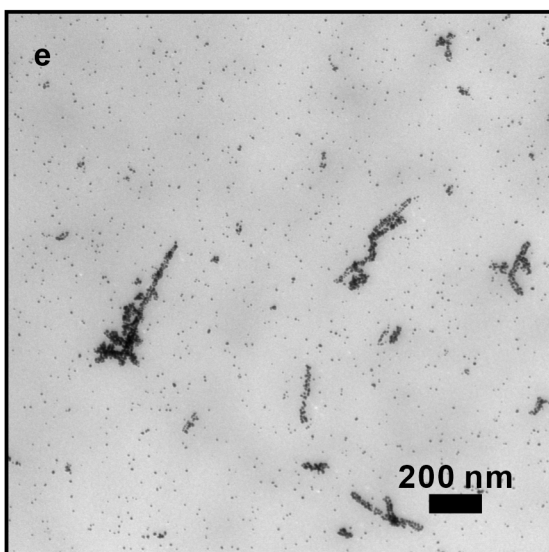
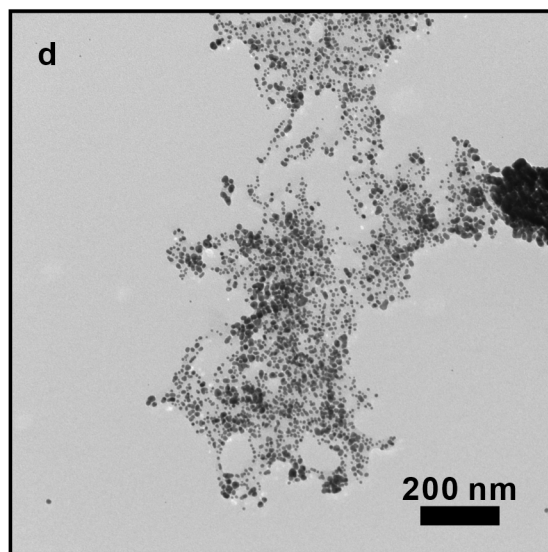
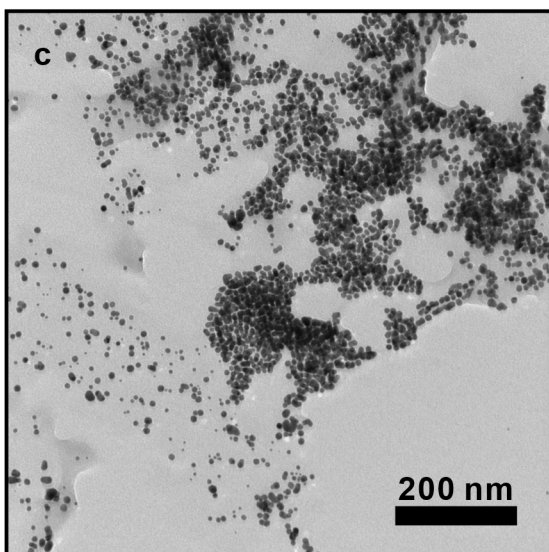
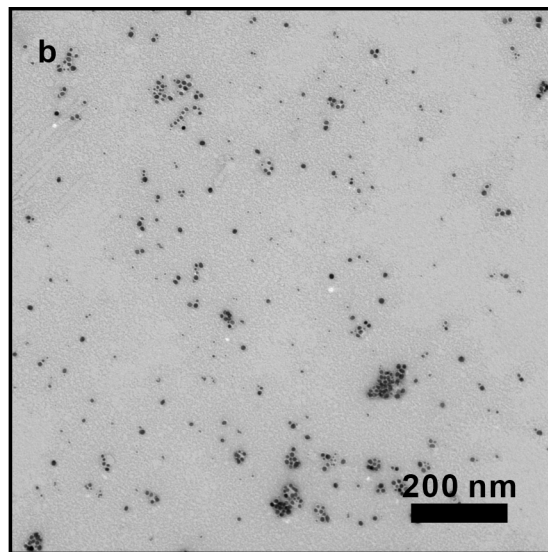
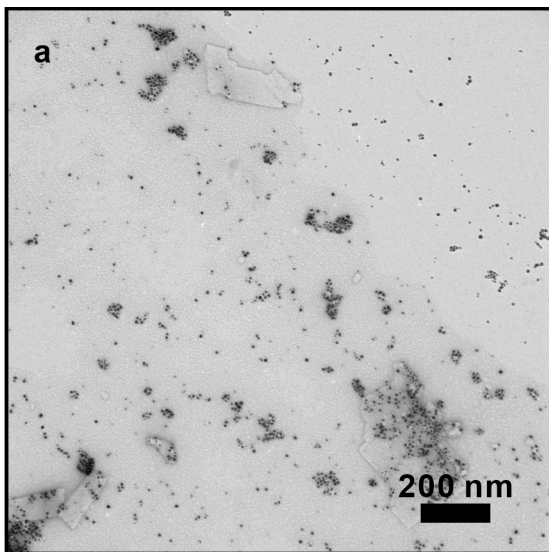


Figure 3.9. Additional TEM images of Au NPs directed by Azo/CD-(CH₃)₃-A-PEP_{Au} in 0.1 M HEPES buffer saturated by β -CD before (a-d) and after (e, f) UV irradiation for 30 min.

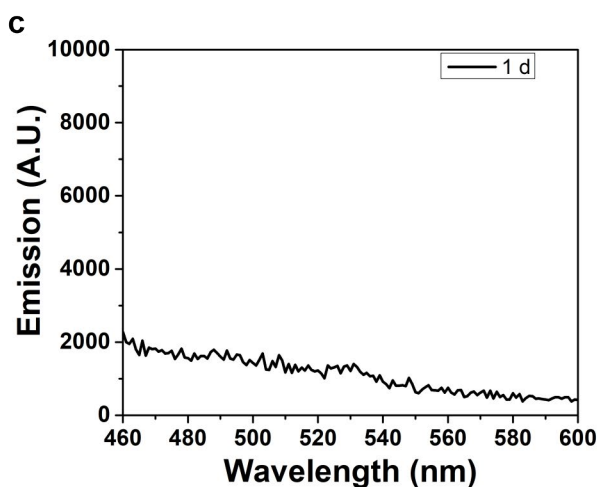
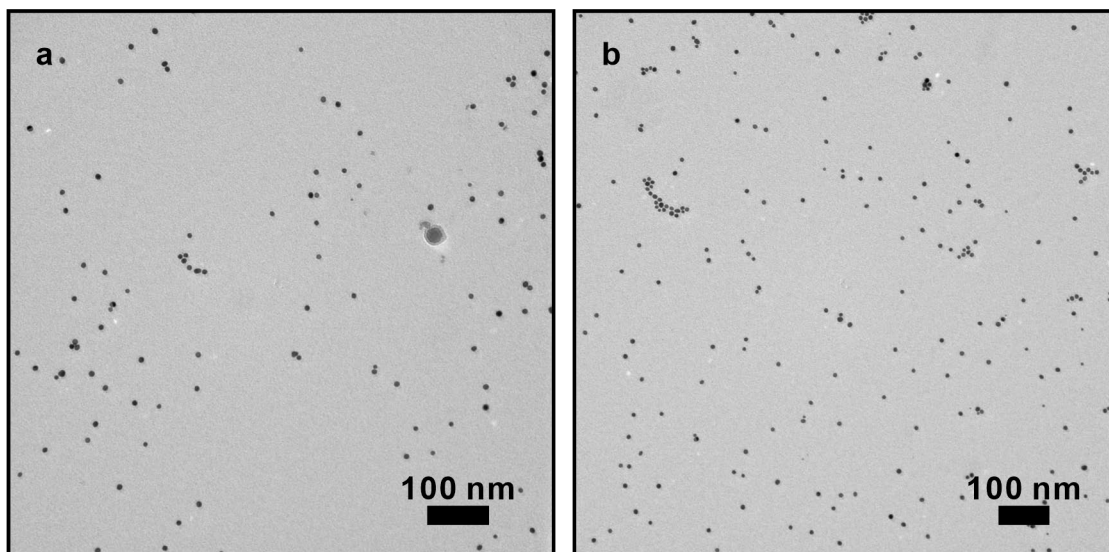


Figure 3.10. (a, b) TEM images and (c) ThT fluorescence of Au NPs directed by Azo/CD-(CH₃)₃-A-PEP_{Au} after incubating in 0.1 M HEPES saturated with β -CD for 1 d.

To confirm the morphological transition, we recorded the UV-Vis spectra of the sample before and after UV irradiation. Upon UV irradiation, the LSPR band of the Au NPs red-shifted from 533 nm to 561 nm, indicating plasmon coupling in the one-dimensional assembly of Au NPs. It should also be noted that the broadening of the LSPR band also indicates the presence of both discrete NPs and one-dimensional assemblies in the solution.

To verify that the assembly of 1-D superstructures is due to photo-triggering of the Azo/CD-(CH₃)₃-A-PEP_{Au} conjugate, we replaced Azo/CD-(CH₃)₃-A-PEP_{Au} with PEP_{Au} (AYSSGAPMPPF). PEP_{Au} directs formation of discrete NPs in the presence of HEPES and the Au³⁺ precursor (Figure 3.11a). PEP_{Au} caps the surface of the Au particles. We mixed these particles with equimolar Azo-(CH₃)₃-A-PEP_{Au} (Figure 3.11b) or Azo/CD-(CH₃)₃-A-PEP_{Au} (Figure 3.11c). Negatively stained TEM images showed a clear distinction between Au NPs and the one-dimensional fiber assemblies. UV irradiation did not induce re-organization of Au NPs to form any well-defined superstructures (Figure 3.11d). These results indicate that the morphological transition from discrete NPs to one-dimensional superstructures is due to the photo-transition of the Azo/CD-(CH₃)₃-A-PEP_{Au} conjugate capping the Au NPs.

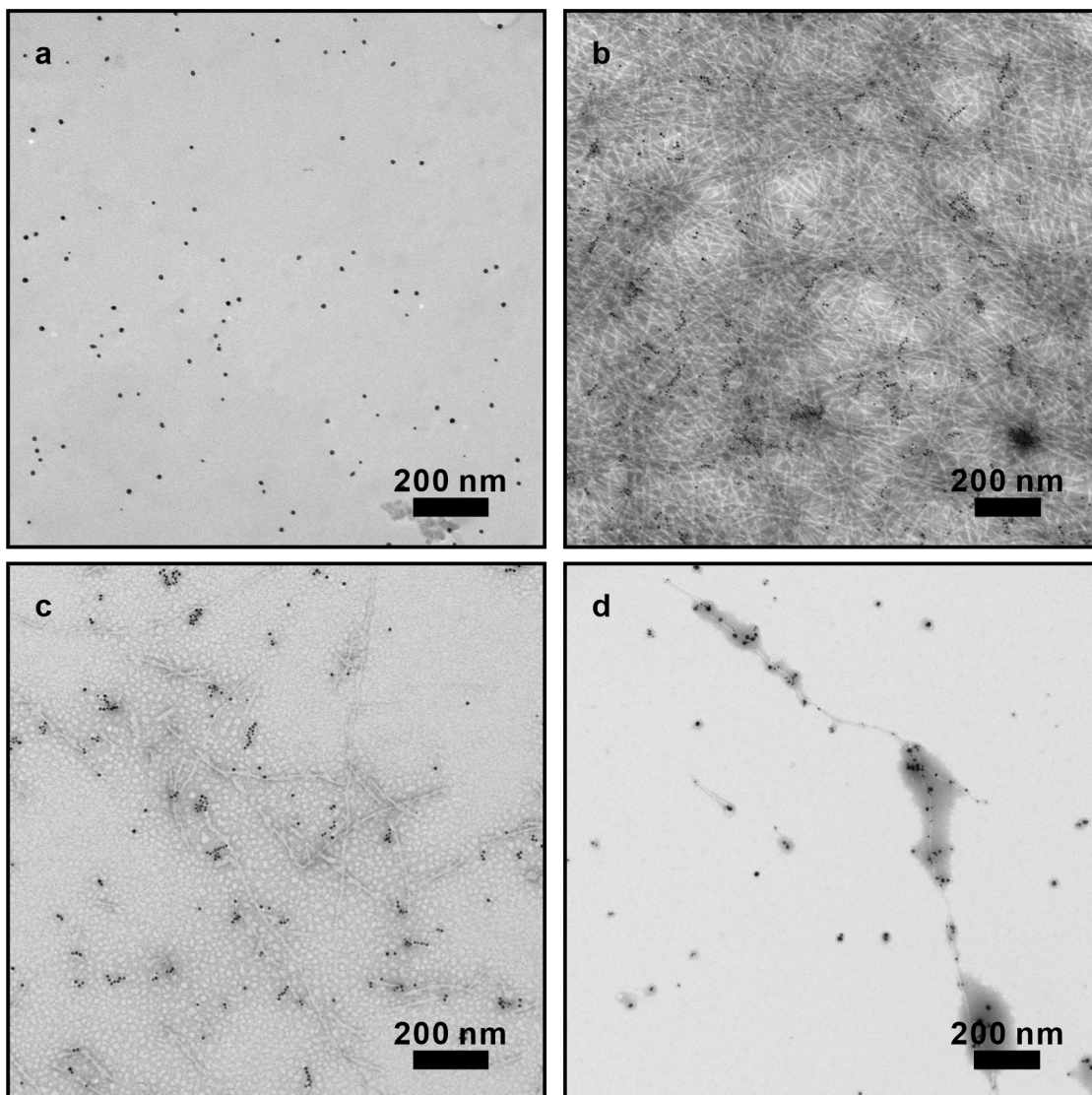


Figure 3.11. (a) TEM image of Au NPs synthesized using PEP_{Au}. (b, c) Negatively stained TEM images of PEP_{Au} capped Au NPs in the presence of equimolar Azo-(CH₃)₃-A-PEP_{Au} (b) or Azo/CD-(CH₃)₃-A-PEP_{Au} (c). (d) Negatively stained TEM image of Au NPs sample in (c) after UV irradiation for 30 min.

3.3 Conclusion

In this study, we have described and demonstrated a new strategy to form one-dimensional Au NP assemblies from discrete NPs by capitalizing on the host-guest interaction between azobenzene and β -CD. Upon removal of β -CD by UV light irradiation, the remaining Azo-(CH₃)₃-A-PEP_{Au} is capable of reorganizing the Au NPs into one-dimensional assemblies. β -CD molecule works as “lock” for Au NPs and UV irradiation “unlocks” the one-dimensional superstructure. Although optimization of the yield of the resulting 1-D superstructures is still ongoing, we envision that this new strategy could lead to the development of similar photo-induced NP assembly systems could enable on-demand assembly of nanoparticle superstructures from precursor Au colloidal solutions.

3.4 Supplementary Information

3.4.1 General Methods

All chemicals were purchased from commercially available sources and used as received unless otherwise specified. Nanopure water (18.2 m Ω) was obtained using a Barnstead DiamondTM water purification system. ¹H-NMR spectra were recorded on a Bruker DRX 300 spectrometer. Chemical shifts were recorded in ppm (parts per million) based on residual solvent peaks as internal reference (d₆-DMSO δ : 2.54 (¹H)). Peptide and peptide conjugate syntheses were carried out on a CEM MARS 6TM synthesis microwave reactor. Peptide and peptide conjugates were purified using an Agilent 1200 reverse-phase high-performance liquid chromatography (RP-

HPLC) system equipped with multiple wavelength detectors and a Zorbax-300SB C₁₈ column. A linear gradient of 5-95% acetonitrile (with 1% formic acid) over 30 min was used to elute peptide samples. Matrix-assisted laser desorption ionization time-of-flight (MALDI-TOF) mass spectra were obtained on a Bruker ultrafleXtreme™ MALDI-TOF/TOF mass spectrometer (Grant from National Science Foundation CHE-1625002) using α -cyano-4-hydroxy cinnamic acid (CHCA) as the ionizing matrix. Agilent 8453 UV-vis spectrometer with quartz cuvette (10 mm path length) was used to quantify peptide conjugate based on tyrosine absorbance at 280 nm. All microscopy measurements were performed using ImageJ software. Dynamic light scattering (DLS) was performed using a Brookhaven 90+ quasi-elastic light scattering spectrometer using with a disposable plastic cuvette.

3.4.2 Synthetic Scheme for Peptide Conjugate Azo/CD-(CH₃)₃-PEP_{Au}

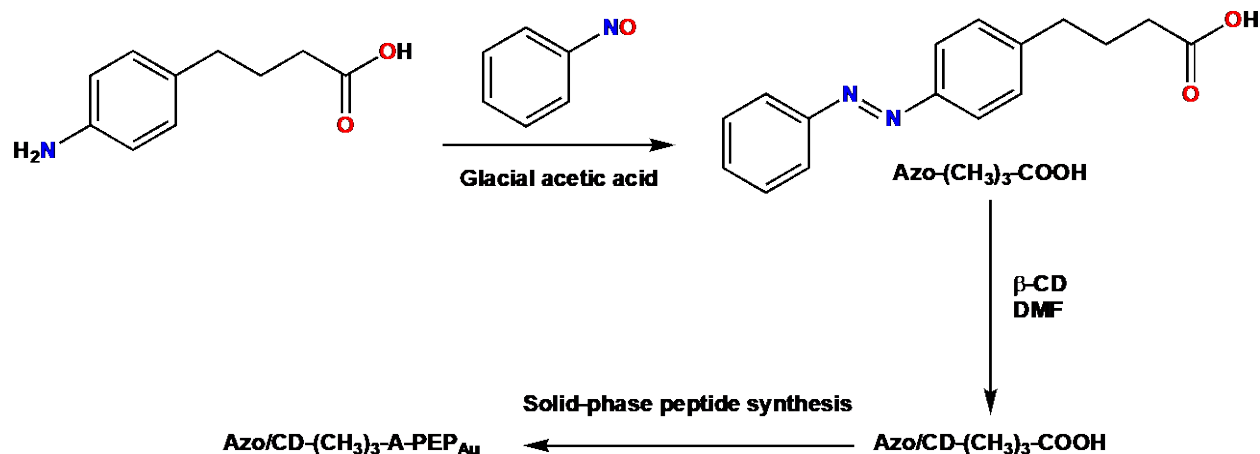
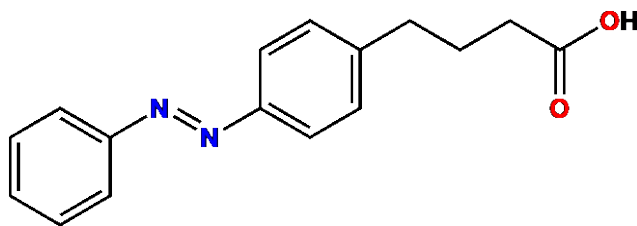


Figure 3.12. Synthetic scheme for peptide conjugate Azo/CD-(CH₃)₃-PEP_{Au}.

3.4.3 Synthesis of Azo-(CH₃)₃-COOH



4-(4-Aminophenyl)butanoic acid (Azo-(CH₃)₃-COOH, 1.5 mmol, 268.83 mg) was dissolved in 5 mL warm glacial acetic acid. Then the mixture was cooled to room temperature. To the cooled solution, nitrosobenzene (1.5 mmol, 160.7 mg) was added and the reaction vial was vortexed to yield a dark orange solution. After it was then left undisturbed for 12 hours, 5 mL water was added to precipitate an orange crude product (370 mg, 1.37 mmol, yield = 91.9%). The solid was re-dissolved in warm ethanol, cooled to room temperature, and re-precipitated with water. The solid was then filtered, oven-dried, and dried *in vacuo* (1.34 mmol, yield = 89.4%). ¹H-NMR spectrum of the product is shown in Figure 3.13, using d₆-DMSO (δ: 2.54 (¹H)) as solvent.

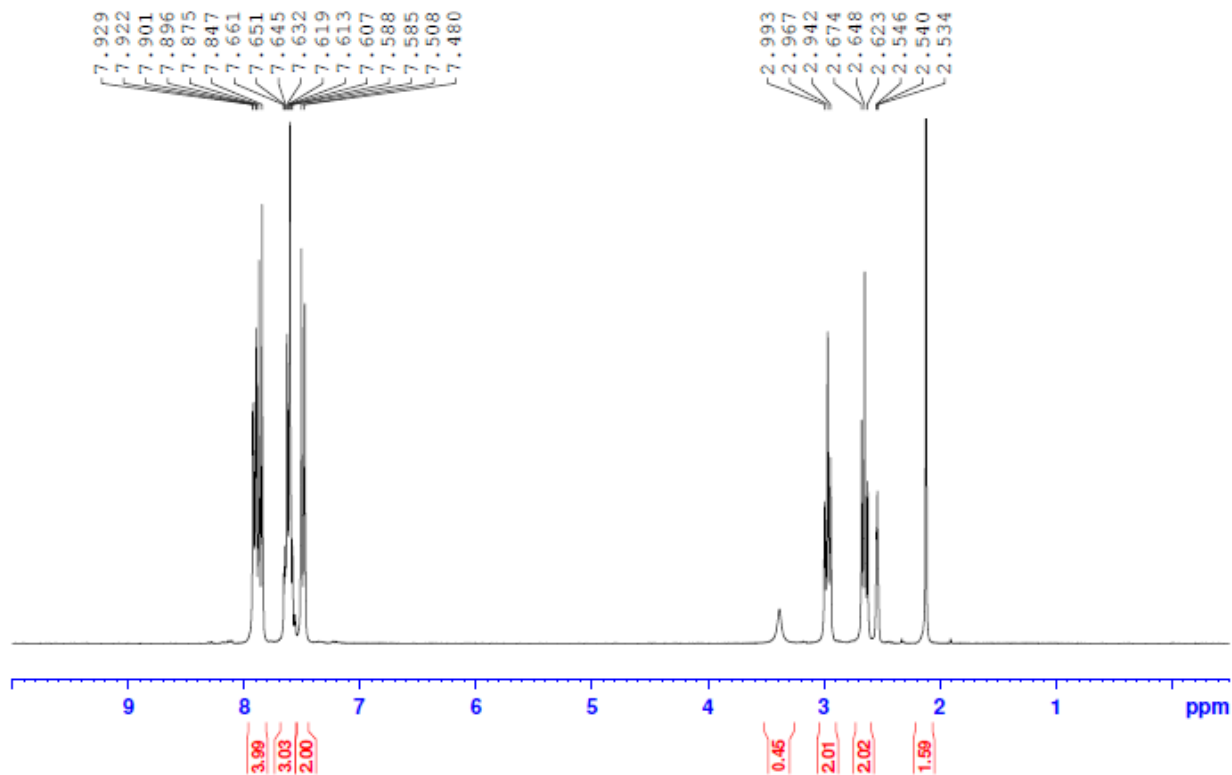


Figure 3.13. $^1\text{H-NMR}$ spectrum of 4-(4-Aminophenyl)butanoic acid.

3.4.4 Solid-Phase Peptide Synthesis of Azo/CD-(CH_3)₃-AA-PEP_{Au}

Azo/CD-(CH_3)₃-A-PEP_{Au} was synthesized following a similar procedure used to synthesize Azo-(CH_3)₃-A-PEP_{Au}. It is completed by manual microwave-assisted Fmoc solid phase methods using a CEM MARS microwave and NovaSyn TGA Fmoc-Phe resin (Milipore catalog number: 8560340001). The resin was first soaked in dimethylformamide (DMF) for 15 minutes and a 2 mL Fmoc-deprotection solution consisting of 20% 4-methylpiperidine in DMF was added. Fmoc deprotections were performed with a 1 min ramp to 75 °C, followed by a 2 min hold at that temperature with stirring. Thereafter, excess solution was drained using a filtration manifold and

washed with 2 mL DMF for three times. Thereafter, a 1.25 mL coupling solution consisting of 0.1 M HCTU (*O*-(1H-6-chlorobenzotriazole-1-yl)-1,1,3,3-tetramethyluronium hexafluorophosphate, 5 eq. to resin) in NMP (1-methyl-2-pyrrolidinone), vortexed with Fmoc-protected amino acid (5 eq. to resin) and DIEA (N,N-diisopropylethylamine, 7 eq. to resin), was added. Coupling reactions were then performed with a 1 min ramp to 75 °C, followed by a 5 min hold at that temperature while stirring. Thereafter, excess reagent was drained and the residue was washed with DMF for three time. This coupling-deprotection cycle was repeated for every amino acid. Proline and adjacent amino acids were coupled twice to ensure complete reaction of secondary amide group. N-terminus was capped with a 0.1 M DMF solution of equimolar of β -CD and Azo-(CH₃)₃-COOH of the same volume as the coupling solution, 1.25 mL, which was incubated at 50 °C overnight before coupling. The resin was then washed with DMF, methylene chloride, and methanol. The peptide was then cleaved from resin using a 2 mL cleavage cocktail (95/2.5/2.5 trifluoroacetic acid/triisopropylsilane/H₂O). Crude peptide was precipitated by adding the resin-cleavage cocktail to cold Et₂O and washed by Et₂O for two times. The peptide was then dissolved in 1/1 acetonitrile/water, and stored at 4 °C, before further purified with RP-HPLC.

3.4.5 Molecular Structure of Azo-(CH₃)₃-A-PEP_{Au}

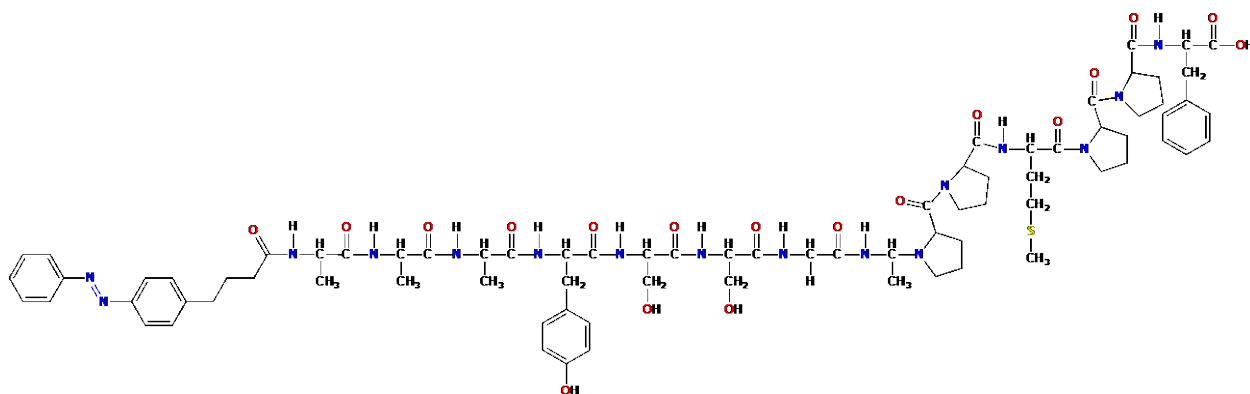


Figure 3.14. Molecular Structure of Azo-(CH₃)₃-A-PEP_{Au}.

3.4.6 Molecular Structure of β -Cyclodextrin (β -CD)

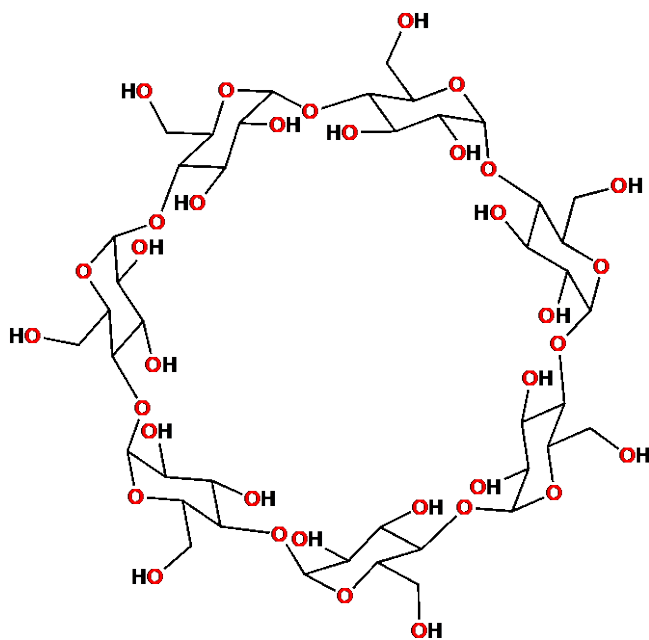


Figure 3.15. Molecular structure of β -cyclodextrin (β -CD).

3.4.7 Assembly of Peptide Conjugate Azo/CD-(CH₃)₃-A-PEP_{Au} in HEPES Buffer and UV Irradiation

20 nmol of Azo/CD-(CH₃)₃-A-PEP_{Au} was dissolved in 200 μL 0.1 M HEPES buffer in a plastic vial either in the presence or absence of saturated β-CD. The vial was sonicated for 5 min to ensure complete solubilization, and the left undisturbed for 25 min. UV light irradiation was conducted using a Continuum Minilite Nd:YAG 1080 laser operated at 355 nm. The sample was loaded in a quartz cuvette with a path length of 10 mm and irradiated with UV laser at 355 nm for 5 min, 30 min or 2 h. The solution was then immediately spotted on a TEM for imaging.

3.4.8 Synthesis of NPs Directed by Azo/CD-(CH₃)₃-A-PEP_{Au} and UV Irradiation

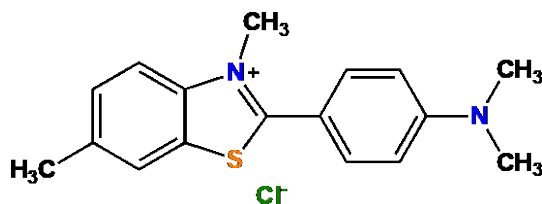
NP superstructures were prepared using established methods with minor modifications.²⁷⁻
²⁸ Briefly, 20 nmol of lyophilized Azo/CD-(CH₃)₃-A-PEP_{Au} was dissolved in 200 μL 0.1 M HEPES buffer saturated with β-CD. Next, the sample was sonicated for 5 min, before it was left undisturbed at room temperature for 25 min. Toward the end of the 25 min incubation, a gold precursor solution was freshly prepared by vortexing 0.1 M HAuCl₄ in H₂O and 1 M triethylammonium acetate (TEAA) buffer for 1 min. After the 25 min, 2 μL of the gold precursor solution was added to the peptide buffer solution. Upon observing a black precipitate, the reaction vial was vortexed and left at room temperature for 18 hours. The sample was then centrifuged (5 krpm, 10 min) and re-dispersed in 200 μL 0.1 M HEPES buffer saturated with β-CD. For UV irradiation, the sample was loaded in a quartz cuvette with a path length of 10 mm and was then irradiated with UV laser at 355 nm.

3.4.9 Transmission Electron Microscopy (TEM)

TEM imaging was performed on a FEI Morgagni 268 operated at 80 kV and equipped with an advanced microscopy techniques (AMT) side mount charge-coupled device (CCD) camera system. TEM samples were prepared by drop-casting 5 μL of sample onto a 3 mm diameter copper grid with Formvar coating. After 5 min, excess solution was removed by filter paper and the sample was air-dried for 1 min. And 5 μL of H_2O was applied to the grid to remove excess solvent. After 1 min, the H_2O was removed, and the grid was left to air dry for 5 min. Negatively stained TEM samples were prepared by adding 5 μL 2% uranyl acetate solution to the grid after it was air dried for 5 min. Next, after 5 min, the excess staining solution was removed by filter paper and the grid was left to air dry for 5 min.

3.4.10 Fluorescence Studies

3.4.10.1 Molecular Structure of Thioflavin T (ThT)



3.4.10.2 ThT Fluorescence Studies for Peptide Assemblies

ThT fluorescence were recorded on a Horiba Jobin Yvon (HJY) Fluoromax 3 spectrofluorimeter using a quartz cuvette. Each sample was allowed to incubate with ThT (5 μM)

overnight and was excited at 450 nm while emission was recorded from 460 to 600 nm at room temperature in a quartz cuvette.

3.4.11 Supporting Figures

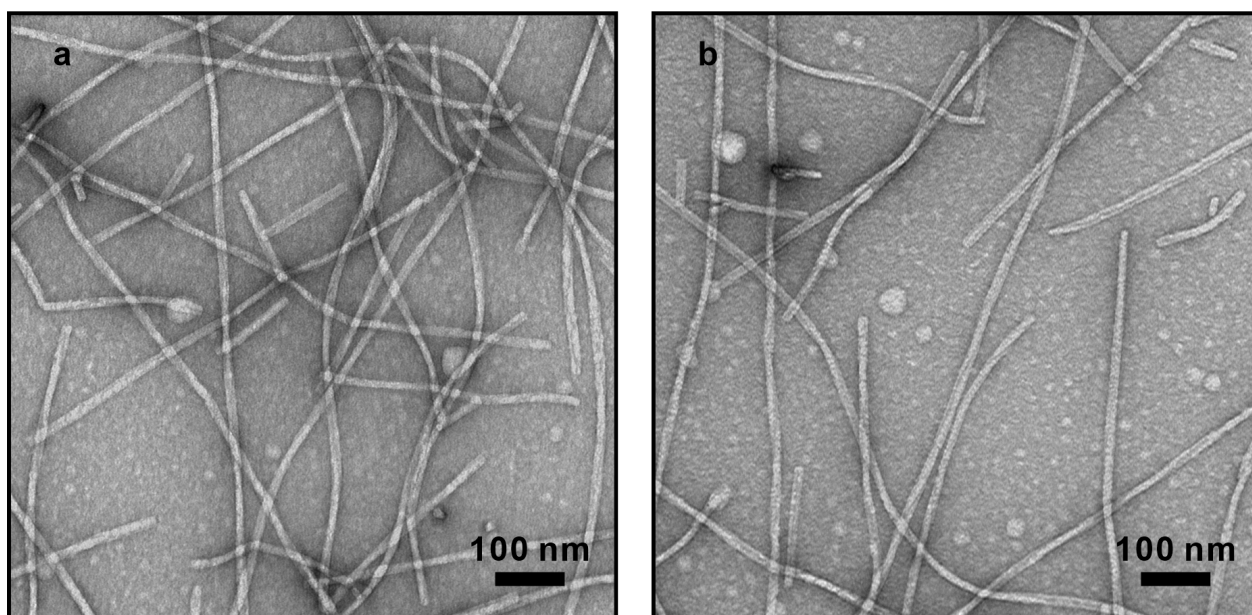


Figure 3.16. Negatively stained TEM image of assembly of Azo-(CH₃)₃-A-PEP_{Au} in 0.1 M HEPES buffer at 2 h.

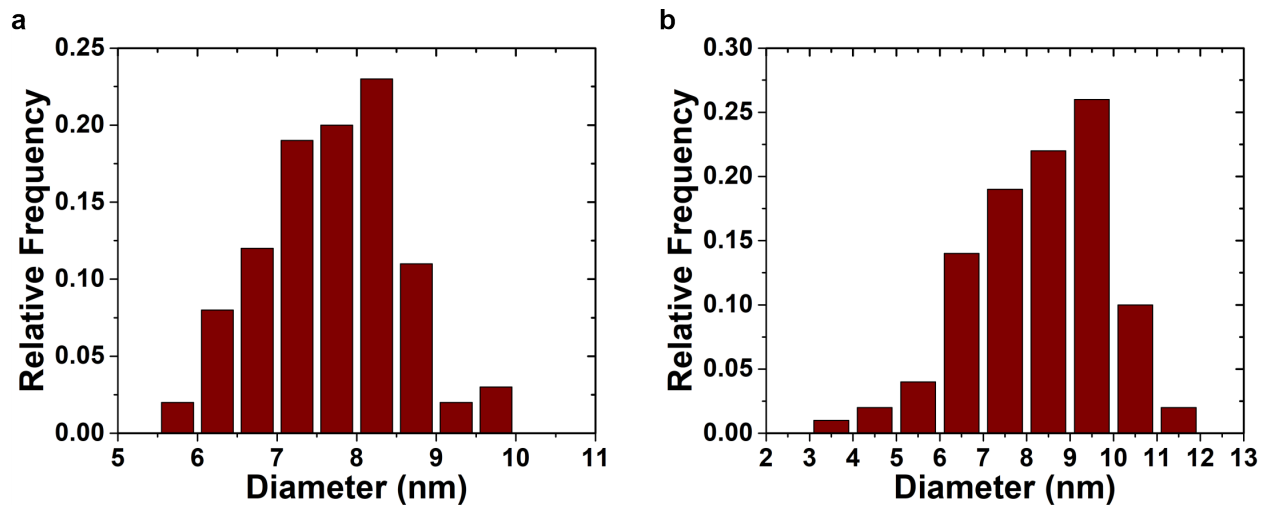


Figure 3.17. Diameter distribution (based on 100 counts) of NPs directed by conjugate Azo/CD-(CH₃)₃-A-PEP_{Au} (a) before and (b) after UV irradiation for 30 min. The average diameters before and after UV irradiation are 7.7 ± 0.9 nm and 8.3 ± 1.5 nm, respectively.

4.0 Investigating the Stability of Peptide-based Gold Nanoparticle Single Helices

This work is the subject of a manuscript in preparation.

We have been able to construct a wide variety of structurally-complex nanoparticle superstructures using our peptide-based methodology. Some of these superstructures exhibit NIR optical properties that could be exploited for biological applications and others exhibit unusual plasmonic chiroptical properties that are of interest for sensing and the creation of negative index materials. It is critical that we study and understand the stability of these superstructures in various environments and examine factors that influence their structural robustness. In this study, I examine the stability of single-helical nanoparticle superstructures. I evaluate their stability at different temperatures and in the presence of urea, a denaturant, and proteinase K (ProK), an enzyme that digests peptides. I demonstrate that structural stability positively correlates with increasing size of the component nanoparticles within the superstructures.

4.1 Introduction

Chiral and helical NP superstructures are a novel class of material because they have wide variety of potential applications in chemical sensing^{61,179} and catalysis¹⁸⁰ and are a promising class of metamaterials.¹⁸¹⁻¹⁸⁴ We focus our attention on the peptide-based single helical gold nanoparticle (AuNP) superstructures, which exhibit strong plasmonic chiroptical response.^{25,27-28} We have established and developed this peptide-based methodology, which is very powerful and versatile for synthesizing and assembling NPs. By designing the peptide conjugates and fine-

tuning reaction conditions, we were able to systematically modify the superstructure morphologies,¹⁰⁵ control the pitch of helical superstructures,²⁸ and control the size and shape of constituent NPs.^{28,110}

Our prior efforts focused on carefully designing and tuning the molecular structures of peptide conjugates, and subsequently controlling the morphology, metrics and properties of the superstructure. However, we have not rigorously examined the stability of the NP superstructures. The structural integrity and stability are not only important for application of these assembled NP superstructures, but also constitute a fundamental property of the material. In a typical synthesis, a specific peptide conjugate and Au precursor are incubated in the presence of a reducing reagent. The peptide conjugates associate with *in situ* formed AuNPs and incorporate them into an assembled superstructure. As the reaction proceeds, Au NPs grow in size and their optical signal intensifies. In the final superstructures, individual NPs are embedded and anchored onto the peptide scaffold. We reason that further growth of the individual NPs would lead to intergrowth and fusing of the NPs, which could improve structural stability and prevent disassembly under conditions that promote peptide conjugate disassembly. For the single-helical NP superstructures, in particular, a more robust and stable fused helical structure, rather than a superstructure comprising discrete particles, could exhibit a stronger chiroptical signal and could be sufficiently robust for more wide-spread applications.¹⁸⁴

Here, we take a first step toward increasing the stability of single-helical Au NP superstructures by increasing the constituent NP sizes, with the goal of ultimately forming a fused single helix (Figure 4.1). We study and examine the stability of these single-helical superstructures with increasing NP sizes under three different environments: elevated temperature, and in the presence of two peptide denaturants, proteinase K (ProK) and urea. By gradually increasing the

size of the constituent NPs, the single-helical superstructures become more stable under these conditions.

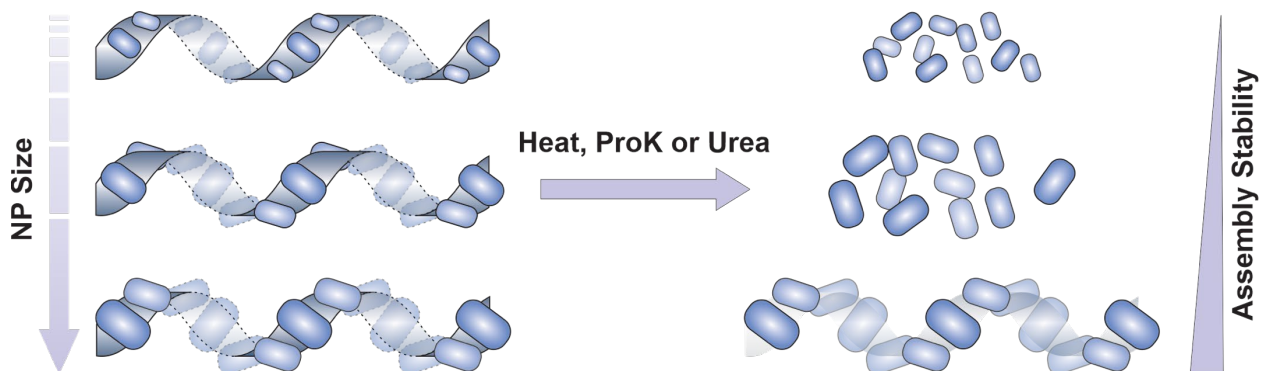


Figure 4.1. Schematic representation of increasing the stability of peptide-based Au NP single helices against heat, urea or ProK by increasing the constituent NP sizes.

4.2 Results and Discussion

We synthesized the single-helical AuNP superstructures using $C_{18}-(PEP_{Au}^{M-ox})_2$ (PEP_{Au} : NH_2 -AYSSGAPPMPF; M-ox indicates oxidized methionine residue), according to our previously reported methods.²⁷⁻²⁸ Briefly, purified and lyophilized peptide conjugates were dissolved in HEPES (4-(2-hydroxyethyl)-1-piperazineethanesulfonic acid) buffer (pH = 7.3) before an aliquot of $HAuCl_4$ precursor was added to the reaction mixture. The resulting AuNP single helices were purified via centrifugation and imaged with transmission electron microscopy (TEM). Au NP single helices with larger particle sizes were obtained by adding growth solution of $HAuCl_4$ and hydroquinone according to a previously reported method (See Supporting Information for experimental details).¹⁰⁶ In the syntheses of AuNP superstructures, we noticed the presence of a large amount of peptide assemblies without any AuNP attached. To eliminate the interference of these peptide assemblies, as-synthesized samples were centrifuged to yield pure

AuNP single helices. AuNP single helices comprising particles of three different sizes were obtained (Table 4.1 and Figure 4.2), and they are hereafter referred to as **small**, **medium** and **large** AuNP single helices, respectively. It should be noted that the shape of the NP is oblong instead of spherical. We then proceeded to examine the stability of this family of AuNP single helices under three different conditions: 1) elevated temperature, 2) presence of proteinase K (ProK) and 3) presence of urea.

Table 4.1. Metrics of Au NP single helices comprising of three different NP sizes.

Au NP single helices	Small	Medium	Large
NP length (nm)	13.5 ± 3.5	15.5 ± 4.1	17.9 ± 5.2
NP width (nm)	7.8 ± 2.4	9.5 ± 3.2	11.0 ± 3.7

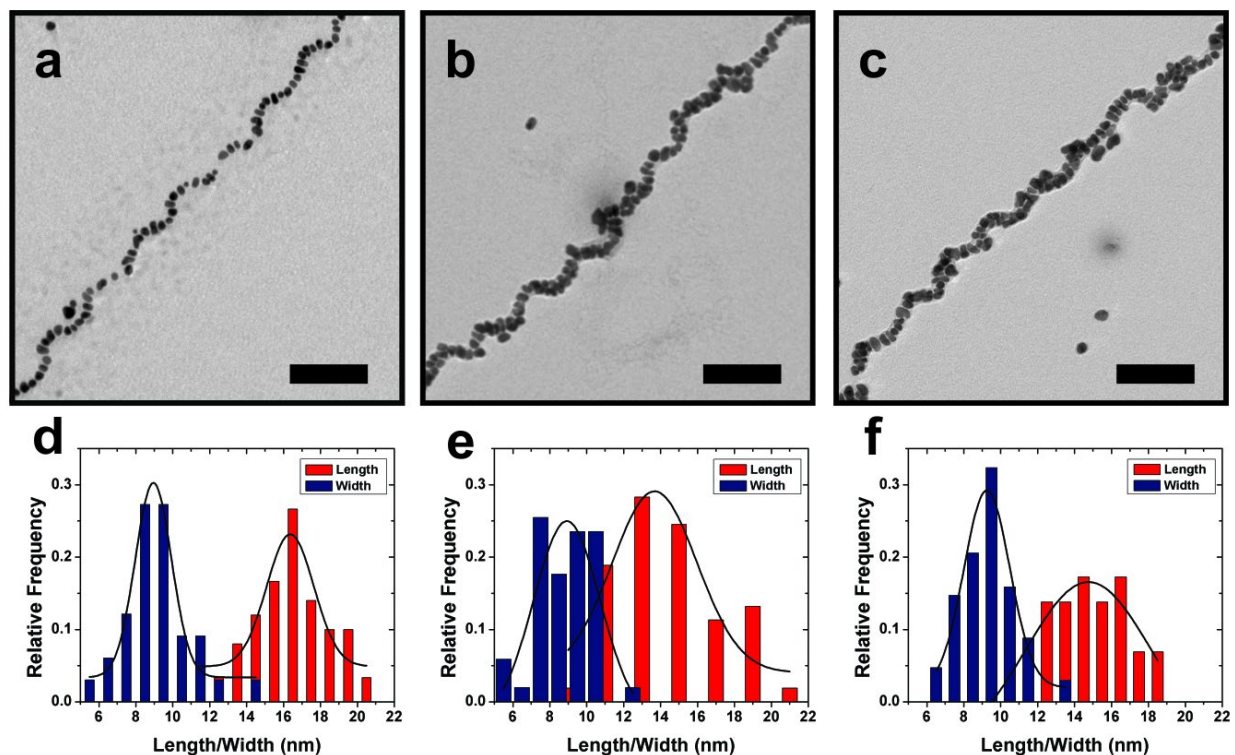


Figure 4.2. Characterization of AuNP single helices of increasing NP sizes. TEM images and metrics measurements of small (a, d), medium (b, e), and large (c, f) Au NP single helices. Scale bar, 50 nm. Measurements are based on at least 100 counts.

4.2.1 Elevated Temperature

As previously described, the peptide conjugate assembly serves as an underlying scaffold onto which Au NPs are assembled, and its structure dictates the structure of the NP assembly. It is therefore very important to examine the stability of the peptide scaffold before we begin to study the stability of AuNP superstructures. The peptide itself assembles into a coiled-ribbon morphology at room temperature in HEPES buffer.²⁷ Peptide conjugates were dissolved in HEPES buffer and allowed to assemble. Samples were incubated for 5 min at every 5 °C from 25 °C to 90 °C. Negatively-stained TEM images show that the peptide fibers gradually disassemble as the temperature increases from 25 °C to 90 °C. Specifically, the peptide assembly remains as a one-dimensional fiber below 40 °C and gradually transitions into amorphous aggregates as the temperature reaches above 50 °C (Figure 4.3).

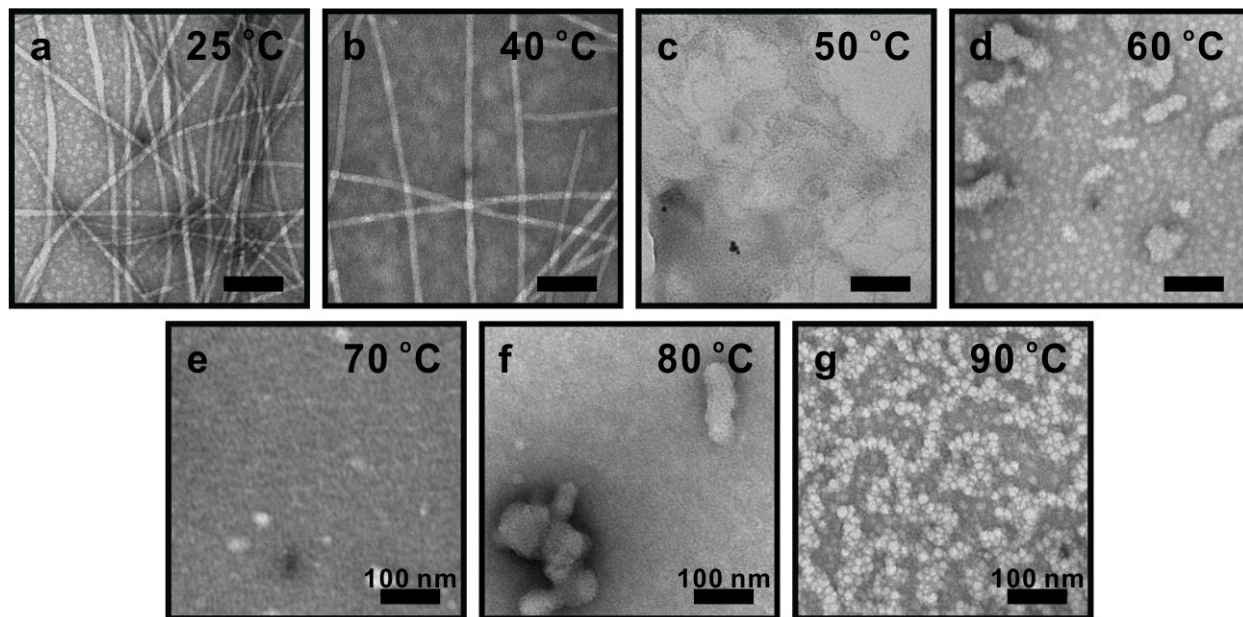


Figure 4.3. Negatively stained TEM images of assemblies of conjugate $C_{18}-(PEP_{Au}^{M-ox})_2$ in 0.1 M HEPES buffer as temperature increases from 25 °C to 90 °C.

To confirm this observation, circular dichroism (CD) spectroscopy, which is commonly used to characterize the secondary structure of peptides and proteins, was employed to monitor the fiber melting process. The intensity of the CD signal at 208 nm was plotted against the temperature, and the signal decreases as the temperature is above 40 °C, indicating disruption of the ordered secondary structure (Figure 4.4).¹⁸⁵ We further used a fluorescent dye thioflavin T (ThT), which is found to bind to amyloid fibers,¹⁸⁶⁻¹⁸⁸ as an indicator for assembly morphology. When excited at 450 nm, strong emission is observed at 485 nm when ThT binds to β -sheet structure, whereas emission diminishes when no β -sheet structure is present. Despite the fact that Au NPs could potentially quench the fluorescence of some dyes in close range with themselves, the results from this control experiments suggest otherwise that, in our case, ThT fluorescence of $C_{18}-(PEP_{Au}^{M-ox})_2$ was not quenched even in the presence of Au NPs, and we can use ThT to monitor Au NP single helices. We then examined the fluorescence of $C_{18}-(PEP_{Au}^{M-ox})_2$ conjugates as the temperature increases. A drastic decrease of the fluorescence signal of peptide fiber assemblies can be observed at around 40 °C, which follows the same trend as observed in TEM images and CD measurements (Figure 4.5).

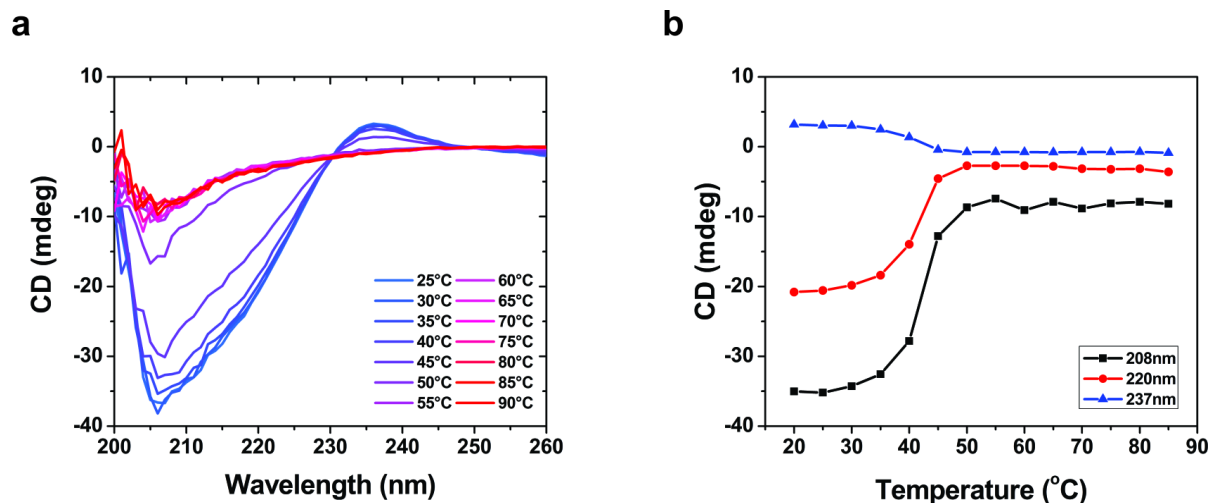


Figure 4.4. (a) CD spectra of assemblies of conjugate $C_{18}-(PEP_{Au}^{M-ox})_2$ in 0.1 M HEPES buffer as temperature increases from 25 °C to 90 °C. (b) CD intensity at 208 nm (black), 220 nm (red), and 237 nm (blue) as temperature increases from from 25 °C to 90 °C.

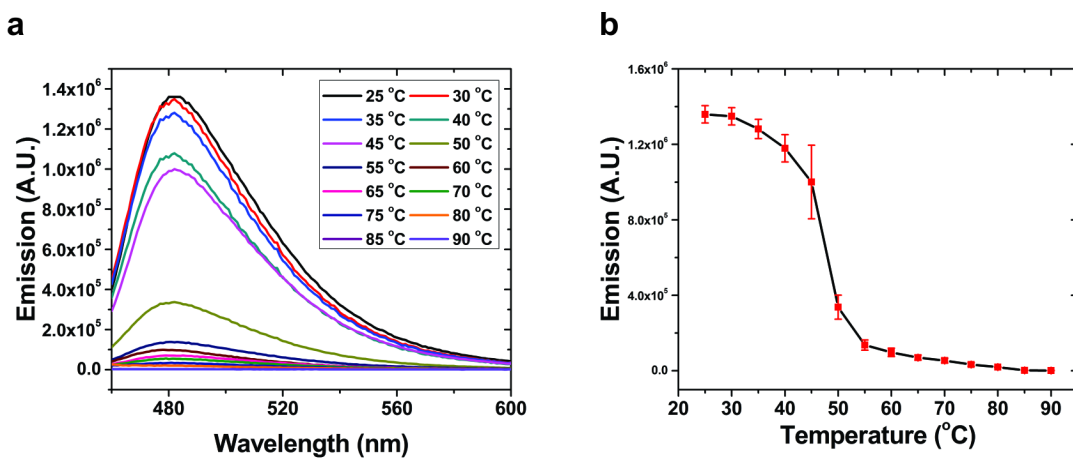


Figure 4.5. (a) ThT emissions upon excitation at 450 nm as a function of temperature. (b) Emission intensity at 485 nm as a function of temperature.

We next proceeded to investigate the AuNP single helices at elevated temperatures. In all three cases, the AuNP single helices remained intact at low temperatures (below 40 °C) and disassembled at high temperatures (above 70 °C). Interestingly, the temperature at which the AuNP single helices start to disassemble increases as the size of the NP increases. Specifically, from TEM images, small, medium and large Au NP single helices disassemble at different temperatures,

around 40 °C, 50 °C and 60 °C, respectively. To confirm the findings in TEM images, we performed melting experiments monitored with CD spectroscopy (Figure 4.6 and Figure 4.7). For an as-synthesized sample (without any further treatment), the AuNP single helices exhibit a plasmonic chiroptical signal at around 560 nm (Figure 4.7a) due to the chiral arrangement of AuNPs along the peptide fiber assembly. A closer look at the CD melting profiles of these samples confirmed the findings observed in TEM images. For small single helices, a transition from single-helical assembly to disassembled NPs can be observed when the temperature increases from 40 °C to 50 °C (Figure 4.6e). For medium and large single helices, the transition takes place when temperature increases from 50 °C to 60 °C (Figure 4.6j) and from 60 °C to 70 °C (Figure 4.6o), respectively. Although the superstructures disassembled completely at high temperature, increasing the size of the constituent NPs resulted in shifting the melting temperature higher, indicating the superstructure becomes more stable.

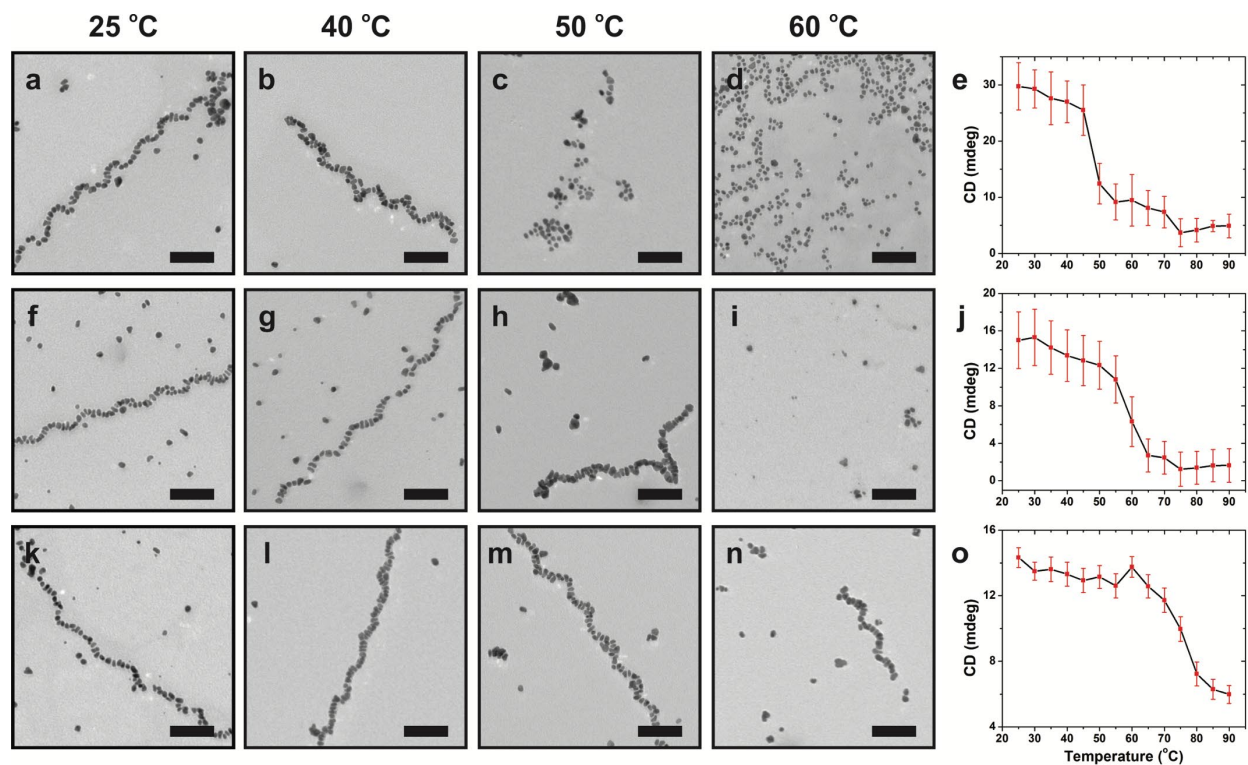


Figure 4.6. Effect of temperature on Au NP single helices. TEM images and CD intensity at 560 nm of small (top row), medium (middle row), and large (bottom) Au NP single helices at different temperatures. Scale bar = 100 nm. CD intensity data were collected using three parallel measurements.

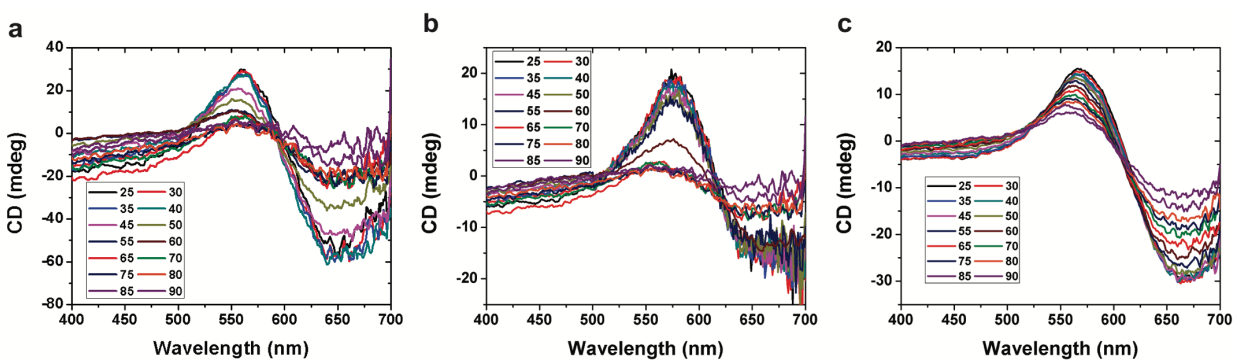


Figure 4.7. CD spectra of small (a), medium (b), and large (c) Au NP single helices when temperatures were increased from 25 °C to 90 °C.

4.2.2 Treatment with Proteinase K (ProK)

ProK is a non-specific, broad-spectrum protease, which is commonly used to digest peptides or proteins.¹⁸⁹ We have previously succeeded in using ProK to digest spherical AuNP superstructures.²⁴ To first determine a suitable concentration for the digestion experiment, lyophilized C₁₈-(PEP_{Au}^{M-ox})₂ peptide conjugates were dissolved in 0.1 M HEPES buffer and incubated for 30 min at 37 °C. At this temperature, peptide fibers remain intact as shown in the previous section and ProK is active. The peptide fibers were then incubated in the presence of ProK with concentrations ranging from 0.02 to 0.8 mg/mL at 37 °C. The final concentrations for each component were as follows: 20 μM peptide conjugate, 0.1 M HEPES, 5 μM ThT, and 0.02 to 0.8 mg/mL ProK. Results from ThT fluorescence (Figure 4.8) and TEM imaging (Figure 4.9) showed that peptide fibers were intact after being incubated at the lower ProK concentration, 0.02 mg/mL, for up to 18 hrs, but were digested at the higher ProK concentrations, 0.1, 0.2, 0.4 and 0.8 mg/mL, in less than 2 min. After screening a series of ProK of different concentrations, two sets of concentrations of ProK, 0.02 mg/mL and 0.4 mg/mL, were selected to be used in ProK digestion experiments: these two concentrations represent two conditions in which peptide conjugate would stay intact (0.02 mg/mL) and disassemble (0.4 mg/mL).

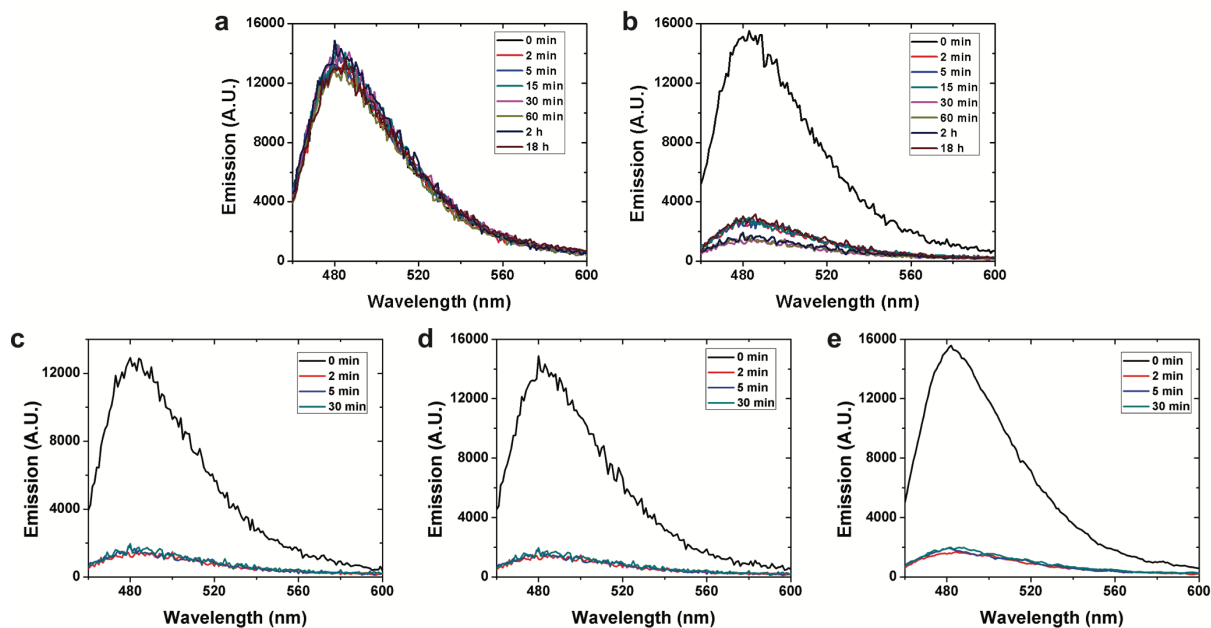


Figure 4.8. ThT emission spectra (excited at 450 nm) recorded at different time points when incubated with $C_{18}-(PEP_{Au}^{M-ox})_2$ (20 nmol) in 0.1 M HEPES buffer at 37 °C in the presence of different concentrations of ProK: (a) 0.02 mg/mL, (b) 0.1 mg/mL, (c) 0.2 mg/mL, (d) 0.4 mg/mL, (e) 0.8 mg/mL.

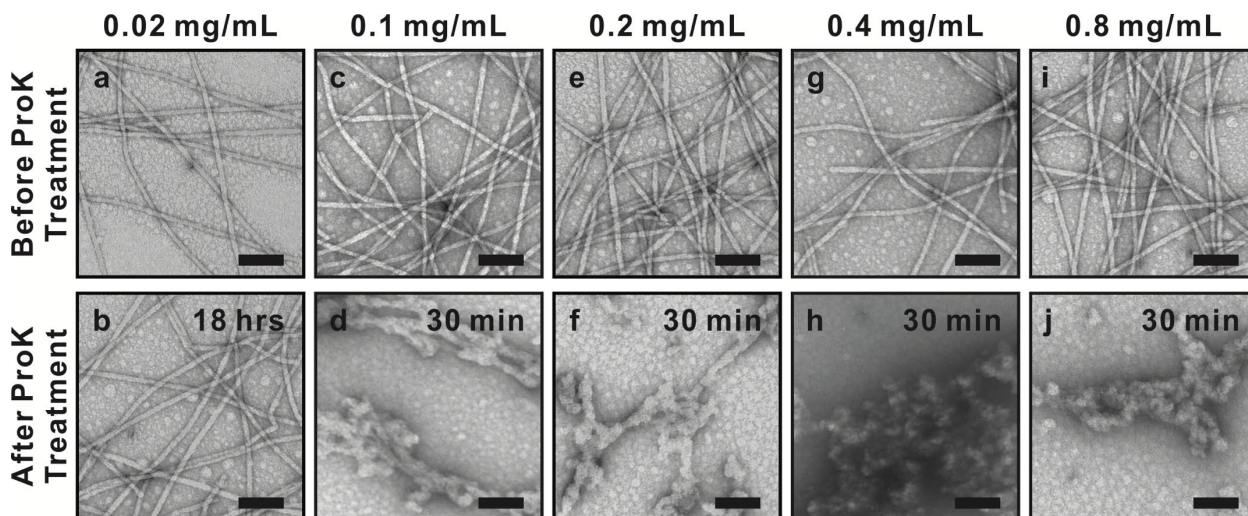


Figure 4.9. Negatively stained TEM images of $C_{18}-(PEP_{Au}^{M-ox})_2$ (20 nmol) assemblies before (top row) and after (bottom row) ProK was added. ProK concentrations: (a, b) 0.02 mg/mL, (c, d) 0.1 mg/mL, (e, f) 0.2 mg/mL, (g, h) 0.4 mg/mL, (i, j) 0.8 mg/mL. For 0.02 mg/mL ProK, TEM images were taken after 18 hours incubation; for all other concentrations, TEM images were taken after 30 min incubation. Scale bar = 100 nm.

Next, we examined AuNP single helices in the presence of ProK. As-synthesized small, medium, and large AuNP single helices were incubated with 0.02 or 0.4 mg/mL ProK at 37 °C. For the lower concentration (0.02 mg/mL) of ProK, no obvious changes were observed in morphology for small, medium and large single helices after incubation with ProK for up to 18 hrs (Figure 4.11). At higher ProK concentration, 0.4 mg/mL, after incubating for 30 min, shorter AuNP single helices and discrete NPs were observed for small and medium single helices samples, as shown in Figure 4.10d and Figure 4.10e, respectively. Interestingly, large AuNP single helices remained intact longer after treatment with ProK, as shown in Figure 4.10f. To confirm that the peptide fiber scaffold was digested by ProK, we negatively stained TEM samples with 2% uranyl acetate. For as-synthesized AuNP single helices, a clear fiber backbone could be observed (Figure 4.12). However, for large AuNP single helices after incubation with ProK, we cannot clearly observe the fiber backbone (Figure 4.12).

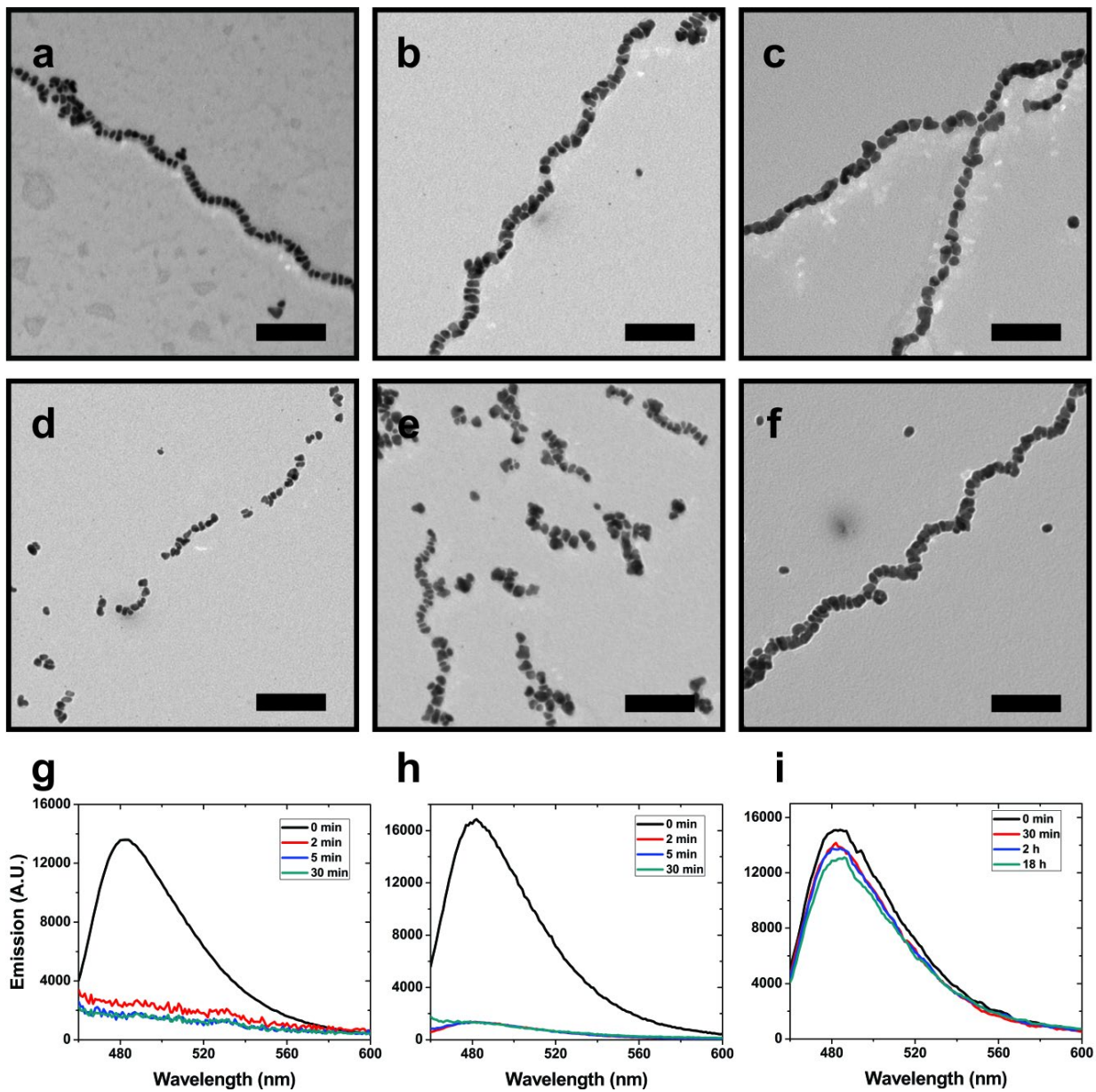


Figure 4.10. TEM images and ThT fluorescence spectra of small (left column), medium (middle column), and large (right column) Au NP single helices before (top row) and after (middle row) mixing with ProK. Scale bar = 100 nm.

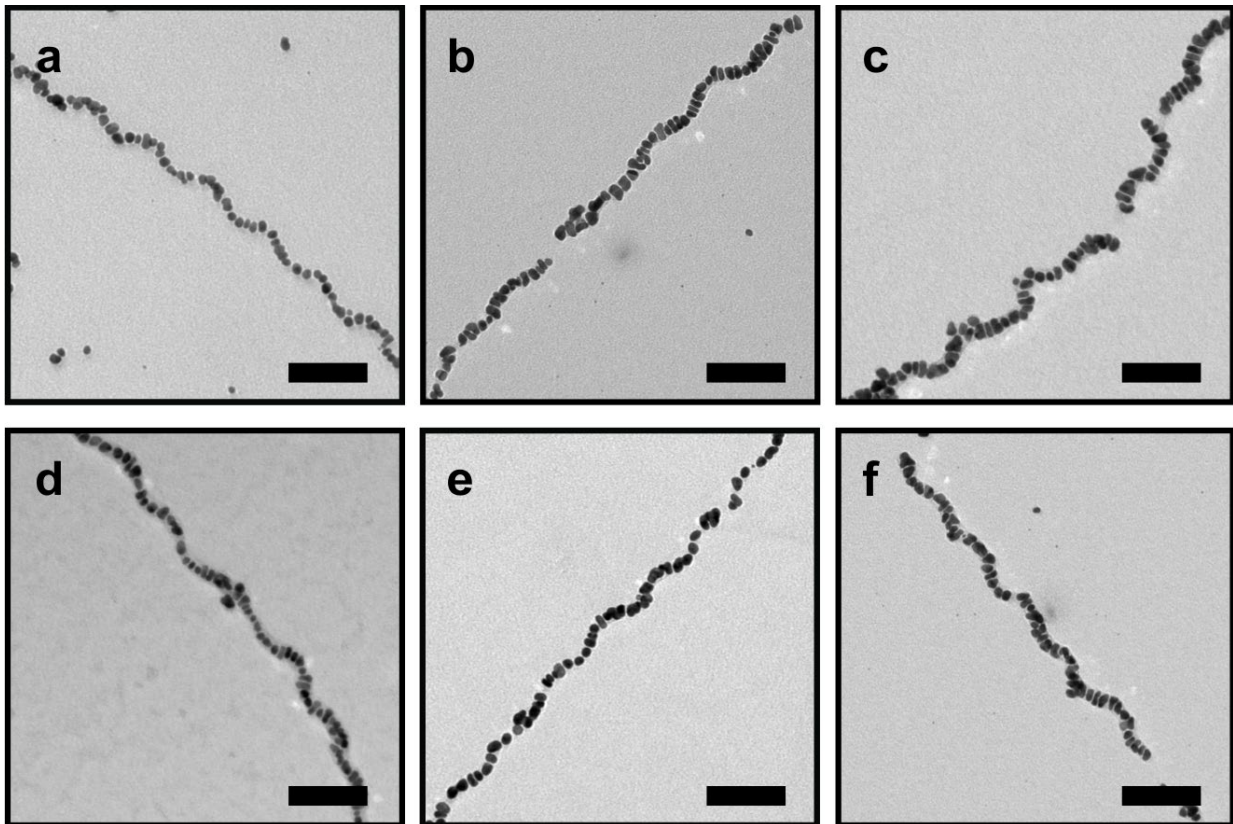


Figure 4.11. TEM images of small (a, d), medium (b, e), and large (c, f) Au NP single helices before (top row) and after (bottom row) incubating with 0.02 mg/mL ProK. Scale bar = 100 nm.

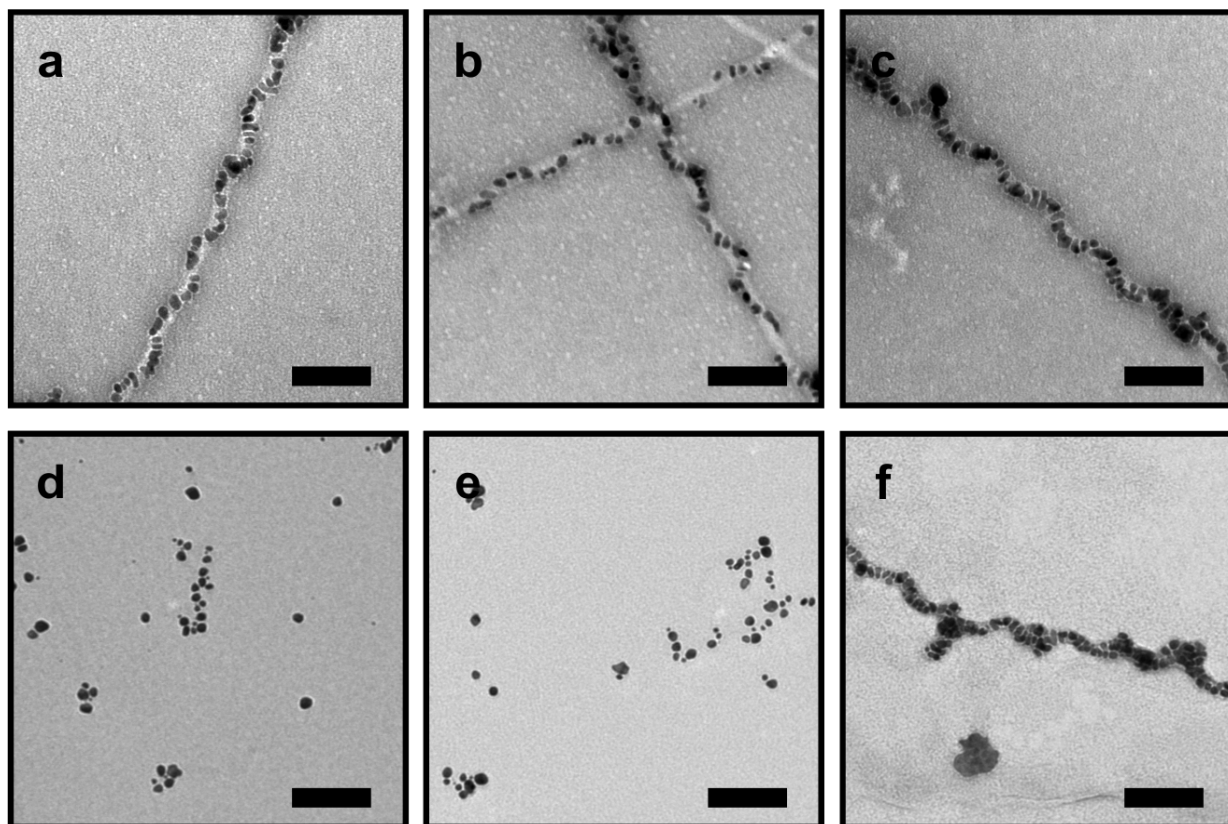


Figure 4.12. Negatively stained TEM images of small (a, d), medium (b, e), and large (c, f) Au NP single helices before (top row) and after (bottom row) mixing with ProK. Scale bar = 100 nm.

We proceeded to examine the small, medium and large AuNP single helices in the presence of ThT dye and ProK. When the Au NP single helices samples were incubated with 0.4 mg/mL ProK, ThT emission decreased drastically and fairly quickly (within 30 min) for small (Figure 4.10g), and medium (Figure 4.10h) AuNP single helices, indicating digestion of the peptide scaffold. For the large AuNP single helices, ThT fluorescence signal decreased slightly (Figure 4.10i). This result shows that helices with large constituent NPs can maintain their structure in the presence of ProK treatment. Further, the data show that the fibers remain intact, indicating that the larger Au NPs provide protection against ProK digestion.

4.2.3 Treatment with Urea

As shown in the previous section, AuNP single helices were able to maintain their stability (to a certain degree) when the size of the constituent NPs increased. I chose to study urea as a non-destructive denaturant for peptides and proteins. Urea denatures peptides and proteins via its strong H-bonding interaction with amino acid residues, thus it may serve to disassemble peptide backbone.

To find an optimal concentration of urea for testing Au NP single helices stability, we first tested the stability of the peptide assembly in the presence of a range of urea concentrations. Peptide conjugates were first incubated in HEPES buffer in the presence of ThT as a β -sheet indicator for at least one day to allow for complete one-dimensional assembly. Different concentrations of urea were then added to the assemblies. The final concentrations for each component were as follows: 20 μ M peptide conjugate, 0.1 M HEPES, 5 μ M ThT, and 0.005 to 10 M urea. From the fluorescence responses of ThT upon mixing urea with the peptide conjugate assemblies (Figure 4.13), it is clear that urea concentrations higher than 2 M led to loss of ThT fluorescence, whereas urea concentrations lower than 2 M caused ThT fluorescence signal to decrease to a certain degree. TEM images fiber assemblies were consistent with the data from the ThT studies: amorphous aggregates were observed for samples with higher urea concentration (2 M or higher, Figure 4.14), and 1-D fibers were observed for samples with lower concentrations of urea (1M or lower, Figure 4.14). We decided to focus on three different concentrations of urea: 0.5 M, 1 M, and 2 M. At these concentrations, peptide fibers would remain intact or disassemble, and we could examine the stability of Au NP single helices as a function of urea concentration.

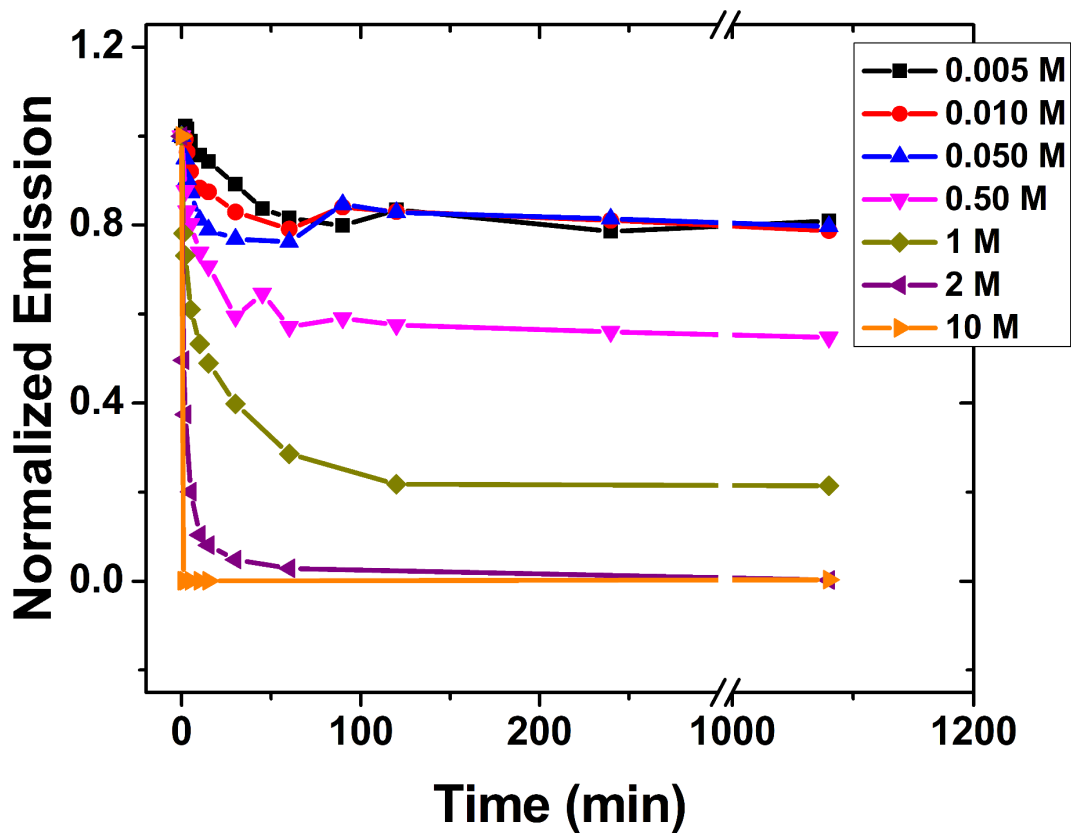


Figure 4.13. Normalized emission at 485 nm of ThT in the presence of $C_{18}-(PEP_{Au}^{M-ox})_2$ and different concentrations of urea as a function of time.

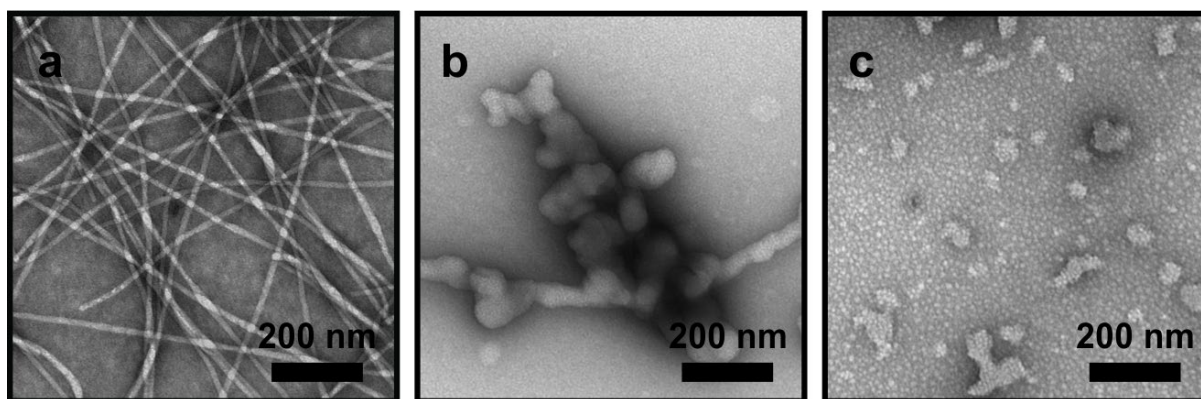


Figure 4.14. Negatively stained TEM images of $C_{18}-(PEP_{Au}^{ox})_2$ assembly after incubating with urea of different concentrations. Urea concentrations: (a) 0.5 M, (b) 1 M, and (c) 2 M.

We then studied the stability of small, medium, and large Au NP single helices in the presence of urea at the three different concentrations. Upon incubating with urea at the selected concentrations (0.5 M, 1 M, and 2 M), small, medium, and large Au NP single helices exhibited different responses to urea. Specifically, as shown in the TEM images in Figure 4.15, small helices were more likely to disassemble when urea concentrations increased from 0.5 M to 2 M: single helices were observable at 0.5 M urea (Figure 4.15a); at 1 M urea, segmentation of single helices was observed (Figure 4.15b); at the highest concentration of urea, 2 M, only discrete NPs were present in TEM images (Figure 4.15c). For medium helices, the segmentation of helices occurred at higher urea concentration (e-g). For large helices, more complete helices could be observed at higher urea concentrations such as 1 M or 2 M (Figure 4.15i-k). The TEM images revealed that increasing the size of constituent NPs leads to more robust single helices. To further examine the process, each sample was also monitored with ThT fluorescence using the method described previously (Figure 4.16). For all samples, ThT emissions decreased instantly upon addition of urea, indicating denaturation of the peptide fibers. However, the decrease in ThT emission varied for small, medium, and large helices, as well as for different urea concentrations. For example, for small helices, the ThT emission decreased significantly at 2 M urea after 2 h incubation (Figure 4.15d). The observation suggests that the majority of the helices disassembled into discrete NPs, as shown in the corresponding TEM images (Figure 4.15c). As the size of the NPs increases, the degree to which ThT emission decreases becomes smaller (Figure 4.15h and Figure 4.15l), suggesting the single helices with larger NP sizes are in some way protected from denaturation by urea. To highlight this difference, at 2 M urea, emission for large helices was recorded to be

around 50 % of the starting intensity; however, for small helices, the ThT fluorescence decreased almost completely.

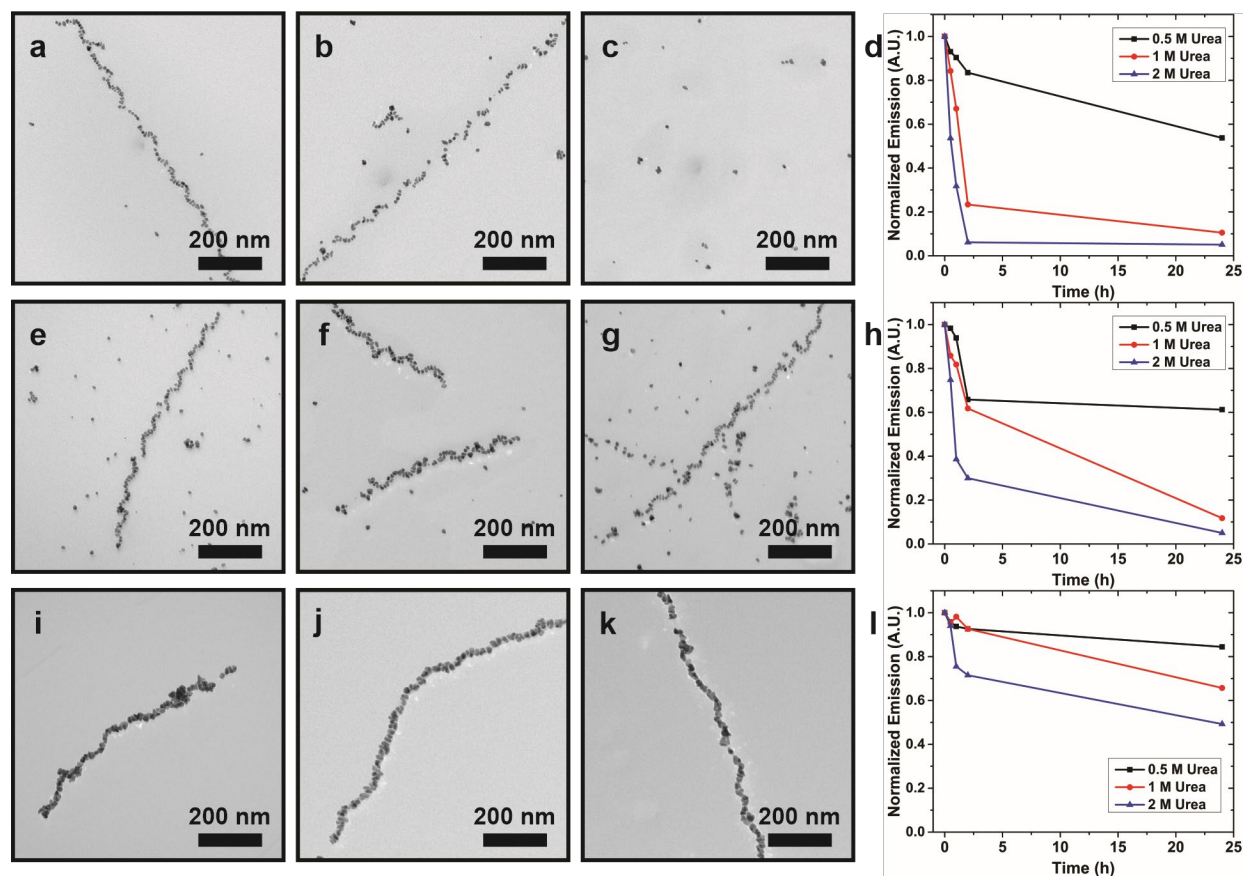


Figure 4.15. Effects of different concentrations of urea on Au NP single helices of increasing constituent NP sizes. TEM images of small (a, b, c), medium (e, f, g), and large (i, j, k) Au NP single helices after incubating with different urea concentrations (a, e, i: 0.5 M. b, f, j: 1 M. c, g, k: 2 M) for 1 d. Normalized ThT emissions for small (d), medium (h), and large (l) Au NP single helices at 480 nm recorded for up to 1 d (urea concentrations: black, 0.5 M; red, 1 M; blue, 2 M). See Fig. S12 for full ThT emission spectra.

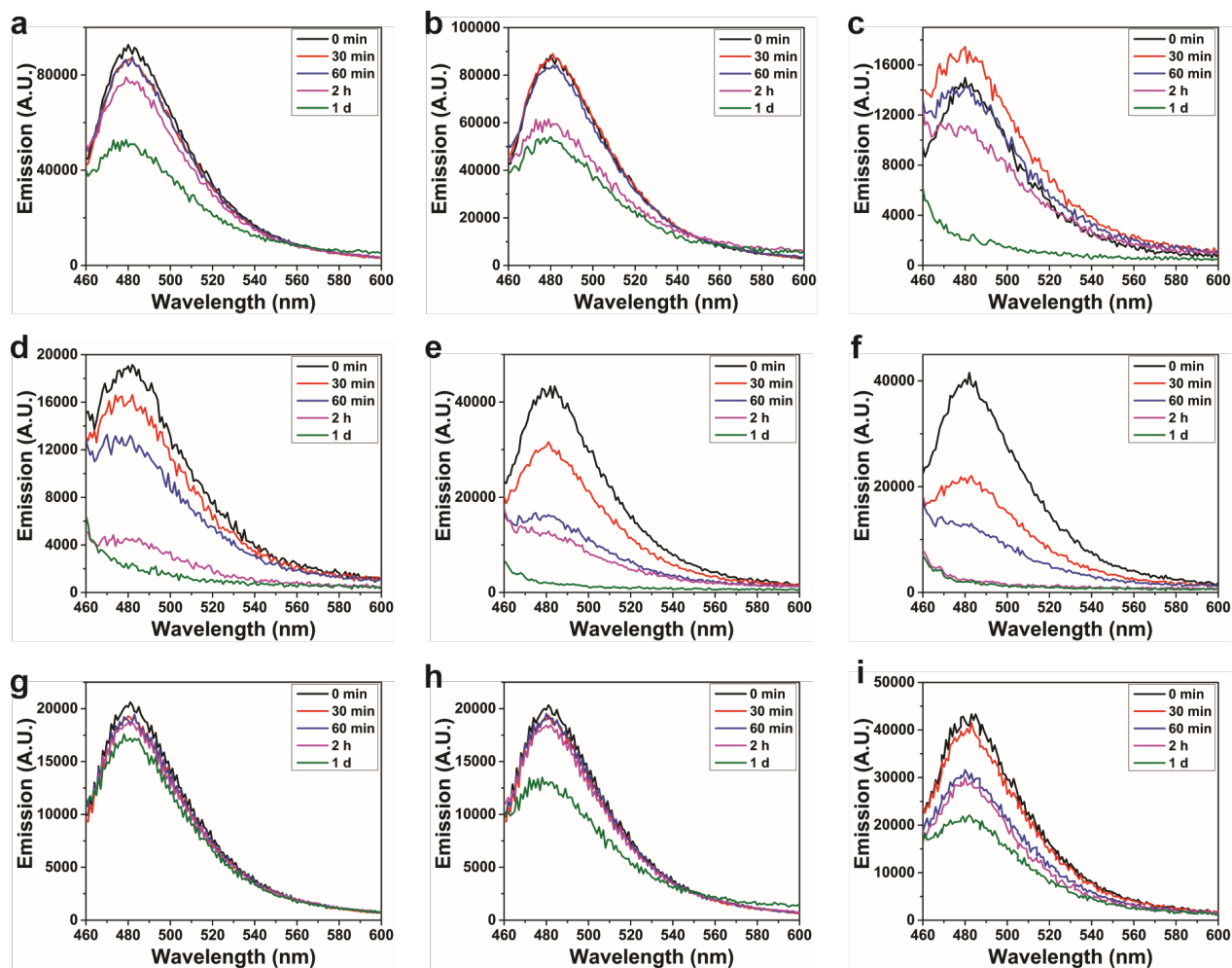


Figure 4.16. ThT emission spectra excited at 450 nm of small, medium, and large Au NP single helices upon incubating with different concentrations of urea. NP sizes: (a, b, c) small, (d, e, f) medium, (g, h, i) large. Urea concentrations: (a, d, g) 0.5 M, (b, e, h) 1 M, (c, f, i) 2 M.

4.3 Conclusion

In summary, we examined the stability of Au NP single helices formed using C_{18} - $(PEP_{Au}^{ox})_2$. We studied the stability at elevated temperatures and in the presence of two peptide denaturants, ProK and urea. Our data indicate that helices with larger particles are more structurally robust in the presence of increased temperature and in the presence of ProK and urea.

We reason that as the particles become larger, the peptide fiber becomes more shielded and less accessible to ProK. Urea, however, is a small molecule, and should easily be able to penetrate into the fiber scaffold, regardless of the NP dimensions. The larger particles may also impart greater stability because they ‘weld’ the structure together, preventing disassembly of the underlying peptide fibers. Inspired by the results in this study, we envision that the stability of single helices could be enhanced even further with further NP growth that ultimately leads to NP fusion and formation of 1D helical gold wires, which could potentially show interesting electromagnetic properties.

4.4 Supplementary Information

4.4.1 General Methods

All chemicals were purchased from commercial suppliers and used as received unless otherwise specified. Nanopure water (18.2 mΩ) was obtained using a Barnstead Diamond™ water purification system. Peptide and peptide conjugate syntheses were carried out on a CEM MARS 6™ synthesis microwave reactor. Peptide and peptide conjugates were purified using an Agilent 1200 reverse-phase high-performance liquid chromatography (RP-HPLC) system equipped with multiple wavelength detectors and a Zorbax-300SB C₁₈ column. A linear gradient of 5-95% acetonitrile (with 1% formic acid) over 30 min was used to elute peptide samples. Molecular mass of purified peptides and peptide conjugates were confirmed on a Shimadzu liquid chromatography-mass spectroscopy (LC-MS) 2020 system. Agilent 8453 UV-vis spectrometer with quartz cuvette

(10 mm path length) was used to quantify peptide conjugate based on tyrosine absorbance at 280 nm. All microscopy measurements were performed using ImageJ software.

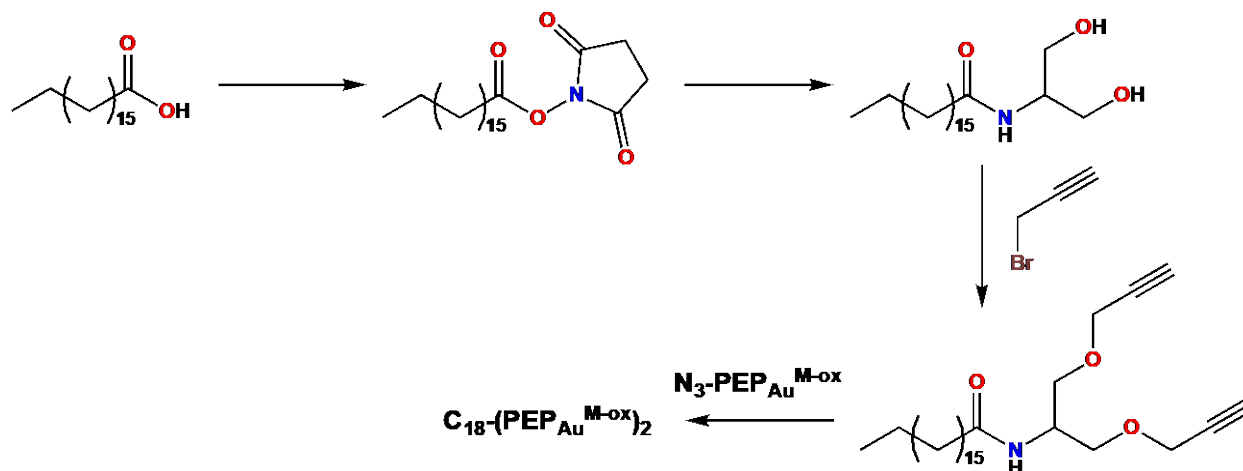


Figure 4.17 Synthetic scheme for peptide conjugate $C_{18}-(PEP_{Au}^{M-ox})_2$.

4.4.2 Solid-Phase Peptide Synthesis of PEP_{Au} and N_3-PEP_{Au}

N_3-PEP_{Au} was synthesized by manual microwave-assisted Fmoc solid phase methods using a CEM MARS microwave and NovaSyn TGA Fmoc-Phe resin (Milipore catalog number: 8560340001). The resin was first soaked in dimethylformamide (DMF) for 15 minutes and a 2 mL Fmoc-deprotection solution consisting of 20% 4-methylpiperidine in DMF was added. Fmoc deprotections were performed with a 1 min ramp to 75 °C, followed by a 2 min hold at that temperature with stirring. Thereafter, excess solution was drained using a filtration manifold and washed with 2 mL DMF for three times. Thereafter, a 1.25 mL coupling solution consisting of 0.1 M HCTU (*O*-(1H-6-chlorobenzotriazole-1-yl)-1,1,3,3-tetramethyluronium hexafluorophosphate,

5 eq. to resin) in NMP (1-methyl-2-pyrrolidinone), vortexed with Fmoc-protected amino acid (5 eq. to resin) and DIEA (N,N-diisopropylethylamine, 7 eq. to resin), was added. Coupling reactions were then performed with a 1 min ramp to 75 °C, followed by a 5 min hold at that temperature while stirring. Thereafter, excess reagent was drained and the residue was washed with DMF for three time. This coupling-deprotection cycle was repeated for every amino acid. Proline and adjacent amino acids were coupled twice to ensure complete reaction of secondary amide group. At this step, crude PEP_{Au} was cleaved from resin after the final deprotection step; whereas for N₃-PEP_{Au}, the N-terminus was capped with 5-azido pentanoic acid (4 eq. to resin). The resin was then washed with DMF, methylene chloride, and methanol. The peptides was then cleaved from resin using a 2 mL cleavage cocktail (95/2.5/2.5 trifluoroacetic acid/triisopropylsilane/H₂O). Crude peptide was precipitated by adding the resin-cleavage cocktail to cold Et₂O and washed by Et₂O for two times. The peptide was then dissolved in 1/1 acetonitrile/water, and stored at 4 °C, before further purified with RP-HPLC.

4.4.3 Preparation of N₃-PEP_{Au}^{M-ox} and C₁₈-(PEP_{Au}^{M-ox})₂

Details of oxidation of N₃-PEP_{Au}, synthesis of C₁₈-dialkyne, and copper assisted “click” coupling of C₁₈-dialkyne to N₃-PEP_{Au}^{M-ox} to yield C₁₈-(PEP_{Au}^{M-ox})₂ were described in our previous publications.²⁷⁻²⁸

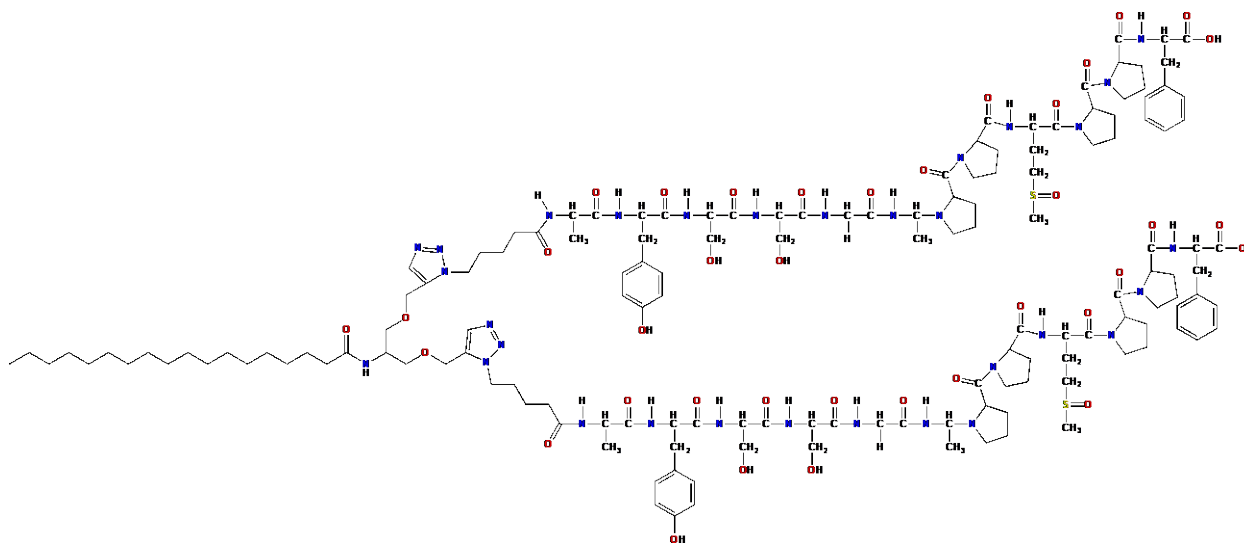


Figure 4.18. Molecular structure of C_{18} -(PEPAu^{M-ox})₂

4.4.4 Synthesis of Small Au NP Single Helices

Small helical Au NP superstructures were prepared using established methods with minor modifications.²⁷⁻²⁸ Briefly, 20 nmol of lyophilized C_{18} -(PEPAu^{M-ox})₂ was dissolved in 200 μ L 0.1 M HEPES buffer. Next, the sample was sonicated for 5 min, before it was left undisturbed at room temperature for 25 min. Toward the end of the 25 min incubation, a gold precursor solution was freshly prepared by vortexing 0.1 M HAuCl₄ in H₂O and 1 M triethylammonium acetate (TEAA) buffer for 1 min. After the 25 min, 2 μ L of the gold precursor solution was added to the peptide buffer solution. Upon observing a black precipitate, the reaction vial was vortexed and left at room temperature for 18 hours. The sample was then centrifuged (5 krpm, 10 min) and re-dispersed in 200 μ L 0.1 M HEPES buffer.

4.4.5 Synthesis of Medium and Large Au NP Single Helices

Medium Au NP single helices were prepared following a previously reported procedure with slight modification.¹⁰⁶ First, small Au NP helices were synthesized using the method described in the previous section, where the 200 μL 0.1 M HEPES was replaced with 200 μL 0.08 M HEPES/0.02 M citrate buffer. After incubated for 18 hours, 1 μl of 0.1M HAuCl_4 was added and then the vial was vortexed for 5 seconds. After incubation of the above mixture solution for 1 minute, 100 μl 0.01 M Hydroquinone, 0.08 M HEPES and 0.02 M citrate buffer was added. The mixture solution was vortexed for 3 minutes and the color became dark purple. Precipitate was also observed. After 1 h, the solution was centrifuged (5 krpm, 10 min) and re-dispersed in 200 μL 0.1 M HEPES.

For large Au NP single helices, a second round of growth process was carried out based on medium Au NP single helices. And the large Au NP single helices was centrifuged and re-dispersed in 200 μL 0.1 M HEPES as well.

4.4.6 Transmission Electron Microscopy (TEM)

TEM imaging was performed on a FEI Morgagni 268 operated at 80 kV and equipped with an advanced microscopy techniques (AMT) side mount charge-coupled device (CCD) camera system. TEM samples were prepared by drop-casting 5 μL of sample onto a 3 mm diameter copper grid with Formvar coating. After 5 min, excess solution was removed by filter paper and the sample was air-dried for 1 min. And 5 μL of H_2O was applied to the grid to remove excess solvent. After 1 min, the H_2O was removed and the grid was left to air dry for 5 min. Negatively stained TEM samples were prepared by adding 5 μL 2% uranyl acetate solution to the grid after it was air dried

for 5 min. Next, after 5 min, the excess staining solution was removed by filter paper and the grid was left to air dry for 5 min.

4.4.7 Circular Dichroism (CD) Spectroscopy

CD studies of Au NP single helices were conducted on an Olis DSM 17 CD spectrometer with a quartz cuvette (path length 0.1 cm). For temperature studies, each sample was loaded in the cuvette and incubated according to the temperature ramp described in the manuscript. For ProK studies, the cuvette was held at 37 °C. For urea studies, the cuvette was held at room temperature.

4.4.8 Fluorescence Studies

4.4.8.1 Molecular Structure of Thioflavin T (ThT)

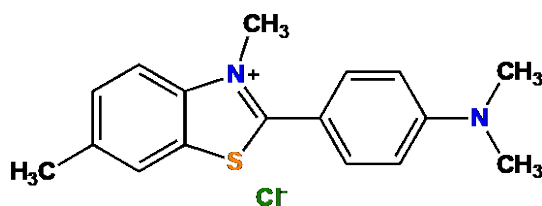


Figure 4.19. Molecular structure of thioflavin T (ThT)

4.4.8.2 ThT Fluorescence Studies for Peptide Assemblies

ThT fluorescence were recorded on a Horiba Jobin Yvon (HJY) Fluoromax 3 spectrofluorimeter using a quartz cuvette. Each sample was allowed to incubate with ThT (5 μM) overnight, and was excited at 450 nm while emission was recorded from 460 to 600 nm. For temperature studies, each sample was loaded in the cuvette and incubated according to the

temperature ramp described in the manuscript. For ProK studies, the cuvette was held at 37 °C.

For urea studies, the cuvette was held at room temperature.

Bibliography

1. Heiligtag, F. J.; Niederberger, M. The fascinating world of nanoparticle research. *Mater. Today* **2013**, *16* (7), 262-271.
2. Moshfegh, A. Z. Nanoparticle catalysts. *J. Phys. D: Appl. Phys.* **2009**, *42* (23), 233001.
3. Li, Y.; Qian, F.; Xiang, J.; Lieber, C. M. Nanowire electronic and optoelectronic devices. *Mater. Today* **2006**, *9* (10), 18-27.
4. Medintz, I. L.; Uyeda, H. T.; Goldman, E. R.; Mattoussi, H. Quantum dot bioconjugates for imaging, labelling and sensing. *Nat. Mater.* **2005**, *4* (6), 435-446.
5. Stewart, M. E.; Anderton, C. R.; Thompson, L. B.; Maria, J.; Gray, S. K.; Rogers, J. A.; Nuzzo, R. G. Nanostructured Plasmonic Sensors. *Chem. Rev.* **2008**, *108* (2), 494-521.
6. Tong, L.; Wei, Q.; Wei, A.; Cheng, J.-X. Gold Nanorods as Contrast Agents for Biological Imaging: Optical Properties, Surface Conjugation and Photothermal Effects†. *Photochem. Photobiol.* **2009**, *85* (1), 21-32.
7. Boles, M. A.; Engel, M.; Talapin, D. V. Self-Assembly of Colloidal Nanocrystals: From Intricate Structures to Functional Materials. *Chem. Rev.* **2016**, *116* (18), 11220-11289.
8. Maier, S. A.; Atwater, H. A. Plasmonics: Localization and guiding of electromagnetic energy in metal/dielectric structures. *J. Appl. Phys.* **2005**, *98* (1), 011101.
9. Ozbay, E. Plasmonics: Merging Photonics and Electronics at Nanoscale Dimensions. *Science* **2006**, *311* (5758), 189-193.
10. Tang, Z.; Wang, Y.; Podsiadlo, P.; Kotov, N. A. Biomedical Applications of Layer-by-Layer Assembly: From Biomimetics to Tissue Engineering. *Adv. Mater.* **2006**, *18* (24), 3203-3224.
11. Zeng, S.; Baillargeat, D.; Ho, H.-P.; Yong, K.-T. Nanomaterials enhanced surface plasmon resonance for biological and chemical sensing applications. *Chem. Soc. Rev.* **2014**, *43* (10), 3426-3452.
12. Pengo, P.; Broxterman, Q. B.; Kaptein, B.; Pasquato, L.; Scrimin, P. Synthesis of a Stable Helical Peptide and Grafting on Gold Nanoparticles. *Langmuir* **2003**, *19* (6), 2521-2524.
13. Stevens, M. M.; Flynn, N. T.; Wang, C.; Tirrell, D. A.; Langer, R. Coiled-Coil Peptide-Based Assembly of Gold Nanoparticles. *Adv. Mater.* **2004**, *16* (11), 915-918.
14. Slocik, J. M.; Stone, M. O.; Naik, R. R. Synthesis of Gold Nanoparticles Using Multifunctional Peptides. *Small* **2005**, *1* (11), 1048-1052.

15. Aili, D.; Enander, K.; Rydberg, J.; Nesterenko, I.; Björefors, F.; Baltzer, L.; Liedberg, B. Folding Induced Assembly of Polypeptide Decorated Gold Nanoparticles. *J. Am. Chem. Soc.* **2008**, *130* (17), 5780-5788.
16. Chen, C.-L.; Zhang, P.; Rosi, N. L. A New Peptide-Based Method for the Design and Synthesis of Nanoparticle Superstructures: Construction of Highly Ordered Gold Nanoparticle Double Helices. *J. Am. Chem. Soc.* **2008**, *130* (41), 13555-13557.
17. Hnilova, M.; Oren, E. E.; Seker, U. O. S.; Wilson, B. R.; Collino, S.; Evans, J. S.; Tamerler, C.; Sarikaya, M. Effect of Molecular Conformations on the Adsorption Behavior of Gold-Binding Peptides. *Langmuir* **2008**, *24* (21), 12440-12445.
18. Si, S.; Raula, M.; Paira, T. K.; Mandal, T. K. Reversible Self-Assembly of Carboxylated Peptide-Functionalized Gold Nanoparticles Driven by Metal-Ion Coordination. *ChemPhysChem* **2008**, *9* (11), 1578-1584.
19. Coomber, D.; Bartczak, D.; Gerrard, S. R.; Tyas, S.; Kanaras, A. G.; Stulz, E. Programmed Assembly of Peptide-Functionalized Gold Nanoparticles on DNA Templates. *Langmuir* **2010**, *26* (17), 13760-13762.
20. Song, C.; Zhao, G.; Zhang, P.; Rosi, N. L. Expeditious Synthesis and Assembly of Sub-100 nm Hollow Spherical Gold Nanoparticle Superstructures. *J. Am. Chem. Soc.* **2010**, *132* (40), 14033-14035.
21. Hwang, L.; Zhao, G.; Zhang, P.; Rosi, N. L. Size-Controlled Peptide-Directed Synthesis of Hollow Spherical Gold Nanoparticle Superstructures. *Small* **2011**, *7* (14), 1939-1942.
22. Nonoyama, T.; Tanaka, M.; Inai, Y.; Higuchi, M.; Kinoshita, T. Ordered Nanopattern Arrangement of Gold Nanoparticles on β -Sheet Peptide Templates through Nucleobase Pairing. *ACS Nano* **2011**, *5* (8), 6174-6183.
23. Seker, U. O. S.; Wilson, B.; Kulp, J. L.; Evans, J. S.; Tamerler, C.; Sarikaya, M. Thermodynamics of Engineered Gold Binding Peptides: Establishing the Structure–Activity Relationships. *Biomacromolecules* **2014**, *15* (7), 2369-2377.
24. Zhang, C.; Zhou, Y.; Merg, A.; Song, C.; Schatz, G. C.; Rosi, N. L. Hollow spherical gold nanoparticle superstructures with tunable diameters and visible to near-infrared extinction. *Nanoscale* **2014**, *6* (21), 12328-12332.
25. Merg, A. D.; Slocik, J.; Blaber, M. G.; Schatz, G. C.; Naik, R.; Rosi, N. L. Adjusting the Metrics of 1-D Helical Gold Nanoparticle Superstructures Using Multivalent Peptide Conjugates. *Langmuir* **2015**, *31* (34), 9492-9501.
26. Tadepalli, S.; Kuang, Z.; Jiang, Q.; Liu, K.-K.; Fisher, M. A.; Morrissey, J. J.; Kharasch, E. D.; Slocik, J. M.; Naik, R. R.; Singamaneni, S. Peptide Functionalized Gold Nanorods for the Sensitive Detection of a Cardiac Biomarker Using Plasmonic Paper Devices. *Sci. Rep.* **2015**, *5* (1), 16206.

27. Merg, A. D.; Boatz, J. C.; Mandal, A.; Zhao, G.; Mokashi-Punekar, S.; Liu, C.; Wang, X.; Zhang, P.; van der Wel, P. C. A.; Rosi, N. L. Peptide-Directed Assembly of Single-Helical Gold Nanoparticle Superstructures Exhibiting Intense Chiroptical Activity. *J. Am. Chem. Soc.* **2016**, *138* (41), 13655-13663.
28. Mokashi-Punekar, S.; Merg, A. D.; Rosi, N. L. Systematic Adjustment of Pitch and Particle Dimensions within a Family of Chiral Plasmonic Gold Nanoparticle Single Helices. *J. Am. Chem. Soc.* **2017**, *139* (42), 15043-15048.
29. Zong, J.; Cobb, S. L.; Cameron, N. R. Peptide-functionalized gold nanoparticles: versatile biomaterials for diagnostic and therapeutic applications. *Biomater. Sci.* **2017**, *5* (5), 872-886.
30. Lee, H.-E.; Ahn, H.-Y.; Mun, J.; Lee, Y. Y.; Kim, M.; Cho, N. H.; Chang, K.; Kim, W. S.; Rho, J.; Nam, K. T. Amino-acid- and peptide-directed synthesis of chiral plasmonic gold nanoparticles. *Nature* **2018**, *556* (7701), 360-365.
31. Yang, S.; Yao, D.; Wang, Y.; Yang, W.; Zhang, B.; Wang, D. Enzyme-triggered self-assembly of gold nanoparticles for enhanced retention effects and photothermal therapy of prostate cancer. *Chem. Commun.* **2018**, *54* (70), 9841-9844.
32. Mahato, K.; Nagpal, S.; Shah, M. A.; Srivastava, A.; Maurya, P. K.; Roy, S.; Jaiswal, A.; Singh, R.; Chandra, P. Gold nanoparticle surface engineering strategies and their applications in biomedicine and diagnostics. *3 Biotech* **2019**, *9* (2), 57.
33. Pigliacelli, C.; Sanjeeva, K. B.; Nonappa; Pizzi, A.; Gori, A.; Bombelli, F. B.; Metrangolo, P. In Situ Generation of Chiroptically-Active Gold-Peptide Superstructures Promoted by Iodination. *ACS Nano* **2019**.
34. Tanaka, M.; Takahashi, Y.; Roach, L.; Critchley, K.; D. Evans, S.; Okochi, M. Rational screening of biomineralisation peptides for colour-selected one-pot gold nanoparticle syntheses. *Nanoscale Advances* **2019**, *1* (1), 71-75.
35. Han, G.; You, C. C.; Kim, B. J.; Turingan, R. S.; Forbes, N. S.; Martin, C. T.; Rotello, V. M. Light-regulated release of DNA and its delivery to nuclei by means of photolabile gold nanoparticles. *Angew. Chem. Int. Ed.* **2006**, *45* (19), 3165-3169.
36. Song, J.; Zhou, J.; Duan, H. Self-Assembled Plasmonic Vesicles of SERS-Encoded Amphiphilic Gold Nanoparticles for Cancer Cell Targeting and Traceable Intracellular Drug Delivery. *J. Am. Chem. Soc.* **2012**, *134* (32), 13458-13469.
37. Mura, S.; Nicolas, J.; Couvreur, P. Stimuli-responsive nanocarriers for drug delivery. *Nat. Mater.* **2013**, *12* (11), 991-1003.
38. Hu, R.; Zhang, X.-B.; Kong, R.-M.; Zhao, X.-H.; Jiang, J.; Tan, W. Nucleic acid-functionalized nanomaterials for bioimaging applications. *J. Mater. Chem.* **2011**, *21* (41), 16323-16334.

39. Zeng, S.; Yong, K.-T.; Roy, I.; Dinh, X.-Q.; Yu, X.; Luan, F. A Review on Functionalized Gold Nanoparticles for Biosensing Applications. *Plasmonics* **2011**, *6* (3), 491-506.
40. Whaley, S. R.; English, D. S.; Hu, E. L.; Barbara, P. F.; Belcher, A. M. Selection of peptides with semiconductor binding specificity for directed nanocrystal assembly. *Nature* **2000**, *405* (6787), 665-668.
41. Lee, K.-S.; El-Sayed, M. A. Gold and silver nanoparticles in sensing and imaging: Sensitivity of plasmon response to size, shape, and metal composition. *J. Phys. Chem. B* **2006**, *110* (39), 19220-19225.
42. Anker, J. N.; Hall, W. P.; Lyandres, O.; Shah, N. C.; Zhao, J.; Van Duyne, R. P. Biosensing with plasmonic nanosensors. *Nat. Mater.* **2008**, *7* (6), 442-453.
43. Agasti, S. S.; Chompoosor, A.; You, C.-C.; Ghosh, P.; Kim, C. K.; Rotello, V. M. Photoregulated Release of Caged Anticancer Drugs from Gold Nanoparticles. *J. Am. Chem. Soc.* **2009**, *131* (16), 5728-5729.
44. Cheng, Y.; Samia, A. C.; Li, J.; Kenney, M. E.; Resnick, A.; Burda, C. Delivery and Efficacy of a Cancer Drug as a Function of the Bond to the Gold Nanoparticle Surface. *Langmuir* **2010**, *26* (4), 2248-2255.
45. Doane, T. L.; Burda, C. The unique role of nanoparticles in nanomedicine: imaging, drug delivery and therapy. *Chem. Soc. Rev.* **2012**, *41* (7), 2885-2911.
46. Couvreur, P. Nanoparticles in drug delivery: Past, present and future. *Adv. Drug Deliv. Rev.* **2013**, *65* (1), 21-23.
47. Nam, J.; La, W.-G.; Hwang, S.; Ha, Y. S.; Park, N.; Won, N.; Jung, S.; Bhang, S. H.; Ma, Y.-J.; Cho, Y.-M.; Jin, M.; Han, J.; Shin, J.-Y.; Wang, E. K.; Kim, S. G.; Cho, S.-H.; Yoo, J.; Kim, B.-S.; Kim, S. pH-Responsive Assembly of Gold Nanoparticles and "Spatiotemporally Concerted" Drug Release for Synergistic Cancer Therapy. *ACS Nano* **2013**, *7* (4), 3388-3402.
48. Tang, L.; Li, S.; Xu, L.; Ma, W.; Kuang, H.; Wang, L.; Xu, C. Chirality-based Au@Ag Nanorod Dimers Sensor for Ultrasensitive PSA Detection. *ACS Appl. Mater. Interfaces* **2015**, *7* (23), 12708-12712.
49. Willets, K. A.; Van Duyne, R. P. Localized Surface Plasmon Resonance Spectroscopy and Sensing. *Annu. Rev. Phys. Chem.* **2007**, *58* (1), 267-297.
50. Kamat, P. V. Photophysical, photochemical and photocatalytic aspects of metal nanoparticles. *J. Phys. Chem. B* **2002**, *106* (32), 7729-7744.
51. Daniel, M. C.; Astruc, D. Gold nanoparticles: Assembly, supramolecular chemistry, quantum-size-related properties, and applications toward biology, catalysis, and nanotechnology. *Chem. Rev.* **2004**, *104* (1), 293-346.

52. Mostafa, S.; Behafarid, F.; Croy, J. R.; Ono, L. K.; Li, L.; Yang, J. C.; Frenkel, A. I.; Cuenya, B. R. Shape-Dependent Catalytic Properties of Pt Nanoparticles. *J. Am. Chem. Soc.* **2010**, *132* (44), 15714-15719.
53. Wei, Y.; Han, S.; Kim, J.; Soh, S.; Grzybowski, B. A. Photoswitchable Catalysis Mediated by Dynamic Aggregation of Nanoparticles. *J. Am. Chem. Soc.* **2010**, *132* (32), 11018-11020.
54. Maier, S. A., *Plasmonics: Fundamentals and Applications*. Springer US: New York, NY, 2007.
55. Kelly, K. L.; Coronado, E.; Zhao, L. L.; Schatz, G. C. The Optical Properties of Metal Nanoparticles: The Influence of Size, Shape, and Dielectric Environment. *J. Phys. Chem. B* **2003**, *107* (3), 668-677.
56. Lee, K.-S.; El-Sayed, M. A. Gold and Silver Nanoparticles in Sensing and Imaging: Sensitivity of Plasmon Response to Size, Shape, and Metal Composition. *J. Phys. Chem. B* **2006**, *110* (39), 19220-19225.
57. Skrabalak, S. E.; Au, L.; Li, X.; Xia, Y. Facile synthesis of Ag nanocubes and Au nanocages. *Nat. Protoc.* **2007**, *2* (9), 2182-2190.
58. Gurunatha, K. L.; Fournier, A. C.; Urvoas, A.; Valerio-Lepiniec, M.; Marchi, V.; Minard, P.; Dujardin, E. Nanoparticles Self-Assembly Driven by High Affinity Repeat Protein Pairing. *ACS Nano* **2016**, *10* (3), 3176-3185.
59. Cai, C.; Lin, J.; Lu, Y.; Zhang, Q.; Wang, L. Polypeptide self-assemblies: nanostructures and bioapplications. *Chem. Soc. Rev.* **2016**, *45* (21), 5985-6012.
60. Kim, S.; Kim, J. H.; Lee, J. S.; Park, C. B. Beta-Sheet-Forming, Self-Assembled Peptide Nanomaterials towards Optical, Energy, and Healthcare Applications. *Small* **2015**, *11* (30), 3623-3640.
61. Kumar, J.; Eraña, H.; López-Martínez, E.; Claes, N.; Martín, V. F.; Solís, D. M.; Bals, S.; Cortajarena, A. L.; Castilla, J.; Liz-Marzán, L. M. Detection of amyloid fibrils in Parkinson's disease using plasmonic chirality. *Proc. Natl. Acad. Sci. U. S. A.* **2018**, *115* (13), 3225.
62. Reches, M.; Gazit, E. Formation of Closed-Cage Nanostructures by Self-Assembly of Aromatic Dipeptides. *Nano Lett.* **2004**, *4* (4), 581-585.
63. Li, L.-s.; Stupp, S. I. One-Dimensional Assembly of Lipophilic Inorganic Nanoparticles Templated by Peptide-Based Nanofibers with Binding Functionalities. *Angew. Chem. Int. Ed.* **2005**, *44* (12), 1833-1836.
64. Hendricks, M. P.; Sato, K.; Palmer, L. C.; Stupp, S. I. Supramolecular Assembly of Peptide Amphiphiles. *Acc. Chem. Res.* **2017**, *50* (10), 2440-2448.

65. Wei, G.; Su, Z.; Reynolds, N. P.; Arosio, P.; Hamley, I. W.; Gazit, E.; Mezzenga, R. Self-assembling peptide and protein amyloids: from structure to tailored function in nanotechnology. *Chem. Soc. Rev.* **2017**, *46* (15), 4661-4708.
66. Hamley, I. W.; Dehsorkhi, A.; Castelletto, V. Self-assembled arginine-coated peptide nanosheets in water. *Chem. Commun.* **2013**, *49* (18), 1850-1852.
67. Hamley, I. W.; Castelletto, V. Self-Assembly of Peptide Bioconjugates: Selected Recent Research Highlights. *Bioconjugate Chem.* **2017**, *28* (3), 731-739.
68. Xie, X.; Wang, L.; Liu, X.; Du, Z.; Li, Y.; Li, B.; Wu, L.; Li, W. Light-powered and transient peptide two-dimensional assembly driven by trans-to-cis isomerization of azobenzene side chains. *Chem. Commun.* **2020**.
69. Taskova, M.; Madsen, C. S.; Jensen, K. J.; Hansen, L. H.; Vester, B.; Astakhova, K. Antisense Oligonucleotides Internally Labeled with Peptides Show Improved Target Recognition and Stability to Enzymatic Degradation. *Bioconjugate Chem.* **2017**, *28* (3), 768-774.
70. Gao, X.; Matsui, H. Peptide-Based Nanotubes and Their Applications in Bionanotechnology. *Adv. Mater.* **2005**, *17* (17), 2037-2050.
71. de la Rica, R.; Matsui, H. Applications of peptide and protein-based materials in bionanotechnology. *Chem. Soc. Rev.* **2010**, *39* (9), 3499-3509.
72. Tiede, C.; Tang, A. A. S.; Deacon, S. E.; Mandal, U.; Nettleship, J. E.; Owen, R. L.; George, S. E.; Harrison, D. J.; Owens, R. J.; Tomlinson, D. C.; McPherson, M. J. Adhiron: a stable and versatile peptide display scaffold for molecular recognition applications. *Protein Eng. Des. Sel.* **2014**, *27* (5), 145-155.
73. Hoshino, Y.; Koide, H.; Urakami, T.; Kanazawa, H.; Kodama, T.; Oku, N.; Shea, K. J. Recognition, Neutralization, and Clearance of Target Peptides in the Bloodstream of Living Mice by Molecularly Imprinted Polymer Nanoparticles: A Plastic Antibody. *J. Am. Chem. Soc.* **2010**, *132* (19), 6644-6645.
74. Chen, C.-L.; Rosi, N. L. Peptide-Based Methods for the Preparation of Nanostructured Inorganic Materials. *Angew. Chem. Int. Ed.* **2010**, *49* (11), 1924-1942.
75. Pierschbacher, M. D.; Ruoslahti, E. Cell attachment activity of fibronectin can be duplicated by small synthetic fragments of the molecule. *Nature* **1984**, *309* (5963), 30-33.
76. Webber, M. J.; Tongers, J.; Renault, M.-A.; Roncalli, J. G.; Losordo, D. W.; Stupp, S. I. Development of bioactive peptide amphiphiles for therapeutic cell delivery. *Acta Biomater.* **2010**, *6* (1), 3-11.
77. Birnbaum, Michael E.; Mendoza, Juan L.; Sethi, Dhruv K.; Dong, S.; Glanville, J.; Dobbins, J.; Özkan, E.; Davis, Mark M.; Wucherpennig, Kai W.; Garcia, K. C.

- Deconstructing the Peptide-MHC Specificity of T Cell Recognition. *Cell* **2014**, *157* (5), 1073-1087.
78. Hersel, U.; Dahmen, C.; Kessler, H. RGD modified polymers: biomaterials for stimulated cell adhesion and beyond. *Biomaterials* **2003**, *24* (24), 4385-4415.
 79. Danhier, F.; Le Breton, A.; Pr at, V. RGD-Based Strategies To Target Alpha(v) Beta(3) Integrin in Cancer Therapy and Diagnosis. *Mol. Pharm.* **2012**, *9* (11), 2961-2973.
 80. Dickerson, M. B.; Sandhage, K. H.; Naik, R. R. Protein- and Peptide-Directed Syntheses of Inorganic Materials. *Chem. Rev.* **2008**, *108* (11), 4935-4978.
 81. Yang, W.; Guo, W.; Chang, J.; Zhang, B. Protein/peptide-templated biomimetic synthesis of inorganic nanoparticles for biomedical applications. *J. Mater. Chem. B* **2017**, *5* (3), 401-417.
 82. Naik, R. R.; Stringer, S. J.; Agarwal, G.; Jones, S. E.; Stone, M. O. Biomimetic synthesis and patterning of silver nanoparticles. *Nat. Mater.* **2002**, *1* (3), 169-172.
 83. Djalali, R.; Chen, Y.-f.; Matsui, H. Au Nanowire Fabrication from Sequenced Histidine-Rich Peptide. *J. Am. Chem. Soc.* **2002**, *124* (46), 13660-13661.
 84. Slocik, J. M.; Moore, J. T.; Wright, D. W. Monoclonal Antibody Recognition of Histidine-Rich Peptide Encapsulated Nanoclusters. *Nano Lett.* **2002**, *2* (3), 169-173.
 85. Brown, S. Metal-recognition by repeating polypeptides. *Nat. Biotechnol.* **1997**, *15* (3), 269-272.
 86. Yu, L.; Banerjee, I. A.; Matsui, H. Direct Growth of Shape-Controlled Nanocrystals on Nanotubes via Biological Recognition. *J. Am. Chem. Soc.* **2003**, *125* (48), 14837-14840.
 87. Banerjee, I. A.; Yu, L.; Matsui, H. Cu nanocrystal growth on peptide nanotubes by biomineralization: Size control of Cu nanocrystals by tuning peptide conformation. *Proc. Natl. Acad. Sci. U. S. A.* **2003**, *100* (25), 14678.
 88. Slocik, J. M.; Wright, D. W. Biomimetic Mineralization of Noble Metal Nanoclusters. *Biomacromolecules* **2003**, *4* (5), 1135-1141.
 89. Sarikaya, M.; Tamerler, C.; Jen, A. K. Y.; Schulten, K.; Baneyx, F. Molecular biomimetics: nanotechnology through biology. *Nat. Mater.* **2003**, *2* (9), 577-585.
 90. Brown, S.; Sarikaya, M.; Johnson, E. A genetic analysis of crystal growth | Edited by M. Gottesman. *Journal of Molecular Biology* **2000**, *299* (3), 725-735.
 91. Huang, Y.; Chiang, C.-Y.; Lee, S. K.; Gao, Y.; Hu, E. L.; Yoreo, J. D.; Belcher, A. M. Programmable Assembly of Nanoarchitectures Using Genetically Engineered Viruses. *Nano Lett.* **2005**, *5* (7), 1429-1434.

92. Nam, K. T.; Kim, D.-W.; Yoo, P. J.; Chiang, C.-Y.; Meethong, N.; Hammond, P. T.; Chiang, Y.-M.; Belcher, A. M. Virus-Enabled Synthesis and Assembly of Nanowires for Lithium Ion Battery Electrodes. *Science* **2006**, *312* (5775), 885.
93. Wei, Z.; Maeda, Y.; Matsui, H. Discovery of Catalytic Peptides for Inorganic Nanocrystal Synthesis by a Combinatorial Phage Display Approach. *Angew. Chem. Int. Ed.* **2011**, *50* (45), 10585-10588.
94. Umetsu, M.; Mizuta, M.; Tsumoto, K.; Ohara, S.; Takami, S.; Watanabe, H.; Kumagai, I.; Adschiri, T. Bioassisted Room-Temperature Immobilization and Mineralization of Zinc Oxide—The Structural Ordering of ZnO Nanoparticles into a Flower-Type Morphology. *Adv. Mater.* **2005**, *17* (21), 2571-2575.
95. Chiu, C.-Y.; Li, Y.; Ruan, L.; Ye, X.; Murray, C. B.; Huang, Y. Platinum nanocrystals selectively shaped using facet-specific peptide sequences. *Nat. Chem.* **2011**, *3* (5), 393-399.
96. Peelle, B. R.; Krauland, E. M.; Wittrup, K. D.; Belcher, A. M. Probing the interface between biomolecules and inorganic materials using yeast surface display and genetic engineering. *Acta Biomater.* **2005**, *1* (2), 145-154.
97. Flynn, C. E.; Mao, C.; Hayhurst, A.; Williams, J. L.; Georgiou, G.; Iverson, B.; Belcher, A. M. Synthesis and organization of nanoscale II–VI semiconductor materials using evolved peptide specificity and viral capsid assembly. *J. Mater. Chem.* **2003**, *13* (10), 2414-2421.
98. Mao, C.; Solis, D. J.; Reiss, B. D.; Kottmann, S. T.; Sweeney, R. Y.; Hayhurst, A.; Georgiou, G.; Iverson, B.; Belcher, A. M. Virus-Based Toolkit for the Directed Synthesis of Magnetic and Semiconducting Nanowires. *Science* **2004**, *303* (5655), 213.
99. Reiss, B. D.; Mao, C.; Solis, D. J.; Ryan, K. S.; Thomson, T.; Belcher, A. M. Biological Routes to Metal Alloy Ferromagnetic Nanostructures. *Nano Lett.* **2004**, *4* (6), 1127-1132.
100. Khoo, X.; Hamilton, P.; O'Toole, G. A.; Snyder, B. D.; Kenan, D. J.; Grinstaff, M. W. Directed Assembly of PEGylated-Peptide Coatings for Infection-Resistant Titanium Metal. *J. Am. Chem. Soc.* **2009**, *131* (31), 10992-10997.
101. Sano, K.-I.; Sasaki, H.; Shiba, K. Specificity and Biomineralization Activities of Ti-Binding Peptide-1 (TBP-1). *Langmuir* **2005**, *21* (7), 3090-3095.
102. Fu, X.; Wang, Y.; Huang, L.; Sha, Y.; Gui, L.; Lai, L.; Tang, Y. Assemblies of Metal Nanoparticles and Self-Assembled Peptide Fibrils—Formation of Double Helical and Single-Chain Arrays of Metal Nanoparticles. *Adv. Mater.* **2003**, *15* (11), 902-906.
103. Carny, O.; Shalev, D. E.; Gazit, E. Fabrication of Coaxial Metal Nanocables Using a Self-Assembled Peptide Nanotube Scaffold. *Nano Lett.* **2006**, *6* (8), 1594-1597.

104. Mokashi-Punekar, S.; Zhou, Y.; Brooks, S. C.; Rosi, N. L. Construction of Chiral, Helical Nanoparticle Superstructures: Progress and Prospects. *Adv. Mater.* **2019**, 1905975.
105. Chen, C.-L.; Rosi, N. L. Preparation of Unique 1-D Nanoparticle Superstructures and Tailoring their Structural Features. *J. Am. Chem. Soc.* **2010**, *132* (20), 6902-6903.
106. Song, C.; Blaber, M. G.; Zhao, G.; Zhang, P.; Fry, H. C.; Schatz, G. C.; Rosi, N. L. Tailorable Plasmonic Circular Dichroism Properties of Helical Nanoparticle Superstructures. *Nano Lett.* **2013**, *13* (7), 3256-3261.
107. Hwang, L.; Chen, C.-L.; Rosi, N. L. Preparation of 1-D nanoparticle superstructures with tailorable thicknesses using gold-binding peptide conjugates. *Chem. Commun.* **2011**, *47* (1), 185-187.
108. Shimizu, T.; Masuda, M.; Minamikawa, H. Supramolecular Nanotube Architectures Based on Amphiphilic Molecules. *Chem. Rev.* **2005**, *105* (4), 1401-1444.
109. Zhang, C.; Brinzer, T.; Liu, C.; Garrett-Roe, S.; Rosi, N. L. Loading and triggered release of cargo from hollow spherical gold nanoparticle superstructures. *RSC Advances* **2015**, *5* (93), 76291-76295.
110. Mokashi-Punekar, S.; Rosi, N. L. Deliberate Introduction of Particle Anisotropy in Helical Gold Nanoparticle Superstructures. *Part. Part. Syst. Char.* **2019**, *36* (5), 1800504.
111. Jékely, G. Evolution of phototaxis. *Phil. Trans. R. Soc. B* **2009**, *364* (1531), 2795-2808.
112. Witman, G. B. Chlamydomonas phototaxis. *Trends Cell Biol.* **1993**, *3* (11), 403-408.
113. Cuthill, I. C. Camouflage. *J. Zool.* **2019**, *308* (2), 75-92.
114. Qu, Y.; Li, Q.; Cai, L.; Pan, M.; Ghosh, P.; Du, K.; Qiu, M. Thermal camouflage based on the phase-changing material GST. *Light Sci. Appl.* **2018**, *7* (1), 26.
115. Stuart-Fox, D.; Moussalli, A. Camouflage, communication and thermoregulation: lessons from colour changing organisms. *Phil. Trans. R. Soc. B* **2009**, *364* (1516), 463-470.
116. Cremaldi, J. C.; Bhushan, B. Bioinspired self-healing materials: lessons from nature. *Beilstein J. Nanotechnol.* **2018**, *9*, 907-935.
117. Davies, K. J. A. Adaptive homeostasis. *Mol. Asp. Med.* **2016**, *49*, 1-7.
118. Galluzzi, L.; Yamazaki, T.; Kroemer, G. Linking cellular stress responses to systemic homeostasis. *Nat. Rev. Mol. Cell Biol.* **2018**, *19* (11), 731-745.
119. Shah, J.; Zeier, J. Long-distance communication and signal amplification in systemic acquired resistance. *Front. Plant Sci.* **2013**, *4* (30).

120. Soh, S.; Byrska, M.; Kandere-Grzybowska, K.; Grzybowski, B. A. Reaction-Diffusion Systems in Intracellular Molecular Transport and Control. *Angew. Chem. Int. Ed.* **2010**, *49* (25), 4170-4198.
121. Lei, J.; Ju, H. Signal amplification using functional nanomaterials for biosensing. *Chem. Soc. Rev.* **2012**, *41* (6), 2122-2134.
122. Mann, S. The Origins of Life: Old Problems, New Chemistries. *Angew. Chem. Int. Ed.* **2013**, *52* (1), 155-162.
123. Grzybowski, B. A.; Huck, W. T. S. The nanotechnology of life-inspired systems. *Nat. Nanotechnol.* **2016**, *11* (7), 585-592.
124. Klajn, R.; Stoddart, J. F.; Grzybowski, B. A. Nanoparticles functionalised with reversible molecular and supramolecular switches. *Chem. Soc. Rev.* **2010**, *39* (6), 2203-2237.
125. Klajn, R. Spiropyran-based dynamic materials. *Chem. Soc. Rev.* **2014**, *43* (1), 148-184.
126. Kundu, P. K.; Samanta, D.; Leizrowice, R.; Margulis, B.; Zhao, H.; Boerner, M.; Udayabhaskararao, T.; Manna, D.; Klajn, R. Light-controlled self-assembly of non-photoresponsive nanoparticles. *Nat. Chem.* **2015**, *7* (8), 646-652.
127. Lee, J.-W.; Klajn, R. Dual-responsive nanoparticles that aggregate under the simultaneous action of light and CO₂. *Chem. Commun.* **2015**, *51* (11), 2036-2039.
128. Kundu, P. K.; Klajn, R. Watching Single Molecules Move in Response to Light. *ACS Nano* **2014**, *8* (12), 11913-11916.
129. Klajn, R.; Wesson, P. J.; Bishop, K. J. M.; Grzybowski, B. A. Writing Self-Erasing Images using Metastable Nanoparticle "Inks". *Angew. Chem. Int. Ed.* **2009**, *48* (38), 7035-7039.
130. Manna, D.; Udayabhaskararao, T.; Zhao, H.; Klajn, R. Orthogonal Light-Induced Self-Assembly of Nanoparticles using Differently Substituted Azobenzenes. *Angew. Chem. Int. Ed. Engl.* **2015**, *54* (42), 12394-12397.
131. Klajn, R.; Bishop, K. J. M.; Grzybowski, B. A. Light-controlled self-assembly of reversible and irreversible nanoparticle suprastructures. *Proc. Natl. Acad. Sci. U.S.A.* **2007**, *104* (25), 10305-10309.
132. Kundu, P. K.; Samanta, D.; Leizrowice, R.; Margulis, B.; Zhao, H.; Börner, M.; Udayabhaskararao, T.; Manna, D.; Klajn, R. Light-controlled self-assembly of non-photoresponsive nanoparticles. *Nat. Chem.* **2015**, *7*, 646-652.
133. Zhang, L.; Dai, L.; Rong, Y.; Liu, Z.; Tong, D.; Huang, Y.; Chen, T. Light-Triggered Reversible Self-Assembly of Gold Nanoparticle Oligomers for Tunable SERS. *Langmuir* **2015**, *31* (3), 1164-1171.

134. Ma, L. L.; Jia, J.; Yang, T. Y.; Yin, G. Z.; Liu, Y.; Sun, X.; Tao, X. T. Light-controlled self-assembly and conductance: from nanoribbons to nanospheres. *Rsc Advances* **2012**, *2* (7), 2902-2908.
135. Yagai, S.; Karatsu, T.; Kitamura, A. Photocontrollable self-assembly. *Chem. - Eur. J.* **2005**, *11* (14), 4054-4063.
136. Kim, J.-H.; Lee, T. R. Thermo- and pH-Responsive Hydrogel-Coated Gold Nanoparticles. *Chem. Mater.* **2004**, *16* (19), 3647-3651.
137. Klajn, R.; Browne, K. P.; Soh, S.; Grzybowski, B. A. Nanoparticles That "Remember" Temperature. *Small* **2010**, *6* (13), 1385-1387.
138. Bishop, K. J. M.; Kowalczyk, B.; Grzybowski, B. A. Precipitation of Oppositely Charged Nanoparticles by Dilution and/or Temperature Increase. *J. Phys. Chem. B* **2009**, *113* (5), 1413-1417.
139. Lewandowski, W.; Fruhnert, M.; Mieczkowski, J.; Rockstuhl, C.; Górecka, E. Dynamically self-assembled silver nanoparticles as a thermally tunable metamaterial. *Nat. Commun.* **2015**, *6* (1), 6590.
140. Hazarika, P.; Ceyhan, B.; Niemeyer, C. M. Reversible Switching of DNA-Gold Nanoparticle Aggregation. *Angew. Chem. Int. Ed.* **2004**, *43* (47), 6469-6471.
141. Ding, T.; Valev, V. K.; Salmon, A. R.; Forman, C. J.; Smoukov, S. K.; Scherman, O. A.; Frenkel, D.; Baumberg, J. J. Light-induced actuating nanotransducers. *Proc. Natl. Acad. Sci. U. S. A.* **2016**, *113* (20), 5503.
142. Ma, J.; Hu, Z.; Wang, W.; Wang, X.; Wu, Q.; Yuan, Z. pH-Sensitive Reversible Programmed Targeting Strategy by the Self-Assembly/Disassembly of Gold Nanoparticles. *ACS Appl. Mater. Interfaces* **2017**, *9* (20), 16767-16777.
143. Xia, H.; Li, F.; Hu, X.; Park, W.; Wang, S.; Jang, Y.; Du, Y.; Baik, S.; Cho, S.; Kang, T.; Kim, D.-H.; Ling, D.; Hui, K. M.; Hyeon, T. pH-Sensitive Pt Nanocluster Assembly Overcomes Cisplatin Resistance and Heterogeneous Stemness of Hepatocellular Carcinoma. *ACS Cent. Sci.* **2016**, *2* (11), 802-811.
144. Rao, A.; Roy, S.; Unnikrishnan, M.; Bhosale, S. S.; Devatha, G.; Pillai, P. P. Regulation of Interparticle Forces Reveals Controlled Aggregation in Charged Nanoparticles. *Chem. Mater.* **2016**, *28* (7), 2348-2355.
145. Chan, Y.-T.; Li, S.; Moorefield, C. N.; Wang, P.; Shreiner, C. D.; Newkome, G. R. Self-Assembly, Disassembly, and Reassembly of Gold Nanorods Mediated by Bis(terpyridine)-Metal Connectivity. *Chem. - Eur. J.* **2010**, *16* (14), 4164-4168.
146. Chen, S.; Guo, C. X.; Zhao, Q.; Lu, X. One-Pot Synthesis of CO₂-Responsive Magnetic Nanoparticles with Switchable Hydrophilicity. *Chem. - Eur. J.* **2014**, *20* (43), 14057-14062.

147. Zhang, J.; Han, D.; Zhang, H.; Chaker, M.; Zhao, Y.; Ma, D. In situ recyclable gold nanoparticles using CO₂-switchable polymers for catalytic reduction of 4-nitrophenol. *Chem. Commun.* **2012**, 48 (94), 11510-11512.
148. Flatté, M. E.; Kornyshev, A. A.; Urbakh, M. Understanding voltage-induced localization of nanoparticles at a liquid–liquid interface. *J. Phys.: Condens. Matter* **2008**, 20 (7), 073102.
149. Montelongo, Y.; Sikdar, D.; Ma, Y.; McIntosh, A. J. S.; Velleman, L.; Kucernak, Anthony R.; Ediel, J. B.; Kornyshev, A. A. Electrotunable nanoplasmonic liquid mirror. *Nat. Mater.* **2017**, 16 (11), 1127-1135.
150. Yu, Y.; Yu, D.; Orme, C. A. Reversible, Tunable, Electric-Field Driven Assembly of Silver Nanocrystal Superlattices. *Nano Lett.* **2017**, 17 (6), 3862-3869.
151. Yavuz, C. T.; Mayo, J. T.; Yu, W. W.; Prakash, A.; Falkner, J. C.; Yean, S.; Cong, L.; Shipley, H. J.; Kan, A.; Tomson, M.; Natelson, D.; Colvin, V. L. Low-Field Magnetic Separation of Monodisperse Fe₃O₄ Nanocrystals. *Science* **2006**, 314 (5801), 964.
152. Sim, S.; Miyajima, D.; Niwa, T.; Taguchi, H.; Aida, T. Tailoring Micrometer-Long High-Integrity 1D Array of Superparamagnetic Nanoparticles in a Nanotubular Protein Jacket and Its Lateral Magnetic Assembling Behavior. *J. Am. Chem. Soc.* **2015**, 137 (14), 4658-4661.
153. Riente, P.; Yadav, J.; Pericàs, M. A. A Click Strategy for the Immobilization of MacMillan Organocatalysts onto Polymers and Magnetic Nanoparticles. *Org. Lett.* **2012**, 14 (14), 3668-3671.
154. von Maltzahn, G.; Min, D. H.; Zhang, Y.; Park, J. H.; Harris, T. J.; Sailor, M.; Bhatia, S. N. Nanoparticle Self-Assembly Directed by Antagonistic Kinase and Phosphatase Activities. *Adv. Mater.* **2007**, 19 (21), 3579-3583.
155. Sidhaye, D. S.; Kashyap, S.; Sastry, M.; Hotha, S.; Prasad, B. L. V. Gold nanoparticle networks with photoresponsive interparticle spacings. *Langmuir* **2005**, 21 (17), 7979-7984.
156. Stricker, L.; Fritz, E.-C.; Peterlechner, M.; Doltsinis, N. L.; Ravoo, B. J. Arylazopyrazoles as Light-Responsive Molecular Switches in Cyclodextrin-Based Supramolecular Systems. *J. Am. Chem. Soc.* **2016**, 138 (13), 4547-4554.
157. Wang, D.; Kowalczyk, B.; Lagzi, I.; Grzybowski, B. A. Bistability and Hysteresis During Aggregation of Charged Nanoparticles. *J. Phys. Chem. Lett.* **2010**, 1 (9), 1459-1462.
158. Sahoo, B.; Devi, K. S. P.; Banerjee, R.; Maiti, T. K.; Pramanik, P.; Dhara, D. Thermal and pH Responsive Polymer-Tethered Multifunctional Magnetic Nanoparticles for Targeted Delivery of Anticancer Drug. *ACS Appl. Mater. Interfaces* **2013**, 5 (9), 3884-3893.

159. Zhou, K.; Wang, Y.; Huang, X.; Luby-Phelps, K.; Sumer, B. D.; Gao, J. Tunable, Ultrasensitive pH-Responsive Nanoparticles Targeting Specific Endocytic Organelles in Living Cells. *Angew. Chem. Int. Ed.* **2011**, *50* (27), 6109-6114.
160. Liu, Y.; Han, X.; He, L.; Yin, Y. Thermoresponsive Assembly of Charged Gold Nanoparticles and Their Reversible Tuning of Plasmon Coupling. *Angew. Chem. Int. Ed.* **2012**, *51* (26), 6373-6377.
161. Ferris, D. P.; Zhao, Y. L.; Khashab, N. M.; Khatib, H. A.; Stoddart, J. F.; Zink, J. I. Light-Operated Mechanized Nanoparticles. *J. Am. Chem. Soc.* **2009**, *131* (5), 1686-1688.
162. Housni, A.; Zhao, Y.; Zhao, Y. Using Polymers To Photoswitch the Aggregation State of Gold Nanoparticles in Aqueous Solution. *Langmuir* **2010**, *26* (14), 12366-12370.
163. Zhang, C.; Song, C.; Fry, H. C.; Rosi, N. L. Peptide Conjugates for Directing the Morphology and Assembly of 1D Nanoparticle Superstructures. *Chem. - Eur. J.* **2014**, *20* (4), 941-945.
164. Johny, M.; Vijayalakshmi, K.; Das, A.; Roy, P.; Mishra, A.; Dasgupta, J. Modulating the Phe-Phe dipeptide aggregation landscape via covalent attachment of an azobenzene photoswitch. *Chem. Commun.* **2017**, *53* (67), 9348-9351.
165. Zhao, Y. A.; Lei, B. Q.; Wang, M. F.; Wu, S. T.; Qi, W.; Su, R. X.; He, Z. M. A supramolecular approach to construct a hydrolase mimic with photo-switchable catalytic activity. *J. Mater. Chem. B* **2018**, *6* (16), 2444-2449.
166. Zou, R. F.; Wang, Q.; Wu, J. C.; Wu, J. X.; Schmuck, C.; Tian, H. Peptide self-assembly triggered by metal ions. *Chem. Soc. Rev.* **2015**, *44* (15), 5200-5219.
167. Zanna, N.; Milli, L.; Del Secco, B.; Tomasini, C. Factors Affecting the Stabilization of Polyproline II Helices in a Hydrophobic Environment. *Org. Lett.* **2016**, *18* (7), 1662-1665.
168. Heinz, H.; Farmer, B. L.; Pandey, R. B.; Slocik, J. M.; Patnaik, S. S.; Pachter, R.; Naik, R. R. Nature of Molecular Interactions of Peptides with Gold, Palladium, and Pd-Au Bimetal Surfaces in Aqueous Solution. *J. Am. Chem. Soc.* **2009**, *131* (28), 9704-9714.
169. Forood, B.; Perezpaya, E.; Houghten, R. A.; Blondelle, S. E. Formation of an extremely stable polyalanine beta-sheet macromolecule. *Biochem. Biophys. Res. Commun.* **1995**, *211* (1), 7-13.
170. Lomelí-Rosales, D. A.; Zamudio-Ojeda, A.; Cortes-Llamas, S. A.; Velázquez-Juárez, G. One-step synthesis of gold and silver non-spherical nanoparticles mediated by Eosin Methylene Blue agar. *Sci. Rep.* **2019**, *9* (1), 19327.
171. Anspón, H. D.; Bachmann, W. E.; Deno, N. C. p-Phenylazobenzoic acid. *Org. Synth.* **1945**, *25*, 86.

172. Bortolus, P.; Monti, S. cis .dblharw. trans Photoisomerization of azobenzene-cyclodextrin inclusion complexes. *J. Phys. Chem.* **1987**, *91* (19), 5046-5050.
173. Wang, D.; Zhao, W.; Wei, Q.; Zhao, C.; Zheng, Y. Photoswitchable Azobenzene/Cyclodextrin Host-Guest Complexes: From UV- to Visible/Near-IR-Light-Responsive Systems. *ChemPhotoChem* **2018**, *2* (5), 403-415.
174. Harada, A.; Takashima, Y.; Nakahata, M. Supramolecular Polymeric Materials via Cyclodextrin–Guest Interactions. *Acc. Chem. Res.* **2014**, *47* (7), 2128-2140.
175. Xie, F.; Ouyang, G.; Qin, L.; Liu, M. Supra-dendron Gelator Based on Azobenzene–Cyclodextrin Host–Guest Interactions: Photoswitched Optical and Chiroptical Reversibility. *Chem. - Eur. J.* **2016**, *22* (50), 18208-18214.
176. Bian, Q.; Wang, W.; Wang, S.; Wang, G. Light-Triggered Specific Cancer Cell Release from Cyclodextrin/Azobenzene and Aptamer-Modified Substrate. *ACS Appl. Mater. Interfaces* **2016**, *8* (40), 27360-27367.
177. Nehls, E. M.; Rosales, A. M.; Anseth, K. S. Enhanced user-control of small molecule drug release from a poly(ethylene glycol) hydrogel via azobenzene/cyclodextrin complex tethers. *J. Mater. Chem. B* **2016**, *4* (6), 1035-1039.
178. Zhang, J.; Zhou, Z.-H.; Li, L.; Luo, Y.-L.; Xu, F.; Chen, Y. Dual Stimuli-Responsive Supramolecular Self-Assemblies Based on the Host–Guest Interaction between β -Cyclodextrin and Azobenzene for Cellular Drug Release. *Mol. Pharm.* **2020**, *17* (4), 1100-1113.
179. Wu, X.; Xu, L.; Liu, L.; Ma, W.; Yin, H.; Kuang, H.; Wang, L.; Xu, C.; Kotov, N. A. Unexpected Chirality of Nanoparticle Dimers and Ultrasensitive Chiroplasmonic Bioanalysis. *J. Am. Chem. Soc.* **2013**, *135* (49), 18629-18636.
180. Shukla, N.; Bartel, M. A.; Gellman, A. J. Enantioselective Separation on Chiral Au Nanoparticles. *J. Am. Chem. Soc.* **2010**, *132* (25), 8575-8580.
181. Pendry, J. B. Negative Refraction Makes a Perfect Lens. *Phys. Rev. Lett.* **2000**, *85* (18), 3966-3969.
182. Pendry, J. B. A Chiral Route to Negative Refraction. *Science* **2004**, *306* (5700), 1353.
183. Smith, D. R.; Pendry, J. B.; Wiltshire, M. C. K. Metamaterials and Negative Refractive Index. *Science* **2004**, *305* (5685), 788.
184. Gansel, J. K.; Thiel, M.; Rill, M. S.; Decker, M.; Bade, K.; Saile, V.; von Freymann, G.; Linden, S.; Wegener, M. Gold Helix Photonic Metamaterial as Broadband Circular Polarizer. *Science* **2009**, *325* (5947), 1513.

185. Browne, J. P.; Strom, M.; Martin, S. R.; Bayley, P. M. The Role of β -Sheet Interactions in Domain Stability, Folding, and Target Recognition Reactions of Calmodulin. *Biochemistry* **1997**, *36* (31), 9550-9561.
186. Vassar, P. S.; Culling, C. F. Fluorescent stains, with special reference to amyloid and connective tissues. *Arch. Pathol.* **1959**, *68*, 487-498.
187. Biancalana, M.; Koide, S. Molecular mechanism of Thioflavin-T binding to amyloid fibrils. *Biochim. Biophys. Acta, Proteins Proteomics* **2010**, *1804* (7), 1405-1412.
188. Xue, C.; Lin, T. Y.; Chang, D.; Guo, Z. Thioflavin T as an amyloid dye: fibril quantification, optimal concentration and effect on aggregation. *R. Soc. Open. Sci.* **2017**, *4* (1), 160696.
189. Morihara, K.; Tsuzuki, H. Specificity of Proteinase K from *Tritirachium album* Limber for Synthetic Peptides. *Agric. Biol. Chem.* **1975**, *39* (7), 1489-1492.